



Norwegian University of
Science and Technology

Experimental Investigation and Mitigation of Vortex Shedding

Magne Tveit Bolstad

Master of Energy and Environmental Engineering

Submission date: December 2017

Supervisor: Pål Tore Selbo Storli, EPT

Co-supervisor: Kristian Sagmo, EPT
Ole Gunnar Dahlhaug, EPT

Norwegian University of Science and Technology
Department of Energy and Process Engineering

MASTER THESIS

for

student Magne Tveit Bolstad

Autumn 2017

Experimental investigation and mitigation of vortex shedding

Ekspérimentell undersøkelse og reduksjon av virvelavløsning

Background and objective

Vortexes will often form when a fluid is flowing over solid surfaces. In hydro power plants these vortexes can form when the water is flowing through the stay vanes and guide vanes, and these vortexes will flow into the runner and can cause high frequency noise and other unwanted effects. At the Waterpower laboratory modifications to original design have been proposed and numerically analysed to determine if the modifications work as intended. The results are promising, however there is the need to perform additional simulations and experimental measurements in order seek to validate the success of the geometry modifications.

The objective of the work will be to set up and perform Particle Image Velocimetry (PIV) measurements on original and modified geometry in a blade cascade rig, and to perform PIV measurements in the wicket gate and vaneless space of the Francis test rig at the Waterpower Laboratory at NTNU.

The following tasks are to be considered:

1. Literature study on vortex mechanisms, the mitigation of such vortexes and PIV measurement techniques
2. Perform and document PIV measurements of original and modified design in the blade cascade rig
3. Perform and document PIV measurements in the wicket gate and vaneless space of the Francis test rig

-- “ --

Within 14 days of receiving the written text on the master thesis, the candidate shall submit a research plan for his project to the department.

When the thesis is evaluated, emphasis is put on processing of the results, and that they are presented in tabular and/or graphic form in a clear manner, and that they are analysed carefully.

The thesis should be formulated as a research report with summary both in English and Norwegian, conclusion, literature references, table of contents etc. During the preparation of the text, the candidate should make an effort to produce a well-structured and easily readable report. In order to ease the evaluation of the thesis, it is important that the cross-references are correct. In the making of the report, strong emphasis should be placed on both a thorough discussion of the results and an orderly presentation.

The candidate is requested to initiate and keep close contact with his/her academic supervisor(s) throughout the working period. The candidate must follow the rules and regulations of NTNU as well as passive directions given by the Department of Energy and Process Engineering.

Risk assessment of the candidate's work shall be carried out according to the department's procedures. The risk assessment must be documented and included as part of the final report. Events related to the candidate's work adversely affecting the health, safety or security, must be documented and included as part of the final report. If the documentation on risk assessment represents a large number of pages, the full version is to be submitted electronically to the supervisor and an excerpt is included in the report.

Pursuant to "Regulations concerning the supplementary provisions to the technology study program/Master of Science" at NTNU §20, the Department reserves the permission to utilize all the results and data for teaching and research purposes as well as in future publications.

The final report is to be submitted digitally in DAIM. An executive summary of the thesis including title, student's name, supervisor's name, year, department name, and NTNU's logo and name, shall be submitted to the department as a separate pdf file. Based on an agreement with the supervisor, the final report and other material and documents may be given to the supervisor in digital format.

- Work to be done in lab (Water power lab, Fluids engineering lab, Thermal engineering lab)
 Field work

Department for Energy and Process Engineering, *July 31st, 2017.*



Pål-Tore Storli
Supervisor

Co-Supervisor(s): Kristian Sagmo, Ole Gunnar Dahlhaug

Preface

This work has been conducted at the Waterpower Laboratory at the Department of Energy and Process Engineering as part of concluding my Master's degree in Energy and Environmental engineering at the Norwegian University of Science and Technology (NTNU). The work has been part of the research project HiFrancis at the Waterpower Laboratory, which addresses the challenges related to pressure pulsations occurring in high-head Francis turbines.

During this work I have been given the opportunity to combine my interest and joy for both theoretical and practical engineering. The opportunity to work with such high-end equipment and experimental systems as in the laboratory has certainly increased my interest and knowledge within experimental engineering.

I have been privileged to work amongst the researchers and professors in the Waterpower Laboratory. I would like to thank my supervisor Pål-Tore Storli for giving me the opportunity of working on a highly interesting and challenging subject, and for his guidance when needed. I would also like to thank PostDoc Bjørn Winther Solemslie and Chirag Trivedi, PhD candidates Carl Werdelin Bergan and Eirik Volent, and Dr. Alex Nila in LaVision for advice, discussions and fantastic technical assistance when needed. Special thanks also goes to my co-supervisor and collaborator in the laboratory, PhD candidate Kristian Sagmo, for great discussions and work on the experimental measurements.

Finally, I would like to give a thanks to all those who have contributed to the warm, open-doored environment in the Waterpower Laboratory. The memories and friendships acquired here will be cherished in many years to come.



Magne Tveit Bolstad
Trondheim, December 17, 2017

Abstract

As part of meeting the increase in energy needs and environmental challenges, energy production using intermittent power sources as wind, solar and wave energy has increased. As a consequence, hydropower plants are exploited for their stabilizing abilities, and are subjected to an increasing number of transient operations e.g. load variations and start-stop operations. This may require turbines to be operated at conditions outside their best efficiency operating points. One of the most common hydropower turbines – the Francis turbine – is highly sensitive to variations in flow conditions. Efficiency decrease, high frequency noise and pressure pulsations due to rotor stator interaction (RSI) and fluid structure-interaction (FSI) may occur, potentially causing fatal structural failures when operating outside design conditions.

Pressure measurements and simulations of flow around hydrofoils and through a Francis turbine model have been performed at the Waterpower Laboratory at NTNU to gain understanding of these undesired phenomena and structural failures. Experimental determination of the velocity field and its coupling to FSI and RSI is yet to be performed. In addition, a new hydrofoil design has been suggested in order to mitigate the undesired effects caused by vortex shedding from turbine components e.g. stay vanes, guide vanes and runner blades. The numerical results are promising, but require experimental data to be validated.

The main objective of this thesis has been to acquire experimental measurements of the velocity field in the trailing edge region of hydrofoils and in the vaneless space of a Francis turbine, and investigate its relation to FSI. Two experimental setups have been planned and designed. Measurements using particle image velocimetry (PIV) were performed on one of the two setups, and the velocity field downstream a hydrofoil was determined. Simultaneous measurements of foil vibration were performed to evaluate the degree of FSI, and the acquired data was compared to both previous simulations and relevant experiments.

A dynamic particle seeding system was developed, allowing for PIV measurements of vortex shedding on a large scale piping system. A blade cascade test section was utilized for PIV measurements in the downstream region of a hydrofoil with trailing edge resembling that of a typical Francis runner blade. Measurements of foil vibration allowed for a thorough mapping of the vortex shedding- and foil vibrational frequency both in and around lock-in mode. Lock-in was found to occur in the velocity range 11.1 m/s - 12.1 m/s , at frequencies increasing from approximately 640 Hz to 648 Hz . A significant increase in vortex shedding frequency-stability was found during lock-in. Outside lock-in, the vortex shedding frequency followed the Strouhal law for hydrofoils, where a Strouhal number of 0.22 was found adequate. The measured vortex shedding frequency in lock-in was found to be approximately 21 % higher than the one found through simulations. Due to time-constraints, the suggested design modifications were not implemented, and whether the modifications work as intended or not was not determined.

Due to technical problems and time constraints, no measurements were performed on the Francis-turbine. However, a discussion of the requirements for the experimental setup, together with a description of and recommendations for the setup, has been provided.

Keywords: Hydropower, Francis turbines, Flow-Induced Vibration, FSI, Lock-In, PIV.

Sammendrag

For å møte de tiltagende utfordringene relatert til energibehov og klima, har energiproduksjon med bruk av periodiske energikilder som vind, sol og bølger, økt. Som en konsekvens av dette blir vannkraftverk i økende grad brukt under varierende driftsforhold som for eksempel lastvariasjoner og start-stop operasjoner, på grunn av sine stabiliserende egenskaper på strømmettet. Dette kan kreve at turbiner i større grad må opereres utenfor best-punkt. En av de mest vanlige vannkraftturbinene – Francisturbinen – er svært sensitiv for endringer i lastforhold. Redusert virkningsgrad, høyfrekvent lyd og trykkpulsasjoner grunnet rotor-stator interaksjon (RSI) og fluid-struktur interaksjon (FSI) kan oppstå under drift utenfor best-punkt, og muligens gi fatale konstruksjonsmessige svikt.

Trykkmålinger og simuleringer av strømmingen rundt en hydrofoil og gjennom en Francisturbin-modell har tidligere blitt utført ved vannkraftlaboratoriet ved NTNU, for å oppnå økt forståelse av disse uønskede fenomenene og strukturelle svikt. Eksperimentell bestemmelse av hastighetsfelt og dets kobling til FSI og RSI gjenstår å gjennomføres. I tillegg har det blitt utviklet et nytt design av en hydrofoil med formål å dempe de uønskede effektene relatert til virvelavløsning fra turbinkomponenter som stagskovler, ledeskovler og løpehjulskovler. De numeriske resultatene er lovende, men eksperimentell validering gjenstår.

Hovedformålet med denne oppgaven er å skaffe eksperimentelle målinger av hastighetsfeltet i området like nedstrøms avløpskanten til en hydrofoil, samt i det skovelløse området til en Francisturbin, for å deretter studere koblingen mellom hastighetsfeltet og FSI. To eksperimentelle oppsett har blitt planlagt og designet. Målinger ved bruk av particle image velocimetry (PIV) ble utført på et av de to oppsettene, og hastighetsfeltet nedstrøms en hydrofoil ble bestemt. Samtidsmålinger av foilvibrasjon ble gjennomført for vurdering av graden av FSI, og de innsamlede data ble sammenlignet med både tidligere simuleringer og relevante eksperiment.

Et dynamisk matingsystem som tillot PIV-målinger av virvelavløsninger i et storskala rørsystem, ble utviklet. En bladkaskade testseksjon ble brukt for PIV-målinger i området nedstrøms en hydrofoil med en tilnærmet lik avløpskant som en typisk Francis løpehjulskovel. Målinger av foilvibrasjon tillot en grundig kartlegging av virvelavløsnings- og vibrasjonsfrekvens både i og utenfor lock-in. Lock-in ble observert til å oppstå i hastighetsområdet $11.1 \text{ m/s} - 12.1 \text{ m/s}$, med frekvenser økende fra 640 Hz to 648 Hz . En signifikant økning i frekvensstabiliteten til virvelavløsningen i lock-in ble observert. Utenfor lock-in samsvarte virvelavløsningsfrekvensen godt med den empirisk estimerte frekvensen for hydrofoiler ved bruk av Strouhal tall lik 0.22. Den målte virvelavløsningsfrekvensen i lock-in ble målt til å være tilnærmet 21 % høyere enn frekvensen funnet gjennom simulering. Grunnet tidsbegrensninger ble ikke de foreslåtte designmodifikasjonene implementert. De følgende virkningene av modifikasjonene kunne dermed ikke bestemmes.

Grunnet tekniske problemer og tidsbegrensninger ble det ikke gjennomført målinger på Francisturbinen. En diskusjon av kravene til det eksperimentelle oppsettet ble allikevel gjennomført og presentert sammen med en beskrivelse av, og anbefalinger til, det eksperimentelle oppsettet.

Nøkkelord: Vannkraft, Francisturbiner, Strømnings-Indusert Vibrasjon, FSI, Lock-in, PIV

Contents

CHAPTER 1 INTRODUCTION	1
1.1 BACKGROUND OF STUDY	1
1.2 MOTIVATION AND INSPIRATION	2
1.3 OBJECTIVE	3
1.4 STRUCTURE OF THESIS	4
CHAPTER 2 THEORY AND TECHNICAL BACKGROUND	5
2.1 WAKE FLOW	5
2.2 VORTEX FLOW	6
2.3 VORTEX SHEDDING	7
2.3.1 <i>Basic Flow Mechanism</i>	8
2.3.2 <i>Strouhal Number</i>	11
2.4 FLOW INDUCED VIBRATION	12
2.4.1 <i>Lock-In Phenomenon</i>	13
2.5 HYDROFOILS AND VANES	15
2.5.1 <i>Flow over Hydrofoils</i>	15
2.5.2 <i>Trailing Edge Profiles and Mitigation of Vortex Shedding</i>	16
2.5.3 <i>Guide Vanes</i>	20
2.6 ROTOR–STATOR INTERACTION	20
2.7 SPECTRAL ANALYSIS	22
2.8 UNCERTAINTY ANALYSIS	23
CHAPTER 3 PARTICLE IMAGE VELOCIMETRY	25
3.1 WORKING PRINCIPLE	25
3.2 IMAGE SETTINGS	27
3.3 IMAGE ACQUISITION	29
3.4 PRE-PROCESSING	31
3.5 POST-PROCESSING	31
CHAPTER 4 INVESTIGATIONS OF FSI AT THE WATERPOWER LABORATORY	33
4.1 HYDROFOIL INVESTIGATIONS	33
4.1.1 <i>Experimental Investigations of FSI</i>	33
4.1.2 <i>Simulations of Vortex Shedding from Trailing Edges</i>	34
4.1.3 <i>Summary and Discussion of Results</i>	37
4.2 FRANCIS TURBINE	38
4.2.1 <i>Flow Simulation in the Vaneless Space</i>	38
CHAPTER 5 EXPERIMENTAL PROCEDURE AND SETUP	41
5.1 HYDRAULIC SYSTEM	41
5.2 PIV ANALYSIS AND EQUIPMENT	42
5.3 BLADE CASCADE	44
5.3.1 <i>Test Unit Description</i>	44
5.3.2 <i>Original Hydrofoil</i>	46
5.3.3 <i>Modified Hydrofoil</i>	47

5.3.4	<i>Experimental Setup</i>	48
5.3.5	<i>Flow and Strain Analysis</i>	49
5.3.6	<i>PIV Measurements and Analysis</i>	49
5.4	FRANCIS TURBINE.....	53
5.4.1	<i>Unit Description</i>	53
5.4.2	<i>Experimental Setup</i>	55
5.4.3	<i>PIV Measurements</i>	56
5.5	UNCERTAINTY OF TESTS.....	58
5.5.1	<i>Uncertainty in Test Section Velocity</i>	58
5.5.2	<i>Uncertainty in Frequency and Repeatability</i>	59
5.5.3	<i>Uncertainty in PIV Measurements</i>	59
CHAPTER 6 RESULTS AND DISCUSSION		61
6.1	BLADE CASCADE	61
6.1.1	<i>Strain Measurements</i>	61
6.1.2	<i>Velocity Field Measurements</i>	65
6.1.3	<i>Swirling Strength Analysis</i>	67
6.1.4	<i>Vortex Shedding Frequency Analysis</i>	69
6.1.5	<i>General Discussion</i>	74
6.2	FRANCIS TURBINE.....	75
CHAPTER 7 CONCLUSION		77
CHAPTER 8 FURTHER WORK.....		79
APPENDICES.....		
	APPENDIX A: Matlab Scripts	i
A.1:	Strain Analysis	iii
A.2:	PIV analysis	vii
	APPENDIX B: Measurement Results	xi
B.1:	Strain Measurements	xiii
B.2:	PIV measurements	xiv
	APPENDIX C: Risk Assessment Report.....	xvi

List of Figures

Figure 1.1 – Section view of a Francis-turbine.....	1
Figure 1.2 – Owl wing and its distinctive properties.....	3
Figure 2.1 – Wake flow	6
Figure 2.2 – Free vortex general velocity behavior.....	7
Figure 2.3 –Vortex formation.....	9
Figure 2.4 – Vortex creation and von Karman vortex street from a cylinder.....	9
Figure 2.5 – Strouhal number dependency of Reynolds number for circular cylinders.....	12
Figure 2.6 – Lift generation from vortex shedding.....	13
Figure 2.7 – Lock-in phenomenon.....	14
Figure 2.8 – Typical relative pressure distribution along a hydrofoil.....	15
Figure 2.9 – Vortex characteristics.....	17
Figure 2.10 – The experimentally and numerically investigated airfoil trailing edges	19
Figure 2.11 – Rotor-stator interaction between runner and wicket gate.....	21
Figure 2.12 –Pressure distribution in stay vanes and guide vanes prior to runner inlet	21
Figure 2.13 – Fourier transform of time-varying signal	22
Figure 3.1 – PIV working principle figure.....	26
Figure 3.2 – General procedure of PIV measurements.....	27
Figure 3.3 – Vortex description with a too large IW size (a) and suitable IW size (b).	28
Figure 2.4 – Light refraction due to surface curvature	29
Figure 3.5 – Interrogation Window for vector-analysis	30
Figure 3.6 – Cross correlation of a double framed image using cross correlation.	31
Figure 4.1 – Measured foil vibrational frequency vs test section velocity.....	34
Figure 4.2 - Original hydrofoil design used in simulations	35
Figure 4.3 - Modified hydrofoil design.....	35
Figure 4.4 – Mesh utilized in the simulations by Heggebø.	36
Figure 4.5 – Shedding frequencies of OHF (a) and MHF with six serrations (b).....	36
Figure 4.7 – Hexahedral mesh utilized in Trivedi’s simulations.	39
Figure 4.8 – Velocity plot for the Francis-model at BEP.....	39
Figure 5.1 – Closed-loop hydraulic system in the waterpower laboratory.....	42
Figure 5.3 – PIV procedure for the experimental setups.....	44
Figure 5.4 – Exploded view of main parts of the test section.....	45
<i>Figure 5.5</i> – Flow wise cross section of test section of blade cascade.....	46
Figure 5.6 – Blade cascade test section.	46
Figure 5.7 – Original hydrofoil design with dimensions.	47
Figure 5.8 – Modified hydrofoil trailing edge geometry.	47
Figure 5.9 – Experimental setup for blade cascade.	48

Figure 5.10 – Blade cascade PIV setup.	50
Figure 5.11 – Calibration setup.....	51
Figure 5.12 – Raw image before and after pre-processing.	52
Figure 5.13 – Model turbine showing the laser slit and plexiglas guide vanes.	54
Figure 5.14 – Guide vane geometry in the model turbine.	54
Figure 5.15 – Experimental setup for PIV-measurements on Francis turbine.....	55
Figure 5.16 – Section-view of the PIV setup for the Francis turbine	56
Figure 5.17 – Uncertainty distribution of the instantaneous velocity field at 11.1m/s.....	60
Figure 6.1 – Foil vibrational frequency for velocity range.....	63
Figure 6.2 - Normalised foil vibrational frequency for velocity range.....	64
Figure 6.3 – Instantaneous velocity field for the first measurement at 11.1 <i>m/s</i>	66
Figure 6.4 – Average velocity field for first measurement at 11.1 <i>m/s</i>	67
Figure 6.5 – Instantaneous swirling strength field of the velocity field in figure 6.3.....	68
Figure 6.6 – Instantaneous vortex-velocity field representation of the velocity field in figure 6.3.....	69
Figure 6.7 – Power spectrum for the four measurements at 11.1 <i>m/s</i>	70
Figure 6.8 – Power spectrum of vortex shedding frequency for velocity range.....	72
Figure 6.9 – Normalized power spectrum of vortex shedding frequency for velocity range ..	73
Figure 6.10 – Measured vortex shedding frequency, foil vibrational frequency and empirically estimated vortex shedding frequency.....	74

Abbreviations

AOI	Area of Interest
BEP	Best Efficiency Point
CMOS	Complementary Metal-Oxide Semiconductor
DFT	Discrete Fourier Transform
DTFT	Discrete Time Fourier Transform
FFT	Fast Fourier Transform
FOV	Field of View
FSI	Fluid-Structure Interactions
GV	Guide Vane
OHF	Original Hydrofoil
MHF	Modified Hydrofoil
IW	Interrogation Window
LDV	Laser Doppler Vibrometry
LE	Leading Edge
LTS	Laser Timing Stabilizer
NdYAG	Neodymium-doped Yttrium Aluminium Garnet
NTNU	Norges Tekniske Naturvitenskapelige Universitet
PIV	Particle Image Velocimetry
PTU	Programmable Timing Unit
RSI	Rotor-Stator Interaction
LabVIEW	Laboratory Virtual Instrument Engineering Workbench
SV	Stay Vane
TE	Trailing Edge
TKE	Turbulent Kinetic Energy
TTO	Technology Transfer Company

Nomenclature

Symbol	Description	Unit
a_x	Longitudal vortex spacing	[m]
b	Test unit side-wall width	[m]
B	Geometry factor of trailing edge	[-]
B_x	Systematic uncertainty in value of x	[%]
B_X	Total systematic uncertainty in measurement of x	[%]
C	Constant	[-]
D	Characteristic diameter	[m]
ds	Particle pixel movement	[$pixel$]
dt	Laser pulse separation time	[s]
e_l	Error in length	[m]
f	Frequency of dynamic phenomena	[Hz]
f_n	Natural frequency of structure	[Hz]
f_s	Vortex shedding frequency	[Hz]
f_{sample}	Sample rate	[Hz]
N	Number of samples in measurement	[-]
n	Number of errors in system	[-]
n_v	Number of passing vortices	[-]
n_{IW}	Length and width of image window	[$pixels$]
U_v	Velocity of vortex in flow direction	[m/s]
k	Slope of frequency versus velocity curve	[$1/m$]
L	Characteristic length	[m]
L_f	Vortex formation length	[m]
l	Distance from trailing edge to vortex center	[m]
Q	Volumetric flow through Francis-turbine	[m^3/s]
r	Radius from vortex center	[m]

Re	Reynolds number	[-]
St	Strouhal number	[-]
t	Hydrofoil trailing edge thickness	[m]
$\frac{t\alpha}{2}$	Student-t value for confidence level $1 - \alpha$	[-]
T	Duration of sampling period	[s]
U	Free stream velocity	[m/s]
U_l	Velocity outside wake at location l	[m/s]
u	Velocity along velocity profile	[m/s]
u_θ	Vortex tangential velocity	[m/s]
x	Value of measurand	[-]
w_x	Total uncertainty in measurement of x	[%]

Greek symbols

Symbol	Description	Unit
ρ	Fluid density	[kg/m ³]
Δf	Frequency increment in power spectrum	[Hz]
Γ	Strength of vortex	[-]
Γ_l	Strength of travelling vortex	[-]
δ'	Virtual boundary layer displacement thickness	[m]
μ	Dynamic viscosity	[Ns/m ²]

Chapter 1

Introduction

This chapter presents the background of the work presented. A description of the inspiration and motivation of the work is given, together with a definition of the objective of the work. This is followed by a presentation of the structure of the thesis.

1.1 Background of Study

Electric energy generated from hydropower is one of the most clean and cost efficient sources of energy existing today. It remains the most established, widely used and long-lasting renewable resource for production of clean electricity [1]. Hydropower turbines may be considered as the heart of a hydropower plant, and with today's state of the art designs, turbines are found with efficiencies reaching up to 96% [1]. In addition to being highly effective, hydropower turbines also serve a key role in power-grid stabilization due to their short response time and immediate availability [2]. As part of meeting the increase in energy needs and environmental challenges, energy production using intermittent power sources e.g. wind, solar and wave energy has increased. As a consequence, hydropower plants are victims of their availability and stabilizing properties, and may be required to operate at off-design conditions, i.e. conditions different from the turbine's best efficiency point (BEP). One of the most common hydropower turbine types is the Francis turbine, presented in figure 1.1. These turbines reach high efficiencies, but are highly sensitive to changes in flow rate, and rapid drops in efficiencies may occur if the flow rate diminishes [1].

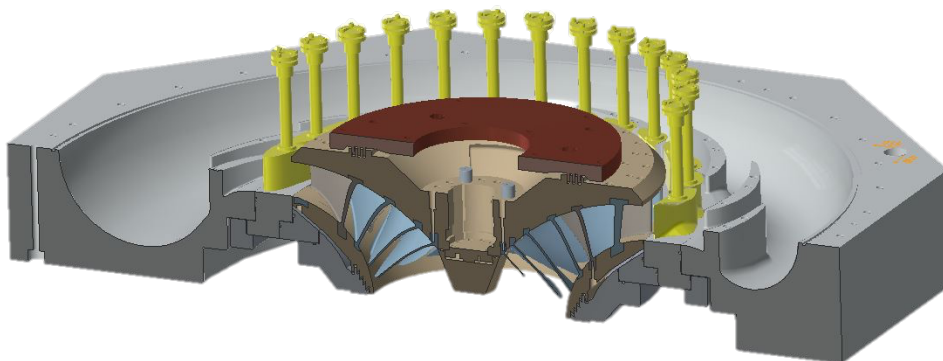


Figure 1.1 – Section view of a Francis-turbine showing spiral casing (grey), stay vanes (grey), guide vanes (yellow) and runner (brown and blue). Adapted from [3]

Operating at these variable off-design conditions, and under an increasing amount of transient operations e.g. start-stop operations, implies operation under less favorable conditions where undesired effects as pressure pulsations and high frequency noise are likely to occur [4].

As a consequence of improvements in welding techniques, usage of lightweight, high tensile strength runner materials and increased turbine efficiencies, the weight-to-power of Francis turbines has decreased [4]. The combination of using such lightweight turbines and increasingly operating at less favorable conditions has given rise to several challenges related to high frequency pressure pulsations, rotor-stator interaction (RSI), fluid-structure interaction (FSI), and fatigue damages [4]. These high frequency phenomena have introduced structural problems in turbine runners and adjacent components, with consequences e.g. turbine runner blade cracking within a short period of operation, even for brand new turbine runners produced today [4], [5]. The impact and degree of occurrence of these phenomena are often directly related to the design and shape of the turbine components, which emphasizes the necessity and importance of design optimization.

In several cases, the high frequency cycle fatigue damage and noise are provoked by the occurrence of the phenomenon vortex shedding. During the 1970s a wave of problems related to vortex shedding and noise from the trailing edges (TE) of stay vanes (SV) occurred as a consequence of non-ideal SV profiles and TE designs [6]. These events occurred despite extensive research on TE designs during the 1950s, to be discussed in a later section. In the meantime, turbine designers and manufacturers have become more cautious, and the occurrence of these problems have been decreased [6]. Further, the ability of a more precise prediction of the occurring forces has increased as a results of the development of more advanced numerical tools, computer power and computational fluid dynamics (CFD). However, due to the complexity of the flow dynamics, it is apparent that a credible estimation of the forces occurring in a turbine subject to variable load conditions is challenging and difficult to achieve, and problems still occur [7].

1.2 Motivation and Inspiration

From the mentioned problems, it is evident that a credible estimation of the undesired forces from FSI and RSI occurring in the turbine could serve as a valuable tool in the design-phase of the turbine. If the forces and dynamic phenomenon could be predicted, the turbine components could be dimensioned to withstand these forces without being over-dimensioned, possibly reducing production and maintenance cost. Another approach is to study the origin of the problematic phenomena, and investigate the possibilities of reducing their impact or prevent them from occurring. It is observed that many of the high-frequency pressure pulsations occurring in today's turbines are related to the RSI between runner and guide vanes (GV) in high head Francis turbines [4]. In fact, such pressure pulsations have been found to cause turbine blade cracking after only a week of operation [4]. Not only do such problems represent a potential expense in maintenance cost, but it also implies a significant loss in income due to lack of electricity production. It is therefore of high economic interest to prevent any possible failures or damages to occur.

In order to enhance performance and dampen undesired effects e.g. high frequency noise, designs inspired by nature has previously been implemented in constructions e.g. windmills and wings [8]. In both hydrodynamics and aerodynamics, the TEs of hydrofoils and wings are generally straight in the spanwise direction. In nature, however, three-dimensional serrated geometries are found on the wings and fins of birds and aquatic animals, suggesting this to be a favorable geometry [8].

Many species of owls are known as silent predators, capable of approaching their prey in almost absolute silence [8], [9]. The presence of both leading edge (LE) and TE serrations on its wings, as shown in figure 1.2, have been found to affect the vortex shedding characteristics in the wake and suppress noise [8].

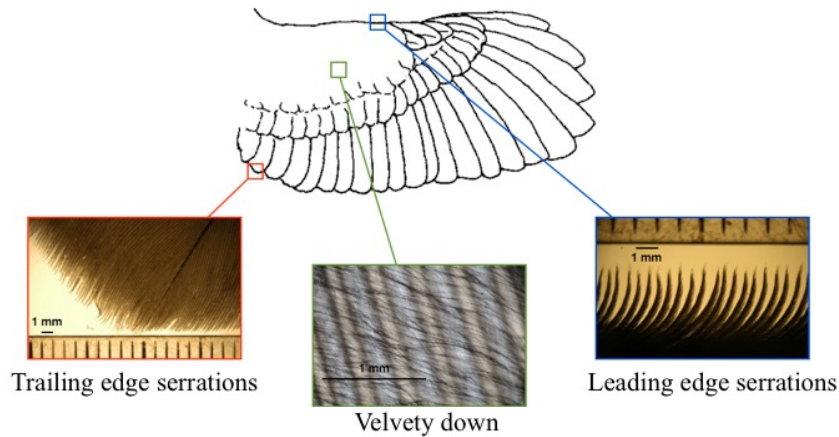


Figure 1.2 – Owl wing and its distinctive properties. Adapted and modified from [10].

The silent flight of the owl has been a subject of engineering interest for many decades, but the precise function of the wing attributes is not yet fully understood [11]. Many of the owl's wing-attributes have already been implemented in the design of airfoils, and it is believed that the wing-attributes may also be implemented in hydropower turbine components to mitigate the effects of vortex shedding and degree of pressure-pulsations.

A new hydrofoil with a TE inspired by the serrations found on owl wings have been developed at the Waterpower Laboratory at the Norwegian University of Science and Technology (NTNU). Simulations have been performed to evaluate the TE's geometry's capacity to mitigate the effects of vortex shedding and pressure pulsations, and the results are promising. However, the results are yet to be verified through experimental measurements and analysis. To the author and to the Technology Transfer company (TTO) at NTNU there are no known studies on spanwise modifications of TEs of turbine vanes. This makes it both highly interesting and exciting to study.

1.3 Objective

The ultimate objective of the work in the Waterpower Laboratory is to achieve increased understanding and ultimately a mitigation of FSI and pressure pulsations occurring due to RSI in Francis-turbines. Pressure measurements and simulations of flow around hydrofoils and in the vaneless space of a Francis turbine have been carried out, and more are to be made as part of achieving this objective. To gain increased understanding and to verify simulated results, experimental data of the corresponding velocity distributions is required. In this thesis, the main objective is to plan, set up, perform and document particle image velocimetry (PIV) measurements of the flow downstream of two hydrofoil geometries and in the vaneless space of a modified Francis turbine model, as an approach towards this ultimate objective.

PIV measurements are to be performed in the downstream region of a hydrofoil with geometry resembling that of a typical Francis runner blade, hereby referred to as the original hydrofoil (OHF). The measurements are to be used to map the vortex shedding frequency and investigate its relation to FSI in the hydrofoil. The suggested modification of adding a three-dimensional serrated edge to the TE of the OHF is then to be implemented, and similar PIV measurements are to be performed on this modified hydrofoil (MHF). The acquired data from the measurements are to be used to determine if the effects of vortex shedding and degree of FSI may be mitigated by means of this TE design, while also serving as comparative data for the already performed simulations. Further, PIV measurements are to be performed in the vaneless space of the modified Francis turbine to determine the velocity distribution in this area and its relation to FSI and RSI in the turbine.

A literature study on the mechanisms of vortex shedding and its relation to Francis turbine's blade geometry and FSI will serve as a foundation for evaluating vortex shedding frequencies, amplitudes and FSI in the measurements. A literature study on the PIV measurement technique and PIV setup-requirements will also be conducted in order to obtain an experimental setup which gives reliable measurements.

1.4 Structure of Thesis

Chapter 2 presents the theory and technical background on the subject. This includes a summary of previous work on TEs of both air- and hydrofoils, with the main focus being on the latter. A brief presentation of frequency analysis and uncertainties related to experimental work is also given here.

Chapter 3 presents the fundamentals of the experimental method of PIV together with a description of the requirements for obtaining reliable results using this technique.

Chapter 4 presents the previous simulations and experimental measurements on the hydrofoil and Francis turbine in the Waterpower Laboratory, and serves as the numerical and experimental comparative basis for the PIV- and FSI measurements.

The experimental equipment, setups, procedure and method of analysis is presented in Chapter 5, while Chapter 6 presents the achieved results. Chapter 6 also includes a discussion of the corresponding results. Chapter 7 presents a summary of the performed work, including conclusive remarks. Recommendations of further work and improvements are presented in Chapter 8.

In the appendices, appendix A presents the MATLAB scripts used in the analysis process. Appendix B presents additional results from both foil strain- and PIV measurements. Appendix C presents the report of the risk assessment carried out prior to performing the experimental measurements.

Chapter 2

Theory and Technical Background

This chapter presents a brief overview of the fundamental fluid mechanical phenomena considered to be of most importance regarding flow in Francis turbines and around hydrofoils, and the objective of this thesis. An analysis of the main problems related to FSI and RSI regarding TEs of hydro turbine blades and vanes will be given, together with a presentation of the previous and current work performed to mitigate these problems. Finally, the fundamentals of power spectrum- and uncertainty analysis for experimental work will be presented, to be used as a tool for evaluation of frequencies and uncertainties, respectively, in the measurements to be performed.

Remark: This chapter builds on the literature review carried out by the author as part of specialisation project TEP4540, and as such, parts of section 2.4 - 2.6 have been reproduced/reused therefrom [3].

2.1 Wake Flow

Any body immersed in a real, viscous fluid flow will have a region of disturbed flow in the downstream region of the body manifested at sufficiently high Reynolds numbers [12], [13]. The upper and lower boundary layers (BL) coalesce at the TE of the object, generating a *wake profile* whose width increases with increasing distance from the TE, while the velocity defect decreases as indicated in figure 2.1, [14]. L_f in the figure indicates the downstream position of the maximum velocity deficit across the wake.

Wake flow is generally divided into three regions [12]–[15]. Close to the TE there will be a *near-wake* or *dead-zone* region, followed by a *mixing region* before the *far-wake* or *pure-wake* region is developed, as presented in figure 2.1. In the near-wake, the flow is characterised by circulation of fluid from the upper and lower shear layer. As the closure of the near-wake at distance L_f from the TE approaches, the upper and lower shear layers interact in the mixing-region. This may cause instabilities, represented by the blue lines in the figure, which will be discussed in section 2.3. In this mixing region there is a high degree of momentum exchange between the free stream and the wake, causing the velocity gradients across the wake to decrease [13]. This in turn causes the wake width to increase and the wake profile to develop, until it reaches the far-wake region where the velocity profile will have a self-preserving shape, i.e. a velocity profile independent of the downstream position when scaled by its local length and velocity scale [8][9].

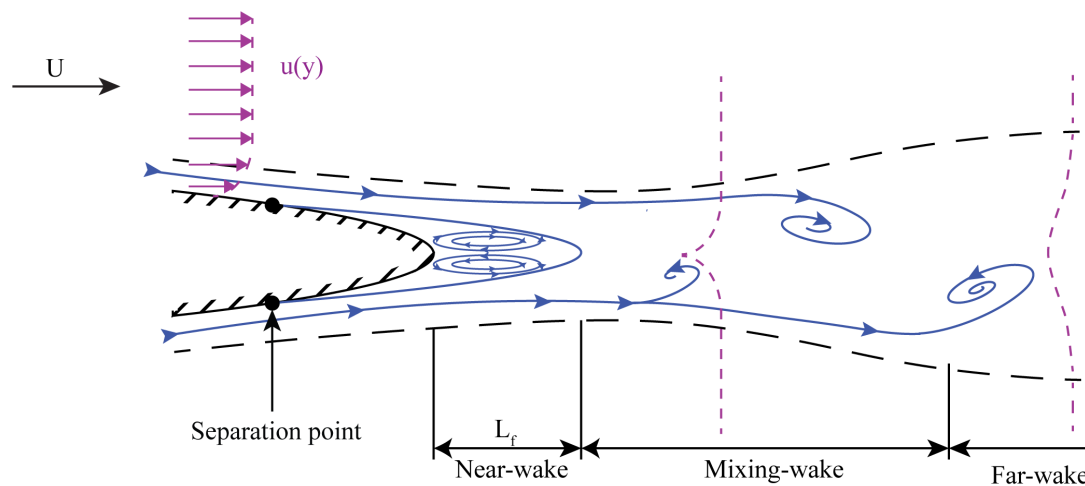


Figure 2.1 – Wake flow with the wake regions, location of maximum velocity deficit, separation point and the velocity profile throughout the flow region indicated.

For laminar flow over slender bodies the wake is smooth and narrow, with wake characteristics that may be determined using BL theory [14], [15]. Flows over bluff bodies on the other hand, will generate a broad and pulsating wake, and the wake profile would need to be determined as a time-averaged wake [15], [16]. In general, the wake of a turbulent flow is more narrow compared to a laminar flow over the same object, and self-similarity may not develop until up to 1000 diameters downstream [16], [17]. The wake flow of such flows, or flow over bluff bodies, is inherently three-dimensional and disorganized, and determining the wake characteristics is a more complicated procedure which requires experimental data to be determined [14], [15], [16]. For a thorough evaluation of turbulent wake flows the reader is referred to [14].

2.2 Vortex Flow

A flow where all streamlines consist of concentric circles about a given point, where the tangential velocity, u_θ , along any streamline is inversely related to the distance, r , from the center point, may be characterized as a free vortex flow [18]. Mathematically it can be described as

$$u_\theta = \frac{C}{r} \quad (2.1)$$

where C is a constant depending on the circulation, Γ , or strength, of the vortex [18]. The strength of a free vortex may be calculated using (2.2), [18].

$$\Gamma = 2\pi r u_\theta \quad (2.2)$$

From (2.1), it is evident that there is a discontinuity at the vortex centre, and the flow velocity is reversed, as shown in figure 2.2. Locating this point of discontinuity makes it possible to define a radial distance, and by measuring the tangential velocity at some radial distance the strength of the vortex may be determined using (2.2).

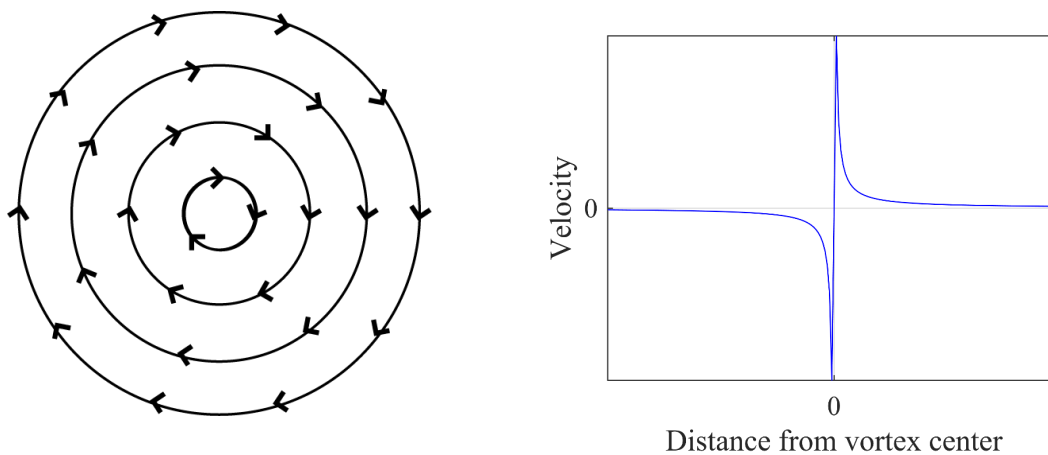


Figure 2.2 – Free vortex general velocity behavior.

Despite being of fundamental importance in fluid mechanics, there is still no consensus on a general rigorous definition of this distinct phenomenon [19]–[22]. The problem is exacerbated by the lack of boundaries, i.e. when looking at the vortex structure in figure 2.2 it is difficult to agree on where the vortex ends [20], [21].

Additional problems are also related to locating vortices in a flow. The above-mentioned procedure is based on identifying a local extremum in the rotational velocity. However, this is actually not a necessary condition of the existence of a vortex [19]. During the last decades, a large number of visualization techniques have been suggested to identify and interpret vortex structures and vortex magnitudes [19], [20], [22]. For the scope of this text, any fluid motion that suggests rotation of fluid particles about a fixed or moving center, i.e. a swirling motion, will be referred to as a vortex. The identification and degree of rotational motion of these vortices will be based on the swirling-strength of the flow, which has been proven to identify vortices successfully in similar studies [19]–[22]. The definition of swirling strength is related to the complex eigenvalues of the velocity gradient tensor, which will not be discussed in detail in this text. For a brief overview of the mathematical details of this quantity the reader is referred to literature [19].

2.3 Vortex Shedding

Vortex shedding is a dominant feature occurring for almost any bluff geometry exposed for fluid flow, irrespective of whether the flow is laminar or turbulent [23]. Depending on the structural design, the presence of vortex shedding may cause crucial structural failures in constructions e.g. bridges, chimneys, hydrofoils and airfoils. In a waterpower context, the effects of vortex shedding is related to the mentioned creation of high frequency noise, alternating stresses and corresponding mechanical fatigue and cracking of vital components [4], [6], [24]. Combined with high sediment load, vortex filaments and shed vortices can cause severe erosive damages on turbine components e.g. GVs and RBs [25], [26]. This makes the vortex shedding phenomenon a subject of concern. In this section a description of the basic flow mechanism and its characteristics will be given, while the two following sections presents the corresponding induced vibrations and a description specific for hydrofoils and vanes, respectively.

2.3.1 Basic Flow Mechanism

Any object in relative motion to a flow will induce a certain amount of vorticity in its BL, i.e. a rotating behavior for an infinitesimally small fluid element [27]. The strength of this generated vorticity depends on the velocity of the fluid, and the geometry and surface of the body. For steady flow at very low Reynolds numbers across symmetrical bodies, the flow and its associated boundary layers stay attached, and nature ensures a smooth flow when the fluid leaves the body. This flow regime is termed Stokes flow, and occurs in the range $0 < Re < 4$, with Re defined as

$$Re = \frac{\rho UL}{\mu} \quad (2.3)$$

where ρ and μ is the fluid density and dynamic viscosity, respectively, of a fluid with free stream velocity U past a body with characteristic length L [18].

If the Reynolds number is increased to the range $4 < Re < 40$, the BLs starts to separate from the body at separation points located on the body's upper and lower surface, and two symmetrically placed vortices are created in the near-wake of the body, as shown in 2.1, [14]. Once these vortices are created they are strengthened and fed by circulation from its connected shear layer [28]. A further increase to the region $40 < Re < 80$ generates a vorticity strength in the shear layer which causes the two shear layers to interact. The interaction between these two shear layers is considered the key element of vortex shedding [23]. At some point, one of the two vortices gain sufficient strength to draw its opposing shear layer across the wake. This cuts off further supply of circulation to the growing vortex, which is further shed off downstream, [23]. The location of where this instability occurs marks the closure of the near-wake, and is often referred to as the vortex formation length L_f as indicated in figure 2.1, [23].

Figure 2.3 presents the general behavior of the interaction; parts of the fluid in the wake (a), is entrained into a growing, downstream travelling vortex fed from the upper shear layer, while fluid from the opposing shear layer (b) is drawn across the wake and into the developing upper shear layer. The near-wake region between the body and the downstream-travelling vortex oscillates in size, and some further fluid is entrained into it (c). This interaction occurs in a periodical manner [29].

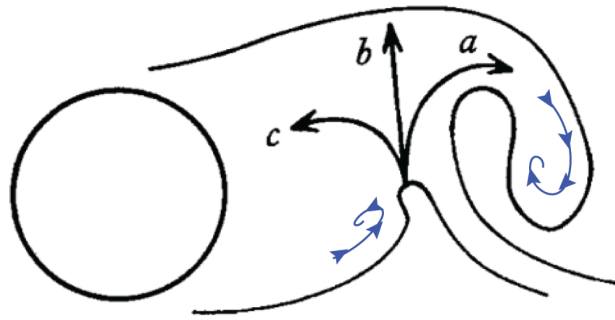


Figure 2.3 – Vortex formation indicating zones of fluid entrainment and rotation. Adapted and modified from [29].

The result is an alternating creation of vortices called vortex shedding, flowing downstream in a regular fashion creating a pattern known as a Karman vortex street as can be seen in figure 2.4.

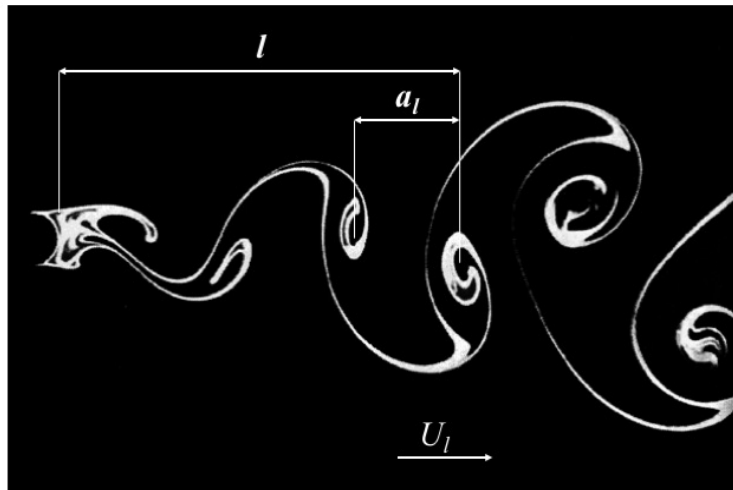


Figure 2.4 – Vortex creation and von Karman vortex street from a cylinder. Adapted and modified from [30]. Downstream distance and vortex pair-distance is indicated.

Once a vortex has been shed, its strength is dependent on its distance l from its feeding shear layer at the TE, as opposed to the free vortex where its strength is constant [18]. The strength, Γ_l , for a moving vortex may be determined as expressed in (2.4), [27]

$$\Gamma_l = 2\sqrt{2}U \left[\left(\frac{U_l}{U} \right) - ka_l \right] a_l \quad (2.4)$$

Here, U_l is the velocity outside the wake at position l and a_l is the longitudinal vortex spacing at location l . k is the slope of the frequency versus velocity curve, which will be discussed in the next section. As already mentioned, identifying and evaluating these parameters of the vortices may be challenging and depends on the method used to visualize the vortices.

A large amount of studies have been conducted in relating the vortex shedding characteristics to fluid flow parameters and body geometry, with the flow around a circular cylinder serving as the benchmark case study [23]. A linear dependency between the shedding frequency and

fluid flow velocity has been found, where the frequency and amplitude generally increases with the velocity for a wide range of Reynolds numbers, to be discussed in more detail in the next section [31]. Lienhard [16] presents an overview of the different results for the flow around a cylinder in table 2.1.

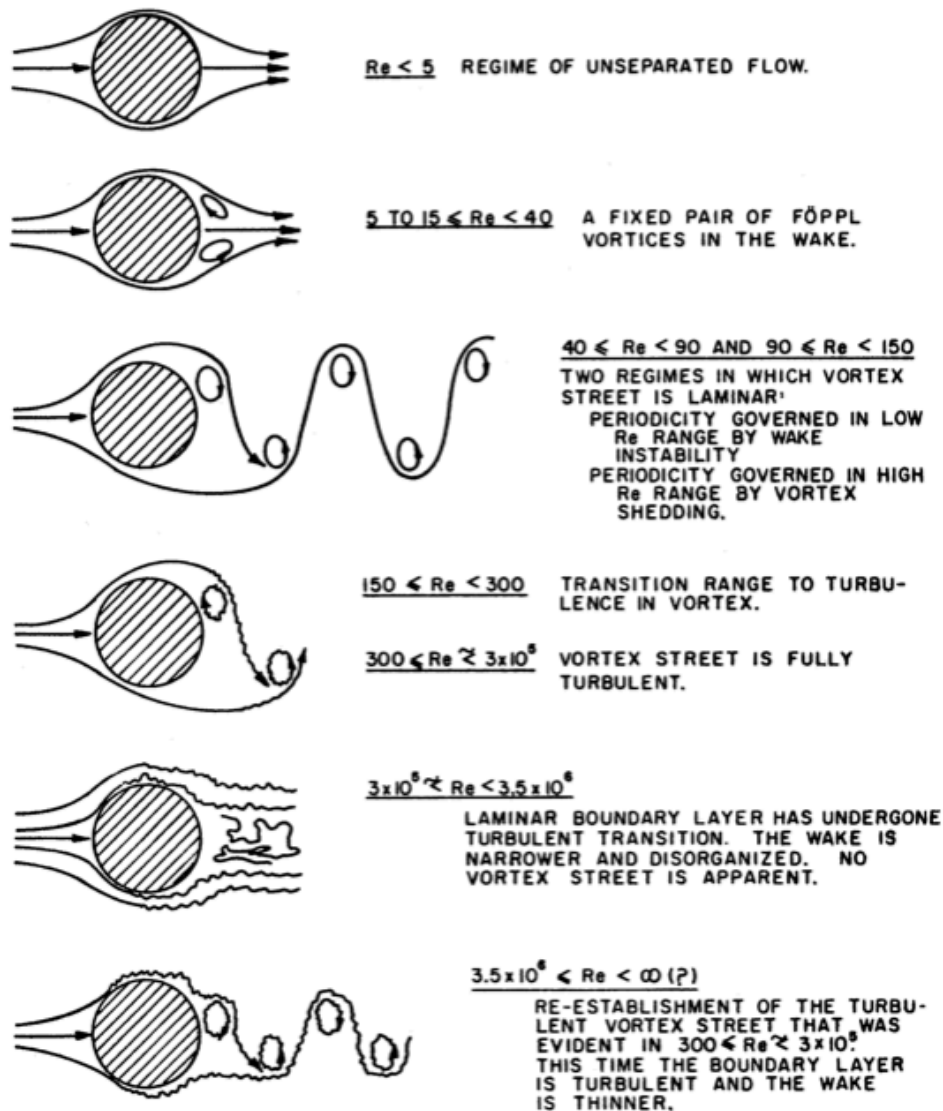


Table 2.1 – Regimes of vortex shedding and fluid flow past a cylinder. Adapted from [16].

Notice the size of the wake in the different regimes. At $Re > 3.5 \cdot 10^6$, a turbulent vortex street is apparent with a narrow wake width and vortex characteristics somewhat different than at laminar flow [16].

It is evident that vortex shedding involves interaction of boundary layers, shear layers and wakes, and a detailed analysis therefore becomes a complex procedure [32]. For a more thorough description of such an analysis, the reader is referred to Schlichting [14] or similar textbooks.

2.3.2 Strouhal Number

As vortex shedding is a phenomenon which depends on the geometry of the body inducing it, and the flow velocity of the passing fluid, it is for comparison reasons beneficial to describe it by means of a dimensionless number. The Strouhal number, St , commonly serves as such a dimensionless parameter, and describes the dimensionless vortex shedding frequency for a bluff body. For a free stream of velocity U , flowing past a bluff body of characteristic diameter D , creating vortices at a frequency f_s , the Strouhal number, or Strouhal law, may be defined as

$$St = \frac{f_s \cdot D}{U} \quad (2.5)$$

The relation in (2.5) was originally developed for bluff cylinders, but with slight modifications it is valid for a range of geometries, to be discussed in a later section.

There are several ways in which the dimensional vortex shedding frequency f_s may be determined. One obvious approach is to count the number of vortices, n_v , passing a certain area during a time-period of duration T , and determine the frequency using (2.6)

$$f_s = \frac{n_v}{T} \quad (2.6)$$

Another approach is to perform a spectral analysis of either pressure measurements or velocity measurements in the downstream region of the body, to be discussed in section 2.7 and 3.5.

Several studies have been performed to map the $St-Re$ relationship for cylinders, and the Strouhal number is found to generally increase with increasing Re , except in the range $10^3 < Re < 10^5$ where it remains relatively constant as shown in figure 2.5. In this region the majority of experimental studies normally results in Strouhal values in the range $0.18 < St < 0.24$ depending on the flow parameters and geometry, with $St = 0.2$ often serving as a guideline-value as indicated in the figure [6][14]. As is evident from (2.5), a constant Strouhal number implies a linear relationship between frequency and velocity.

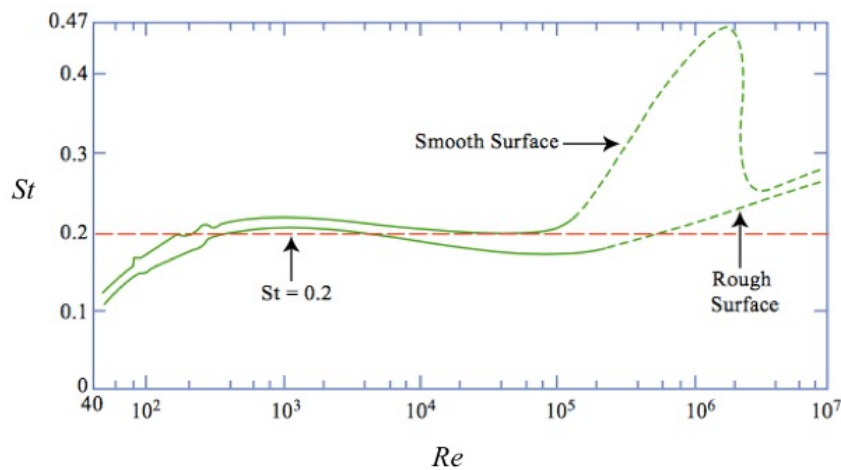


Figure 2.5 – Strouhal number dependency of Reynolds number for circular cylinders. Adapted from [33].

It is also found that in the turbulent vortex shedding regime, several frequencies coexist, and determining the vortex shedding frequency is a matter of determining the dominating frequency through a spectral analysis [16].

Although the above-mentioned parameters are geometry dependent, the results and theory for flow around a cylinder may serve as a valid reference for other similar geometries.

2.4 Flow Induced Vibration

As the vortices shed from a body receives its strength from the circulation around the body shedding the vortex, there is an obvious relation between circulation and vortex shedding. Each of the alternately shed vortices from the TE will generate a circulation around the body shedding them, with a direction opposing the rotational direction of the vortex, as stated by Kelvins circulation theorem and shown in figure 2.6, [18]. Circulation around the body does not necessarily impose a circulating motion of fluid around the body, but it is rather a mathematical term which describes the net rotational motion of fluid flow on the upper and lower surface [18]. A body generating circulation when exposed to a cross-flow, will experience a lift force according to the Kutta-Joukowski theorem, which will not be discussed in detail in this text [18]. Hence, for each of the alternately shed vortices, a transverse lift force is exerted on the object [27]. The strength and direction of this lift force depends on the amount and direction of circulation and fluid flow velocity [18].

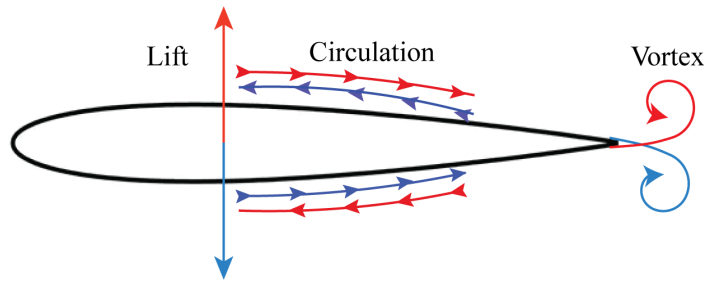


Figure 2.6 – Lift generation from vortex shedding. Hydrofoil geometry showing relation between directions of vortices, circulation and lift.

As a consequence, the body – a rod, plate, or in case of hydropower turbines, GVs, SVs or RBs, experiencing vortex shedding will inevitably experience a periodical lift force pulsating with the same frequency as the shedding frequency [27]. An oscillatory FSI occurs when a structure experiences strain due to such flow induced forces, deforms towards its original state to reduce the strain, but is forced back into the strained configuration again by the fluid [34]. The frequency of this pulsating reaction force is generally high for turbine components, which may lead to a large number of cycles resulting in mechanical damage from high-cycle fatigue [6]. Also, if the vortex induced vibration matches the natural frequency of the body, the body may resonate to dangerous levels [17].

2.4.1 Lock-In Phenomenon

If the structure experiencing the pulsating reaction force of the vortex shedding is sufficiently flexible, the oscillating FSI may feedback on the vortex shedding. This may in turn create a more intense and synchronized vortex shedding, resulting in a self-reinforcing process [6]. This means that the material's properties and its structural parameters plays a role in determining the vortex shedding frequency. More precisely; the structure's natural frequencies, f_n , affects the vortex shedding to a certain degree through FSI [6]. When the velocity past a body is increased, f_s increases according to the Strouhal law, (2.5), as seen in figure 2.7. As the shedding frequency approaches one of the structure's natural frequencies, the self-reinforcing situation occurs and persist until the deviation between the shedding frequency following the Strouhal-law and the natural frequency becomes too large [6]. The phenomenon of the shedding frequency remaining approximately constant while increasing the velocity is called *Lock-in* and may cause high-cycle fatigue loads in the structure experiencing it [6]. Whether a structure is locked-in or not may be answered by measuring the frequency development for a varying flow as shown in figure 2.7. Several studies show that in addition to maintaining a relatively stable frequency, the phenomenon also induces a substantial increase in vibrational amplitude causing increased stresses and noise [35]–[37].

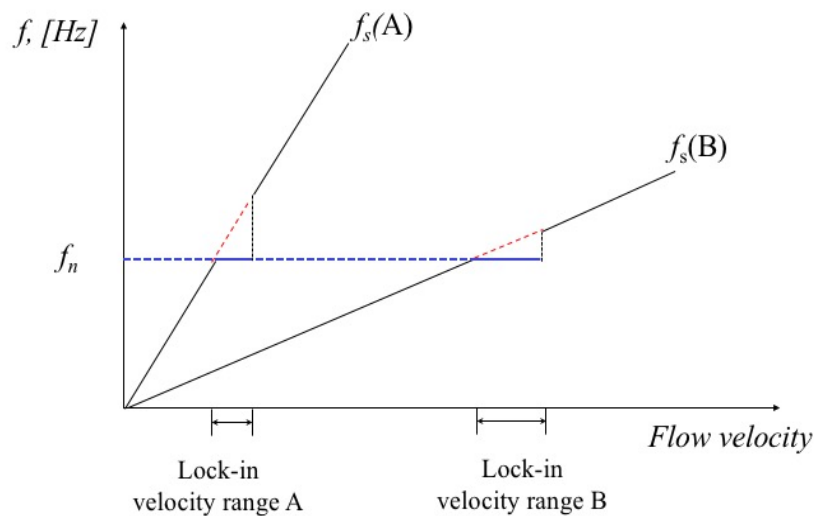


Figure 2.7 – Lock-in phenomenon. Sketch of vortex shedding frequency from structure A and B for a varying flow in relation to the structure’s natural frequency (blue). The red dashed lines indicates the shedding frequency in the absence of lock-in.

Figure 2.7 presents the lock-in behavior for two different structures; structure A and structure B. Note that structure A sheds vortices at a higher frequency than structure B, while they both have equal natural frequencies. The slope of the curves indicates the frequency increase per velocity increase, and serves as the parameter k utilized in (2.4). A modification of the structure which affects either the slope of this curve or the natural frequency will have a direct impact on the lock-in velocity range if lock-in is to occur. As an example; if one is able to reduce the shedding frequency of structure A to that of structure B without affecting the structure’s natural frequency, this will present a shift in lock-in velocity range to a higher one as indicated in the figure, and lock-in in velocity range A is thereby avoided. In a waterpower context, this may be exploited to avoid lock-in in certain components to occur in the operating range of the turbine.

In the figure, the natural frequencies are indicated to be constant, independent of flow velocity. Studies have shown that this is not the case, as experiments have revealed the natural frequency to vary depending on both the type of fluid it is surrounded by and the fluid flow velocity, due to the effect of hydrodynamic damping and added mass [38]–[41]. For a body submerged in water, a significant decrease in natural frequency compared to when surrounded by air has been observed [42], while a slight increase is observed as a consequence of increased velocity [41]. The presence of cavitation has also been found to significantly increase the natural frequency of hydrofoils [43].

2.5 Hydrofoils and Vanes

Due to its fundamental importance and the wide range of applications, the flow around a cylinder has, as already mentioned, served as the base study in investigations of vortex shedding and FSI [23]. In contrast, such studies have been performed in much less extent for hydrofoils and vanes, particularly for high Re -numbers, despite numerous practical applications [44]. Concerning the objective of this thesis, the flow over a hydrofoil and the relation between the downstream flow field and the foil's TE is of particular interest.

2.5.1 Flow over Hydrofoils

As a consequence from the development of aviation-, hydro- and marine-technology, an enormous amount of research has been directed towards the development of streamlined-shaped geometries generating lift in gas and fluids – i.e. airfoils and hydrofoils, respectively [15]. This has led to an increased understanding of the relation between design, the resulting flow and the corresponding forces occurring. In a hydropower context, this knowledge has been utilized in the design of RBs, SVs and GVs, leading to higher efficiencies and reduction of undesired effects such as noise, high-cycle fatigue and mechanical failures. A hydrofoil will, due to its more streamlined shape compared to a cylinder, generate a smoother flow and a more narrow wake [13]. Although smoother, the flow is still quite complex, consisting of free shear flows, vortices and mixing zones.

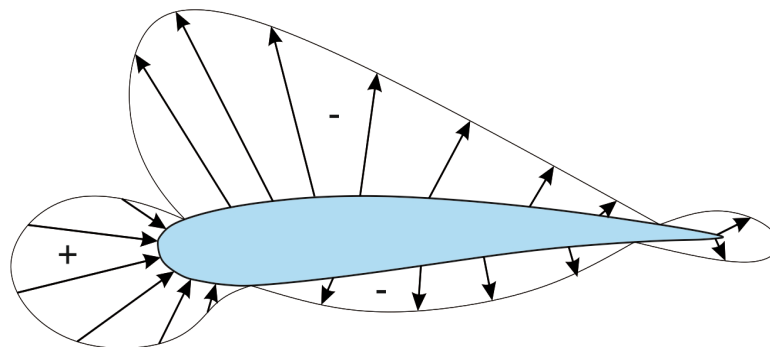


Figure 2.8 – Typical relative pressure distribution along a hydrofoil. Notice the (+) and (-) representing the sign of the relative pressure compared to the stagnation pressure. Adapted from [45].

As fluid flows past a hydrofoil it will be distributed in a manner determined by the geometry of the hydrofoil, causing a certain drag and possibly lift to be generated. These forces are generally related to the pressure distribution, which for a non-symmetrical hydrofoil is typically as shown in figure 2.8. The + and - sign refers to the sign of the relative pressure compared to the stagnation pressure. There is an obvious pressure difference, which inevitably results in the generation of a corresponding lift force in the upwards direction. The lift force may also be explained in terms of circulation theory, which will not be further discussed [18].

As explained and shown in figure 2.6, vortex shedding generates an alternating lift force on the foil,

Vortex shedding also occur for hydrofoils, and the alternating lift force presented in figure 2.6 with the resulting structural vibrations thereby also occur for hydrofoils [46]. Regarding

determination of shedding frequency, the TE thickness would be an appropriate characteristic diameter for hydrofoils, as this determines the scale of the swirls generated [6].

It is evident that the design of the hydrofoil has a direct impact on the pressure distribution and the resulting lift along the entire foil, including at the TE. Gaining a full understanding of the interactions and resulting flow for hydrofoils is a complex procedure, but it presents the opportunity of controlling the pressure distribution, forces and wake by means of design modifications [18]. Increased knowledge and understanding of flow over foils has led to several improvements for hydropower turbine components e.g. the TE modifications of RBs and SVs during the 70s mentioned in Chapter 1.

2.5.2 Trailing Edge Profiles and Mitigation of Vortex Shedding

The basics of flow induced vibrations in hydrofoils and its relation to TEs were laid by Gongwer [31], Donaldson [47] and Heskestad and Olberts [27] during the 50's and 60's. These fundamental studies investigated relations between vortex shedding frequency and amplitude for two dimensional TE geometries, where the TE geometry was found to play a major role in the wake dynamics and resulting structural vibrations. In more recent years, attention has been directed towards three-dimensional modifications of TEs, but such investigations have been performed solely for airfoils. This section presents an overview of the studies that have been performed in relating TE geometry to vortex shedding and mitigation of its effects.

Two-Dimensional Trailing Edges

In his study of flow induced vibrations of vanes in water, Gongwer found the Strouhal-parameter in (2.5) to not be rigidly determined for slender bodies such as hydrofoils, and suggested a correction which took the BL displacement thickness into account. For a range of Reynolds numbers, he found the Strouhal number to be constant and equal to 0.19. His correction suggested the vortex shedding frequency to be inversely proportional to the TE thickness t with a virtual BL thickness δ' added to it, rather to the characteristic diameter as in the original equation. His correction is presented in (2.7).

$$St = \frac{f_s(t + \delta')}{U} \quad (2.7)$$

Where δ' is experimentally determined as a fraction of 0.643 of the displacement thickness of a turbulent BL, defined in (2.8).

$$\delta' = 0.643 \cdot \frac{1}{8} \cdot \frac{0.37L}{Re^{\frac{1}{5}}} \quad (2.8)$$

Donaldson presented a detailed study from his research on the effect of modifying TE geometries of RBs. Focusing mainly on the forces from vortex shedding at the TE on the runner construction, he found that modifying the TE significantly reduced the vibrational amplitude of the structure. The frequency, on the other hand, did not change significantly. Oblique, truncated, symmetrically tapered and cavity edges were all utilized in his study, where the asymmetrical ones displayed attenuation while the symmetrical ones amplified the vibration. His investigations showed a substantial reduction in structural vibrational amplitude

using the so-called *Donaldson's cut* consisting of a combination of a straight 45° cut and a third order polynomial curve [41].

Heskestad and Olberts [27] presented an even more systematic approach to the geometries studied by Donaldson, with a detailed study on the variation of angles for the different geometries. As opposed to Gongwer and Donaldson, they found the vortex shedding frequency to be highly dependent on the shape of the TE. Figure 2.9 serves as a visual representation of their findings. For symmetrical TEs it was found that more acute TE angles to a certain degree allowed for an increase in vortex strength and reduction in frequency due to the TE protrusion serving as a separating wall between the upper and lower shear layers, represented by (a) in the figure. For non-symmetrical TEs (b) it was found that for certain distances between the separation points, the upper and lower vortices could achieve a mutual destructive effect, with mitigation of vortex strength as result. Their findings also suggested that by decreasing the distance between the separation points at the TE, the vortex shedding frequency and vortex strength could be significantly increased and decreased, respectively. This corresponds to going from (c) to (d) in the figure.

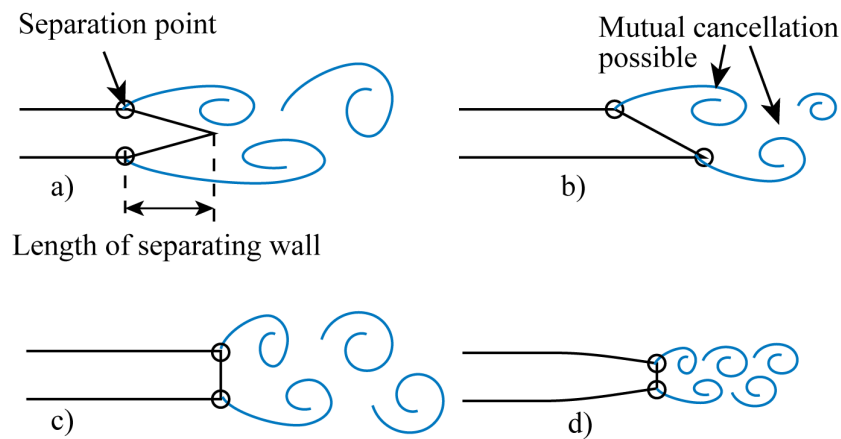


Figure 2.9 – Vortex characteristics from a symmetrical (a), oblique (b), thick blunt (c) and thin blunt trailing edge. Large spirals indicate high strength. Shorter distances between spirals indicate higher frequencies.

Based on the research by Heskestad and Olberts, Antonsen and Nielsen [48] presented a modified formula, (2.9), for calculating the Strouhal number for hydrofoils, which also included the geometry of the TE.

$$St = \frac{100 f_s (t + \delta')}{B U} \quad (2.9)$$

Here, B , is a geometric factor depending on the TE. Its value may be found in table 2.2, which also shows the relative amplitude, A , compared to the blunt edge.

By assuming a constant Strouhal value of 0.19, in addition to assuming a constant virtual BL displacement thickness of 0.56 mm , Brekke [4] presented a simplified suggestion:

$$f_s = 190 \cdot \frac{B}{100} \cdot \frac{U}{t + 0.56} \quad (2.10)$$

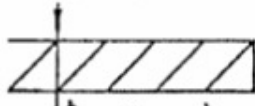
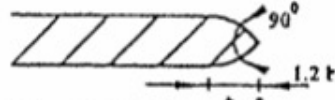
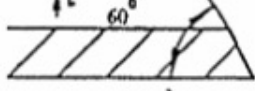
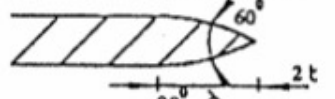
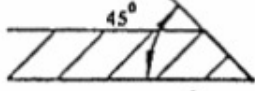
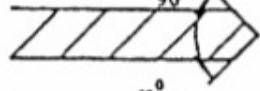
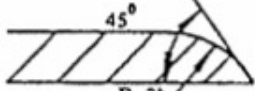
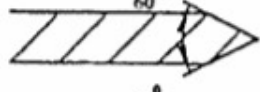
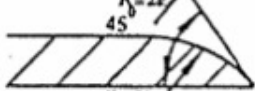
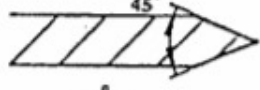
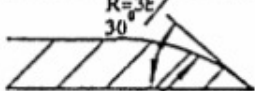
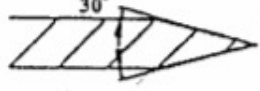
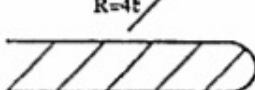
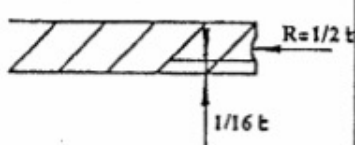
	A	B		A	B
	100 (100)	100		(0)	
	(48)			(0)	
	38 (20)	112		190 (230)	96
	3 (0)	131		380 (360)	93
	0	149		43	117
	0	181		0	159
	(260)			31 (43)	103

Table 2.2 – Trailing edges of vanes with relative amplitude A and values of B to be used in (2.9) and (2.10). Adapted from [4].

By use of (2.7)-(2.10) it is possible to perform estimations of vortex shedding frequencies and Strouhal values for a range of TEs for hydrofoils. Although the value of 0.19 is often used, the Strouhal number for hydrofoils has been found to vary in the range 0.15 to 0.3 [49]. These estimations, together with the data from table 2.2, may be used as a comparative tool for both vortex shedding frequency and amplitude acquired through simulations or experimental measurements.

In more recent years, Zobeiri et. al [44] performed experimental investigations of vortex shedding dynamics in the wake of oblique and blunt TEs for NACA0009 hydrofoils. They found that vortex induced vibrations were significantly reduced in the case of having an oblique TE compared to a blunt one. They point at the disorganization of the vortex street in the wake of the hydrofoil as the reason for the reduction, which further confirmed the observations by Heskestad and Olberts of mutual destruction between vortex pairs from the upper and lower edge.

In addition to being highly dependent on the TE geometry, studies have also shown that the vortex shedding frequency from hydrofoils may be influenced by the presence of cavitation

[50]–[52]. Ausoni [37] has found the vortex shedding frequency to increase up to 15 % in the presence of fully developed cavitation, with vortex-induced vibration occurring already at an early stage of cavitation.

Although this extensive research has been conducted with several effective geometries developed as a result, the physics of the complex flow and its resulting problems still remains quite poorly understood [44]. Today it is recommended to have a skewed cut TE for GVs, RBs and SVs, with an angle less than 45° relative to the pressure side of the vane [4]. Poor vane design has in several cases been the main reason for blade cracking and defects, and has also been the cause for so-called *singing vanes* at certain conditions [1], [4], [35].

Three-Dimensional Trailing Edges

As already mentioned, neither the author or the TTO at NTNU know of any studies on spanwise modification of TEs of hydrofoils. For airfoils, however, such studies have been performed both numerically and experimentally, with some of the geometries presented in figure 2.10. Although hydrofoils and airfoils have different areas of application, the results obtained through research on airfoils are expected to be applicable for hydrofoils as they to a large extent follow the same physics. A short review of some chosen studies is therefore of interest and given in the following paragraph.

Thomareis and Papadakis [53] performed simulations of flow around a NACA 0012 airfoil for serrated edges, observing that a serrated edge creates a spanwise pressure gradient responsible for the development of secondary flow patterns in the spanwise direction. Further, they observed that the velocity deficit in a trough is less than at a protrusion of the edge, resulting in a spanwise decorrelation of vortices and a strong dampening of their strength.

Nedic and Vassilicos [54] performed experimental measurements on a NACA0012 airfoil on a range of TEs. By adding non-flat TEs to the airfoil they were able to reduce the energy of the vortex shedding significantly, as long as the chevron-angle was lower than 45° , i.e. by making them sharper. Yang and Baeder [55] performed simulations of flow over a spanwise wavy flatback TE, resulting in a reduction in drag on the foil and a reduction of flow separation and vortex shedding at the TE compared to the unmodified blunt edge.

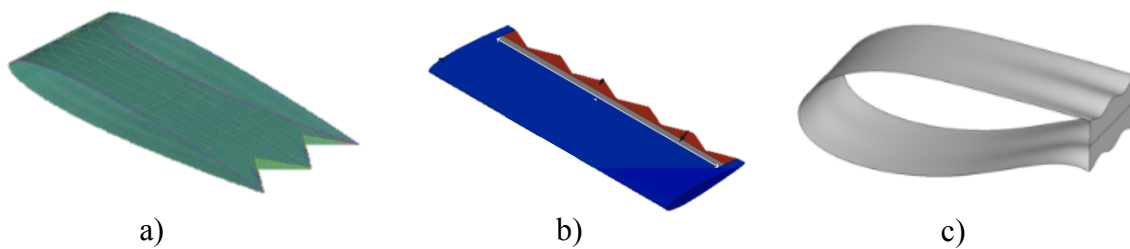


Figure 2.10 – The experimentally and numerically investigated airfoil trailing edges by a) Thomareis and Papadakis, b) Nedic and Vassilicos, c) Yang and Baeder. Adapted from [53][54][55] respectively.

Several studies have also been conducted in adding sharp sawtooth geometries to wind-turbine blades to reduce acoustic noise production, with a significant decrease of noise as the result [56]–[59].

To summarize, blunt TEs generates strong, but low frequency vortex shedding, while sharp protrusions do the opposite. Serrations combine these properties and exploit the mitigative effect of vortex decorrelation.

2.5.3 Guide Vanes

The GVs, or the cascade of GVs called wicket gate, serves the purpose of controlling the velocity field and generate spin of the water entering the turbine runner. By varying the GVs angle of attack in the wicket gate, the water's direction in the vaneless space can be adjusted. Varying the angle of the GVs also controls the volumetric flow rate and the resulting delivered power to the grid. It is desired to have an ideal velocity field similar to that of a free vortex in the vaneless space so that the resulting pressure pulsations and possible damages are avoided [60]. The wicket gate is the last turbine component to mechanically interfere with the water before it enters the runner. Its design and use therefore becomes crucial for obtaining the desired velocity field in the runner, and thereby in achieving the desired efficiency and lifetime of the turbine. The process and methods of GV design will not be discussed here, but a brief overview may be found in [60].

As previously described, pressure pulsations, vibrations and FSI are acquiring an increasing amount of attention due to new design methods and optimization. RSI between runner and GVs and the geometry of both is therefore an area in need of attention. In a hydropower context, the majority of studies on TE modifications have considered modifications on geometries such as SVs and RBs [6]. Modifying the TEs of GVs to reduce vortex shedding remain a field less explored [6]. It is of high interest to reduce pulsations wherever they may exist in the turbine, and being a less investigated field it is believed that improvements in GV design regarding these pressure pulsations may be obtained.

2.6 Rotor–Stator Interaction

The flow in the vaneless space is in the ideal case not affected by the runner, and the free vortex flow described in section 2.2 is applicable to describe the flow field [60]. In the real case, however, the flow in the vaneless space is affected by the geometry and design of both wicket gate and runner [61]. The wakes from the individual GVs affects the pressure- and velocity distribution in the vaneless space, which in turn affects the inlet conditions in the runner, as indicated in figure 2.11. By sharing this vaneless space pressure- and velocity distribution there is a rotor-stator dependency between the runner and wicket gate, i.e. a RSI. From a rotating frame of reference a runner blade will experience an excitation each time it passes a GV, represented by the circled areas in figure 2.11. From a static frame of reference a GV will experience an excitation each time it is passed by a runner blade. These pressure pulsations propagates through the turbine and affects several turbine components [4]. This result in a dynamic force on both RBs and GVs, but also on the SVs and spiral casing, with frequencies depending on the number of GVs, RBs and the rotating speed of the turbine [4]. The fluctuating force experienced by RBs is considered to be the main cause for cracking in Francis-runners [62].

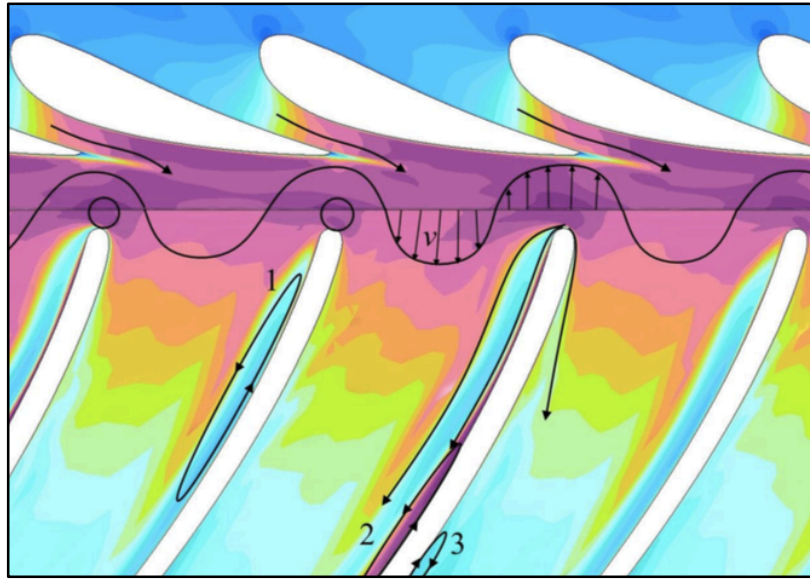


Figure 2.11 – Rotor-stator interaction between runner and wicket gate. Vortices are created at 1, 2 and 3. Pressure pulses are created at the circled areas. Adapted from [61].

Trivedi [61] has carried out numerous studies on pressure loads in transient operations of hydro power turbines. His experimental and numerical study on the RSI for a high head Francis turbine shows a high increase in pressure amplitudes occurring in the runner due to RSI. Vortex formations in the wakes of the GVs were found responsible for asymmetrically pressure rises in both the rotating and stationary frame of references, which in turn created high and unequal stresses on RBs. Figure 2.12 shows the numerically calculated pressure distribution in the SVs and GVs for a model at high discharge operation together with the resulting average pressure distribution along the runner blade.

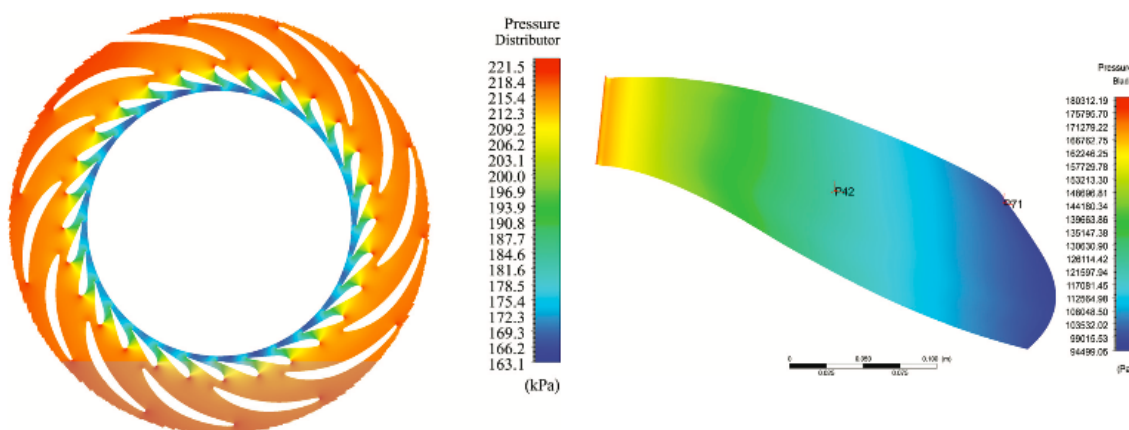


Figure 2.12 – Pressure distribution in stay vanes and guide vanes prior to runner inlet (left) and average pressure distribution along runner blade surface (right). Operational point of volumetric flow $Q = 0.22 \text{ m}^3/\text{s}$ for a turbine of $Q_{BEP} = 0.20 \text{ m}^3/\text{s}$. Adapted from [61].

High amplitude peaks and valleys were observed during pressure-time measurements, where the RBs passed the GVs. Trivedi also found that oscillations in turbine torque were coupled to

RSI and the sequence of interactions. Further, he confirms the behavior as sketched in figure 2.11 by numerically measuring an unsteady vortical flow rotating inside the blade rows.

From the presented considerations it is evident that pressure pulsations occurring in the vaneless space creates a RSI, which in turn generates a vibrational torque possibly causing high-cycle fatigue damage in the structure of the turbine. These damages may lead to a shorter lifetime, high maintenance cost and, most importantly, a loss in power production and resulting income. It may also be believed that vortices and eddy-swirls in the runner presents a loss in the hydraulic efficiency, which in turn is directly related to a loss in the total efficiency of the turbine. It is therefore of high interest to be able to reduce pressure pulsations. If the suggested hydrofoil modifications presented in this work, work as intended, it could be implemented in GVs to achieve a more uniform velocity field in the vaneless space and reduce the undesired effects of RSI.

2.7 Spectral Analysis

When a signal is a pure sine or cosine wave, determining its frequency is a simple process. The general time-varying signal, however, does not have the simple form of such smooth signals. They usually consist of multiple frequencies, including disturbances, where each frequency's impact on the resulting recorded signal varies. It is found that complicated time-varying signals may be considered to be constructed of a sum of sine or cosine waves of different frequencies [63]. The component frequencies may be determined through the process of spectral analysis. There are several ways of performing such analysis, but the one to be utilized in this work will be the Fourier transform. The Fourier transform is a generalization of Fourier series and may be applied to any practical function [63]. A time varying signal is used as input for the transform, and a frequency-domain representation, or power spectrum, is the resulting output as shown in figure 2.13.

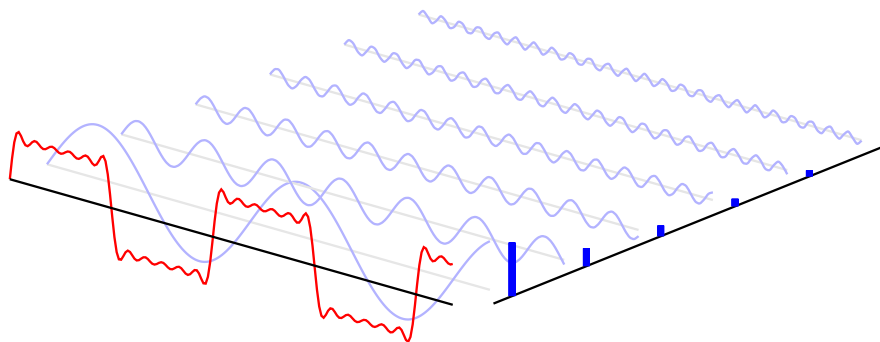


Figure 2.13 – Fourier transform of time-varying signal (red) to its corresponding frequency domain representation (blue). Adapted from [64].

By performing such an analysis one can achieve an understanding of which frequencies are the dominating one in the measured signal. The mathematical details regarding the Fourier transform itself will not be discussed here but may be found in literature [63].

For the Fourier analysis of a signal to give an accurate frequency domain representation it is crucial that the signal has been recorded with a sufficient sampling rate. For a signal with

frequency f , the required sampling rate to properly describe this signal, f_{sample} , is given by the sampling-rate theorem [63]:

$$f_{sample} > 2f \quad (2.11)$$

The required number of samples is determined by the desired frequency resolution in the power spectrum. For a sampling lasting for T seconds, the resulting frequency increment Δf , is determined by

$$\Delta f = \frac{1}{T} \quad (2.12)$$

2.8 Uncertainty Analysis

Any experimental measurement will involve some level of error or uncertainty. An error may be defined as the difference between the measured value and the true value of the physical property in question, i.e. the measurand. The error in a measurement is generally not known, but may be estimated through use of statistical methods. From a set of measurements, these statistical methods may be applied to define confidence intervals which determines the range of where the value of the measurand will lie within, with a certain probability. A confidence level of 95 % is commonly used to determine this interval [63].

In the work to be presented, the following uncertainties will be considered:

- Random uncertainty
- Systematic uncertainty
- Spurious uncertainty

Random uncertainty is the imprecision in the measurement, caused by independent fluctuations in the measurements apparatus due to instrumental or environmental conditions [63]. These fluctuations cause the output of the instrument to fluctuate despite a constant value of the measurand. Based on the instrument's output, the standard deviation of the sample may be determined and used to describe the random uncertainty. For a sample of j measurements of the variable x and mean value \bar{x} , the standard deviation S_x of the sample of size n may be determined according to (2.13)

$$S_x = \left(\sum_{i=1}^j \frac{(x_i - \bar{x})^2}{n - 1} \right)^{\frac{1}{2}} \quad (2.13)$$

For a system with m random errors in measurements of variable X , the total standard deviation, S_X , may be estimated using (2.14), [63]

$$S_X = \left[\sum_{i=1}^m S_i^2 \right]^{\frac{1}{2}} \quad (2.14)$$

Depending on the sample size, the random uncertainty may be estimated using a *Gaussian distribution* or *Student-t distribution*. For a sample of size N with a standard deviation of S_X , the random uncertainty P_X may be estimated as

$$P_X = \pm t_{\alpha/2} \frac{S_X}{\sqrt{N}} \quad (2.15)$$

where $t_{\alpha/2}$ is the t-value determined on the basis of the degree of freedom and confidence level $1 - \alpha$, [63]. For a sufficiently high number of N the t-distribution will approach that of the Gaussian distribution.2.15

Systematic uncertainty is related to errors that have not been eliminated through calibration, which are often related to an error in, or improper use of, the measurement instrument [63]. Systematic errors are independent of sample size and remains constant if the test is repeated under the same conditions, and does therefore not lend itself to the statistical analysis applicable for random errors [63]. The systematic uncertainty may be determined by analysis of manufacturer's specifications, calibration tests and comparisons with independent measurement tests, among others [63]. Generally, for a system with n system uncertainties of value B_x , the total systematic uncertainty B_X , in the measurement of X , may be estimated using (2.16), [63].

$$B_X = \left[\sum_{i=1}^n B_i^2 \right]^{\frac{1}{2}} \quad (2.16)$$

Spurious uncertainty describes errors caused by human error or instrument malfunction. Such errors should usually be recognized during evaluation of the results, and may to a higher degree be visible when comparing repeated measurements. Datasets containing spurious errors should be discarded from the statistical analysis or expression of total uncertainty as they may invalidate the entire dataset [63]. In some cases, spurious errors only occur in some of the measured values in a sample and may be observed as so called *outliers*, i.e. measurements values which are out of line compared to the rest in the dataset.

With the above mentioned uncertainties in mind, the total uncertainty, w_x , may be calculated using the concept of *root of the sum of the squares* (RSS) as shown in (2.17)

$$w_x = \sqrt{B_X^2 + P_X^2} \quad (2.17)$$

Chapter 3

Particle Image Velocimetry

PIV is an optical and non-intrusive method used to investigate the velocity distribution of a chosen region of a fluid flow. In short, the method utilizes small seeding particles, high frequency lasers and cameras to obtain a high resolved vector representation of the momentary or developing velocity field of a fluid flow. From this velocity field one can also calculate other descriptive flow phenomena such as vorticity, vortex shedding frequency, turbulent kinetic energy (TKE) and swirling strengths. The following chapter gives a detailed description of the working principle of PIV and optimizations for proper measurements, followed by a description of some of the pre- and post-processing that may be performed on the measured data.

Remark: This chapter builds on the literature review carried out by the author as part of specialisation project TEP4540, and as such, parts of the chapter have been reproduced/reused therefrom [3].

3.1 Working Principle

A schematic representation of the working principle of PIV is presented in figure 3.1. The fluid is polluted with seeding particles, i.e. particles with density similar to the fluid analysed, and these are assumed to follow the fluid dynamics perfectly. Due to the particle properties, light is reflected when they are illuminated. By illuminating a certain area of interest (AOI) of the flow, and at the same time taking a picture of it with a high-speed camera, it is possible to get an image frame showing the momentary position of each particle within the AOI. By taking two pictures separated in time, an image pair with the momentary position of the particles in both images is achieved. Knowing the change of position of each particle over time may then be used to determine the velocity of the particles and thereby the fluid.

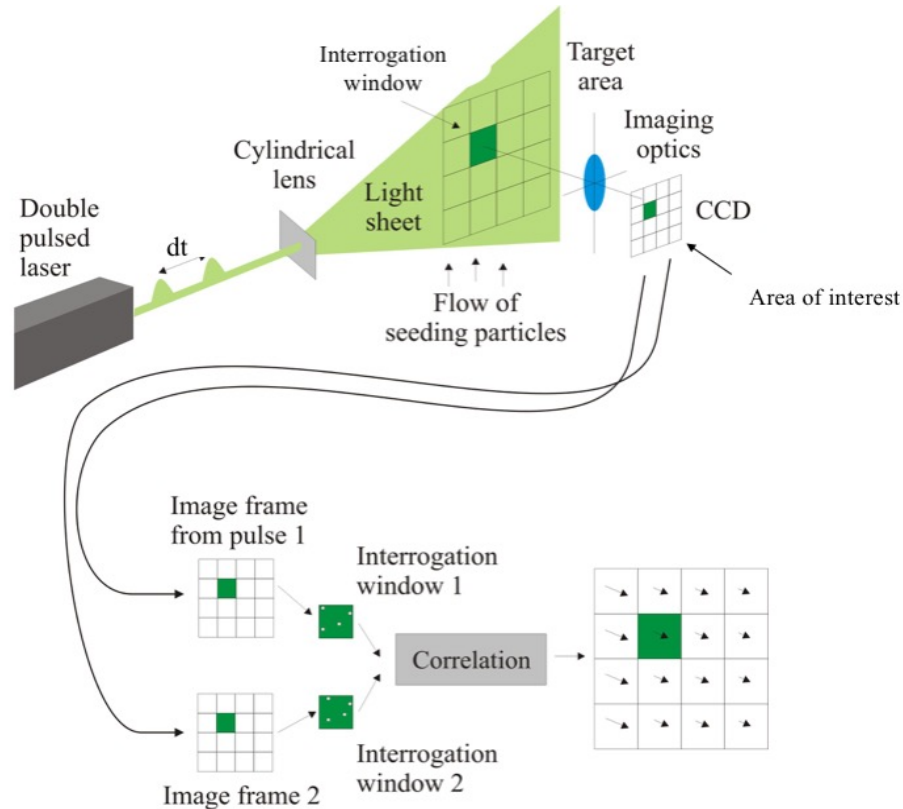


Figure 3.1 – PIV working principle figure. Adapted from [65].

Each image frame is divided into several interrogation windows (IW) of a specified size, n_{IW} . As an example, $n_{IW} = 32$ gives an IW of 32×32 pixels. If the illumination and camera frequency is known, the velocity of each particle can be calculated as distance travelled between the two frames per laser pulse separation time, commonly referred to as the dt of the system. This gives a single vector representing the average velocity in the IW. The challenge lies in identifying the corresponding particles in all image pairs and image windows so that the direction and amplitude of the resulting velocity vector is correct. This is done using an advanced software that can recognize particles through statistical analysis and cross-correlation calculations.

For the PIV-analysis to give accurate measurements it is crucial that the system settings and experimental setup are adjusted and optimized according to the flow to be investigated. Depending on the amount of information known of the flow to be studied prior to measurements, the optimization procedure is a somewhat iterative process as shown in figure 3.2. The degree of accuracy and image-, time- and vector resolution required are also decisive factors in the optimization procedure. One generally needs to set up the experimental setup, perform the measurements, evaluate the results and perform adjustments for optimization if necessary, followed by a repetition of the measurements. Previous studies have found certain rules of thumb, or design-rules, that may be utilized to increase the accuracy, reduce the number of spurious vectors and the uncertainty in the measurements. These rules will be discussed in the following sections.

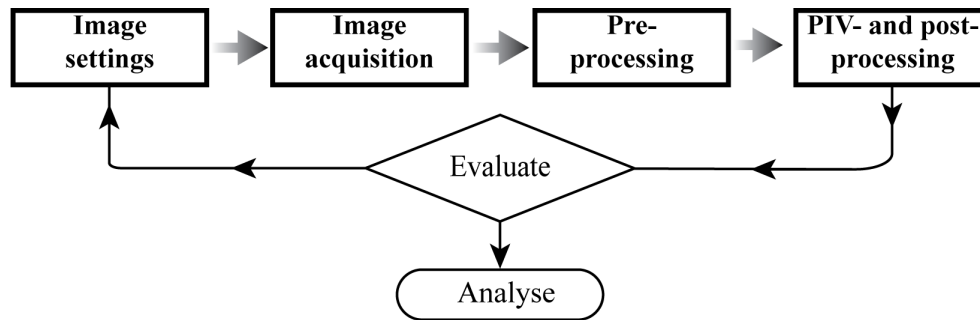


Figure 3.2 – General procedure of PIV measurements.

3.2 Image settings

Image settings are related to the settings of camera resolution, field of view (FOV), IW, particle size, camera sensitivity and seeding particle density. Prior to measurements, evaluations regarding the dimensions of the flow phenomenon to be studied should be performed to get an opinion of the requirements of these settings.

Design Rules

- The FOV should be set such that the entire camera chip is used to capture the flow structure of interest [66].
- For spatial calibration, the AOI should contain 20-30 markers of 10 px diameter [67].
- All particles within one IW should move uniformly [67].
- An IW should contain approximately 10 particles [68].
- Each particle should have an image size of approximately 2 pixels [68].
- The camera's entire dynamic range should be utilized [69].

The size of the FOV is adjusted by the relation between camera distance to the AOI and camera lens. This relation should be set such that the entire image chip is used to capture the observed flow structure of interest. This ensures maximum image resolution of the structure, i.e. maximization of image size to structure size ratio. If the FOV is chosen too large for investigations of a certain phenomenon, the desired flow structure may have too few pixels to even be visible.

When the camera has been positioned, the system should be calibrated to obtain correct measurements of positions and velocities. If the view of the AOI is distorted, e.g. due to an oblique viewing or curved windows, a spatial calibration is necessary to achieve proper accuracy. Depending on the setup, such a calibration is usually performed by placing a two- or three-dimensional calibration plate of dots of known size and position in the AOI. This plate is generated by the PIV-software, and by relating this known pattern to the camera's calibration image, a spatial scaling may be performed, i.e. by relating real distance to pixel distance. The accuracy, of this scaling depends on the dimensions of the dotted plate, the degree of optical distortion and the size of the pixels, which further depends on the resolution of the camera [66]. Having approximately 20-30 dots within the AOI, with a dot pixel-

diameter of approximately 10 px is shown to increase the accuracy, and may be used as a rule of thumb [67].

The choice of IW size depends on the desired vector resolution in the PIV-analysis, and the structural size of the flow, and is one of the most important PIV-parameters. If the IW size is too big, the movement of the flow phenomena will not be properly resolved by the single vector for the IW, as shown in figure 3.3a. It is required that all particles within one IW move uniformly as in figure 3.3b, to assure a good contribution to the cross-correlation in the PIV-analysis [70]. This way, the required size of the IW is determined by the size of the smallest flow structure of interest.

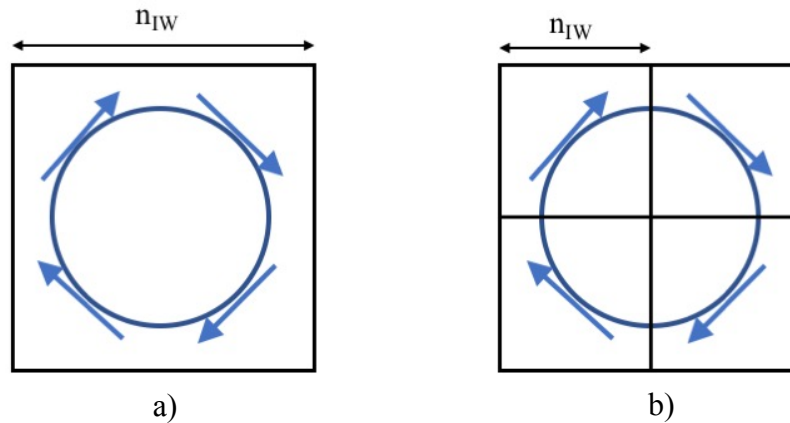


Figure 3.3 – Vortex description with a too large IW size (a) and suitable IW size (b).

The size of the seeding particles should be small enough to follow the flow phenomenon of interest. Smaller particles give a better flow tracking but less light scattering, and a compromise between reducing the particle size to improve particle tracking, and increasing the particle size to improve light scattering is therefore necessary [71]. The amount of seeding particles depends on the size of the FOV and size of the IW, which in turn depends on the physics of the flow [72]. Having at least 10 particles per IW and a digital pixel size of approximately 2 px is shown to give small bias errors and may be used as a rule of thumb [66], [68], [73]. Using figure 3.3 as an example, the IW in (a) require 10 particles, while the same area, i.e. the area covering the vortex flow, using half the IW size would require four times the seeding density as each of the four IWs in (b) requires 10 particles. Note that the *image seeding density* remains unchanged while the *real seeding density* increases for such a reduction in IW size. The total amount of seeding in the real flow is therefore solely dependent on the size of the AOI and IW, which further depends on the size of the fluid structure to be investigated.

The laser intensity and camera setting should be set such that the camera image chip's entire dynamic range is utilized for registering particle illumination [69]. Having too powerful illumination may cause the camera chip to be saturated, and neighboring particles may appear to “melt” together, giving errors in particle location and size [69].

Additional considerations

Laser light-reflections may occur, and the surrounding enclosure of the flow should be painted black or with a fluorescent paint to avoid zones of light-saturation and illumination of particles outside the AOI [70].

As light travels from one medium to another, light refraction will occur. Depending on the medium's or material's index of refraction, the direction of the incoming light will change direction at the boundary between the mediums. For the experiment in this thesis, plexiglas, air and water will be the mediums of which laser light will pass through. Although the refraction index for water and acrylic glass are close to equal, similar studies show a projection of shadows at the LE and TE of GVs depending on the radius of the curvature at the LE and TE, as shown in figure 2.4 [74][75]. Such shadows are shown to generate a high degree of spurious vectors, and should be avoided in the AOI to the extent possible.

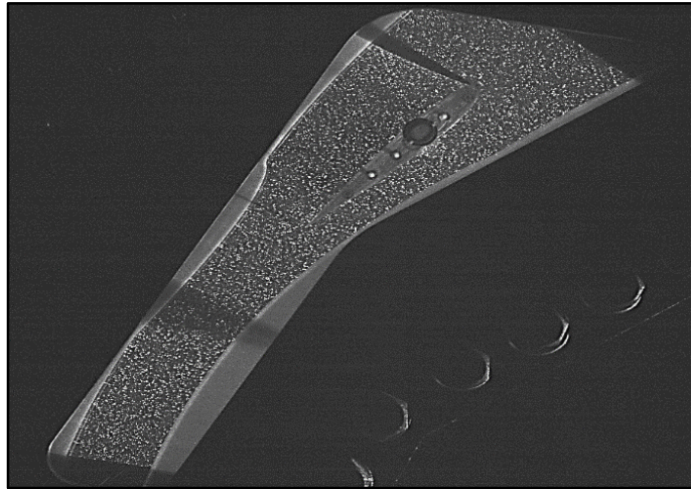


Figure 2.4 – Light refraction due to surface curvature for PIV-measurements on a guide vane. Adapted from [75].

3.3 Image Acquisition

There are several ways in how images using high speed cameras may be recorded. Images for PIV analysis are mainly recorded as so called *single-frames* or *double-frames* [67]. In general, in single-frame mode, one frame is recorded and stored as one image, while in double-frame mode, two illuminations are recorded in two separate frames, stored as one image. In both cases, the PIV-analysis compares two subsequent frames of images captured at a certain frequency. Generally it is desired to have an as high resolution and frequency as possible, but the camera has its limitations. Higher resolution comes at the cost of a lower camera frame rate, and higher frame rates comes at the cost of lower resolution.

Independent of recording method, there are also certain rules of thumb that should be utilized to acquire images in a manner which reduces errors and increases the quality of the PIV-analysis.

Recording Rules

- The system frequency should be set according to the sampling rate theorem [63]
- The dt should be set such that the maximum particle shift is less than a quarter of the IW size [68].

For investigations of a dynamic phenomenon, the camera's recording frequency should be set according to (2.11) to properly capture the frequencies occurring in the flow.

Further, the dt should be set such that the maximum particle movement is below a quarter of the IW size;

$$0.1 \text{ pixel} < |ds| < 0.25n_{IW} \quad (3.1)$$

Having a mean particle shift of 5 *pixels* is shown to give a good contribution to the correlation technique, and may be used as a rule of thumb [70][68].

Figure 3.5 presents an IW where the IW size, particle movement and size is indicated. If the dt is set too high, particles may move outside the IW between two frames, and having it too low gives too small particle movement for a proper velocity calculation. The system's minimum dt is limited by the laser and camera properties, and decides the maximum flow velocity that may be investigated [73].

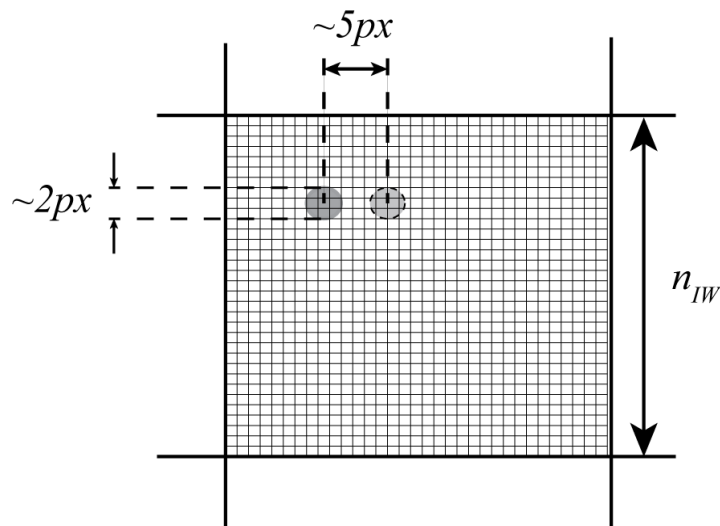


Figure 3.5 – Interrogation Window for vector-analysis with window size, particle pixel size and particle movement indicated.

3.4 Pre-Processing

When a recording has been performed, some pre-processing of the images may be beneficial regarding the accuracy of the PIV-analysis. Such pre-processing may consist of adding a series of filters which removes undesired noise and background intensities, or amplifies low intensity particles, improving the image quality of the images [73]. This may be very useful if the experimental setup has limitations in achieving the optimal design conditions, e.g. problems with poor laser illuminations or high degrees of reflections. Pre-processing presents the ability of dealing with these imperfections digitally. A full overview of the pre-processing tools for the system utilized in this thesis is found in [69], while a brief description of the ones utilized in the measurements will be given in Chapter 5.

3.5 Post-Processing

When the desired flow has been recorded and pre-processed, the post-processing may be initiated. Depending on the recording-parameters, there are several post-processing alternatives. Post-processing generally consists of vector calculation, where the velocity-distribution presents the opportunity of deriving several other flow parameters. This section only presents the post-processing tools utilized in this work, while a full overview of the possible tools for the system used may be found in [67].

Velocity Calculation

The velocity-calculation, or PIV-analysis, is usually performed by cross correlation of either single- or double-framed recordings, with the latter being the most common [66]. The statistical technique of cross correlation may in many cases be considered as the mathematical cornerstone of PIV data evaluation. The technique compares the new and previous locations of all the particles in the IW from frame one to two and defines an intensity field of particle movement. By performing an intensity peak-search the intensity peak which defines the most likely displacement of the particle ensemble can be found. The displacement and corresponding velocity is presented as one local velocity vector for the entire IW, as shown in figure 3.6.

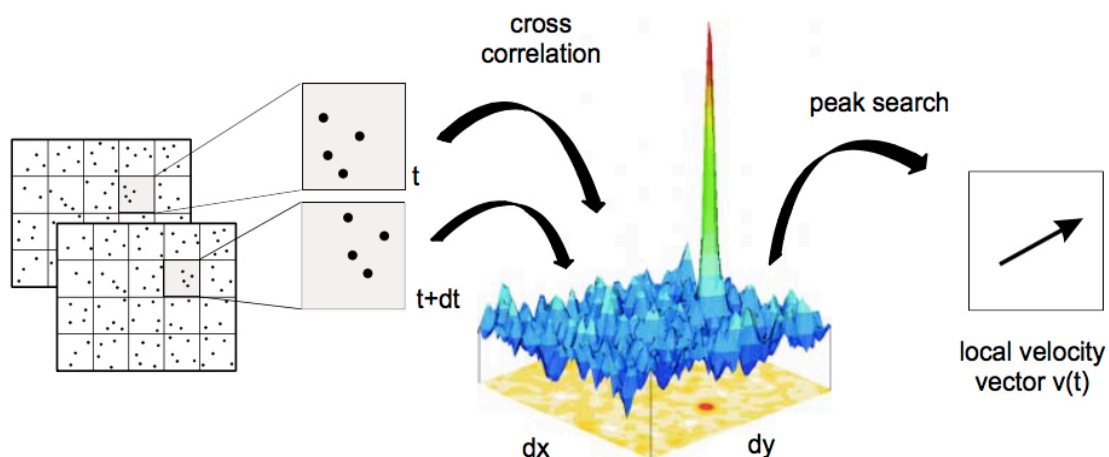


Figure 3.6 – Cross correlation of a double framed image using cross correlation. Adapted from [73].

The above-mentioned approach is repeated for all IWs to give a full velocity field. There are numerous techniques that may be implemented in the cross-correlation to improve its accuracy e.g. multiple-passes and overlap of IWs. The mathematical details of the cross-correlation technique and the possible settings will not be covered here, but may be found in literature[66]–[68].

Vorticity and Swirling-Strength

From the obtained velocity field the vorticity between neighboring velocity vectors in a certain region may be calculated using based on the velocity tensor [67]. This may further be used to calculate the swirling strength for this region, i.e. the degree of rotational motion [73, 75]. Previous PIV studies have found swirling strength superior to other methods by means of identifying certain phenomena e.g. vortices and vortex shedding, in agreement with the general discussion of vortex detection presented in section 2.2 [22], [76]–[79].

Spectral-Analysis

For PIV-analysis, spectral analysis is usually performed using a form of the Fourier transform, e.g. a fast Fourier transform (FFT) or a discrete Fourier transform (DFT), [80], [81]. The power spectrum may be obtained through such an analysis of the velocity development over time at a specific point, along a line or as an average over a larger area [79], [81].

Chapter 4

Investigations of FSI at the Waterpower Laboratory

Both the OHF and Francis turbine of interest in this study have already been studied through experiments and simulations in the Waterpower Laboratory at NTNU. This chapter will present an overview of this work and corresponding results, separated into that regarding the hydrofoil and that of the Francis-turbine. This will serve as a comparative basis for the experimental data to be acquired through the work in this thesis. A general description of the specific designs will be presented, while a full description of the design, experimental setups and flow parameters will be given in Chapter 5 as the same setups will be utilized in the work of this thesis.

4.1 Hydrofoil Investigations

As part of gaining knowledge of the FSI in turbine runner blades, a simple hydrofoil resembling a high head Francis turbine runner blade has been designed in the Waterpower Laboratory. This hydrofoil has been studied experimentally in a blade cascade rig to map the frequencies of vortex shedding and structural vibration, and to evaluate the degree of FSI occurring. Additional investigations using CFD has also been performed, where the effect of modifying the TE of the OHF to mitigate the effects of vortex shedding has been investigated.

4.1.1 Experimental Investigations of FSI

The experimental measurements were performed by Ting[38] and Bergan et.al[82] during fall 2016 using a blade cascade test section in the Waterpower Laboratory. LDV and pressure measurements were performed at incremental steps from 0 m/s to 20 m/s to map the frequencies of foil vibration and vortex shedding, respectively. To avoid cavitation, these measurements were performed with the system pressurized at approximately 7 bar . In addition, piezoelectric patches were used for external excitation of the foil to provoke foil vibration. Lock-in behavior was found to occur for velocities in the range $10\text{ m/s} - 12\text{ m/s}$ as shown in figure 4.1, with peak vibrational amplitude occurring at 11 m/s at a frequency of 631 Hz using external excitation. In the vicinity of lock-in, the vibrational frequency of the foil was found to increase from approximately 626 Hz to 640 Hz , using external excitation to provoke vibration. The vortex shedding frequencies were not successfully acquired as the measured frequencies from the pressure measurements were found to actually be the foil vibrational frequency due to an inadequate positioning of the pressure sensor [38]. This accentuates the need of further experimental work for determination of the vortex shedding characteristics, to be discussed in the next chapter.

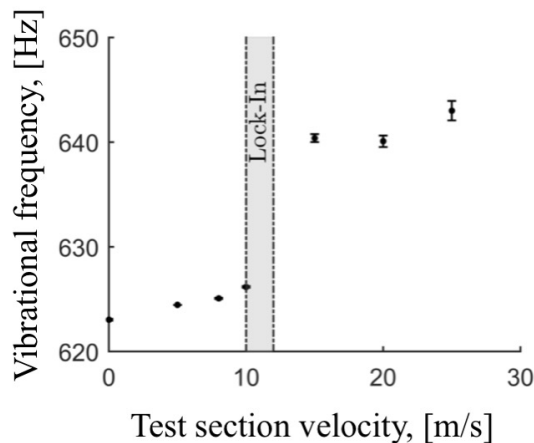


Figure 4.1 – Measured foil vibrational frequency vs test section velocity using external excitation. Adapted from [82].

4.1.2 Simulations of Vortex Shedding from Trailing Edges

Through numerical investigations, Heggebo[83][84] has studied the possibility of mitigating the effects of vortex shedding and reducing the risk of lock-in by means of modifying the TE of the hydrofoil studied by Ting and Bergan et.al. Using the velocity of 11 m/s as reference velocity, the entire three-dimensional flow past the hydrofoil has been simulated for a range of TEs. Mitigation of TKE in the downstream region was achieved by adding a sinusoidal-serrated pattern to the TE, partly based on the optimization procedure of serration design by Nedic and Vassilicos [54]. The design was also found to reduce the vortex shedding frequency significantly, without having a significant impact on the foil's natural frequency. As discussed in section 2.4.1, this presents a shift in lock-in velocity range.

Figure 4.2 shows the OHF design, while the MHF design is presented in figure 4.3. On the latter, six troughs have been added along the TE, giving five full protrusions as shown. The sharp serrated design has been smothered by the rounded sinusoidal geometry primarily to avoid the risk of cavitation at the edges.

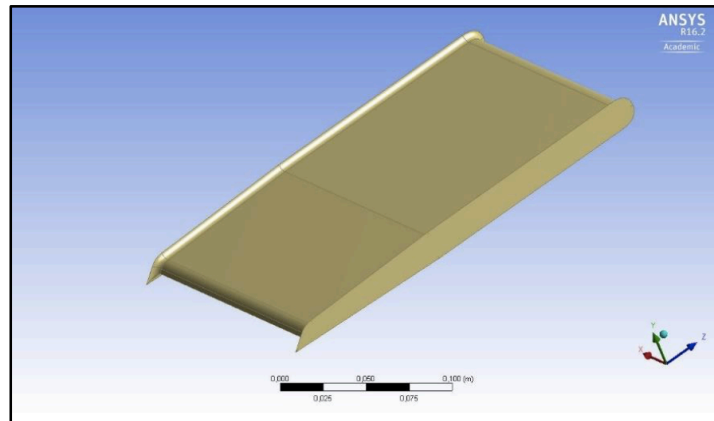


Figure 4.2 - Original hydrofoil design used in simulations performed by Heggebø [83].

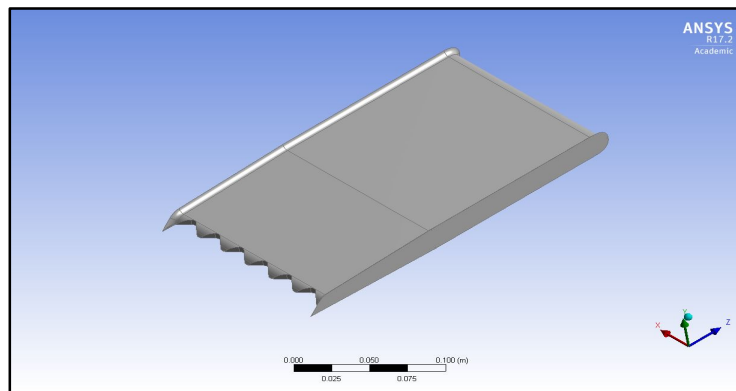


Figure 4.3 - Modified hydrofoil design with six troughs, used in simulations performed by Heggebø [83].

Heggebø's simulations were performed in three steps. First, a CFD analysis of the flow surrounding the hydrofoils was simulated using ANSYS CFX. A one-way FSI was then performed by coupling the CFD-results to ANSYS Static Structural to investigate the flow's effect on the hydrofoil structure. Structural deflections were assumed to be small, preventing the need of iteration between the structural analysis and CFD simulations, i.e. a two way FSI. Finally, a separate simulation using ANSYS Modal was performed to determine the natural frequencies of the foils for comparison with the shedding frequencies, with the results presented in table 4.1. The first mode natural frequency was found to increase by approximately 3 % for the MHF as a consequence of the modification.

Table 4.1 – Natural frequencies of the hydrofoils.

<i>Hydrofoil</i>	<i>First mode natural frequency [Hz]</i>
OHF	677.2
MHF	697.3

Due to the three-dimensionality of the MHF, all simulations were performed as three-dimensional, using the mesh shown in figure 4.4. The elliptical area downstream the TE of the hydrofoil consists of a finer mesh, i.e. a higher number of nodes, and defines the downstream region where experimental comparisons are to be made. It is within this fine mesh area the vortices may be properly described by simulations.

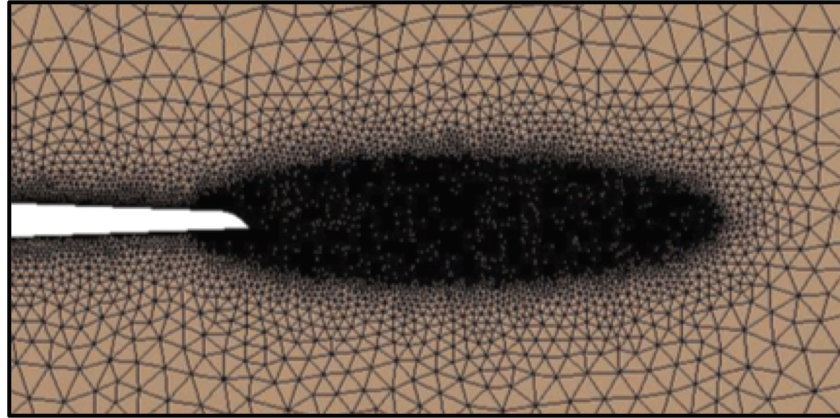


Figure 4.4 – Mesh utilized in the simulations by Heggebø. The fine-mesh (black area) stretches approximately 70mm downstream the TE, with a width of approximately 20mm. Adapted from [84].

A spectral analysis of the simulated pressure data was performed for both hydrofoils to map the vortex shedding frequency distribution, with the results shown in figure 4.5. The analysis was performed at the spanwise center at a point just downstream the TE. The vortex shedding frequency of approximately 530 Hz of the OHF was evaluated as relatively close to the first mode natural frequency and thereby presenting the risk of lock-in.

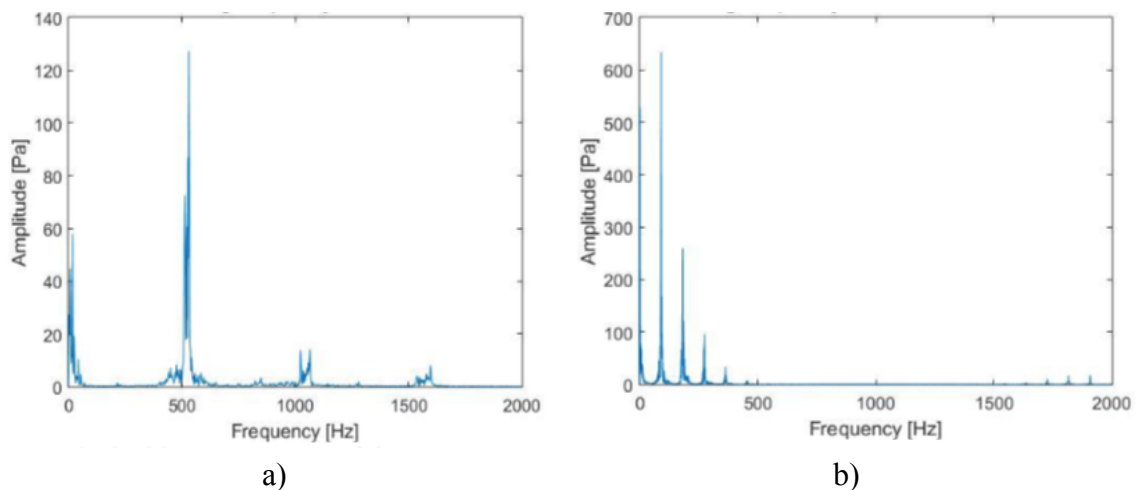


Figure 4.5 – Shedding frequencies of OHF (a) and MHF with six serrations (b) at the spanwise centre of the foil. Adapted from [84].

For the MHF, the dominating vortex shedding frequency was reduced to approximately 100 Hz, or by approximately 80 % compared to the OHF. This significant reduction suggests the adding of serrations to be an effective approach in reducing the risk of lock-in and thereby mitigating the potential of structural failure due to FSI. However, the vortices observed in the downstream region of the MHF induced pressure pulsations of higher amplitude than those of

the OHF. From the TKE analysis, the vortex strength of the von Karman vortices of the MHF were found to decrease in strength, but from a vortex core analysis the dominating vortices shed from the MHF were observed to be of so-called *horseshoe*-type. Heggebø suggested the increased pressure amplitudes of the MHF to be related to the occurrence of such stronger horseshoe vortices.

4.1.3 Summary and Discussion of Results

The experimental, empirical and simulated data for vortex shedding- and natural frequency may be summarized as shown in table 4.2.

Table 4.2 – Empirical, experimental and simulated values for first mode natural- and vortex shedding frequencies at 11m/s.

Type	Frequency	OHF [Hz]	MHF [Hz]
<i>Empirical</i>	<i>Vortex Shedding</i>	541	-
<i>Experimental</i>	<i>Natural</i>	631 ¹	-
	<i>Vortex Shedding</i>	-	-
<i>Simulated</i>	<i>Natural</i>	677	697
	<i>Vortex Shedding</i>	530	~100

The empirical value was determined using (2.10) but as this is only developed for two-dimensional TE geometries, no estimation was performed for the MHF. Some difference exists in the simulated and measured vortex shedding frequencies which Heggebø believed to be related to the simplification of a one-way FSI which do not capture the foil's vibrational impact on the vortex shedding. She also suggested the simplified structure utilized in the simulations as another possible explanation to the difference between measured and simulated natural frequency. In the simulations, both the hydrofoil and its casing were considered as one solid object, consisting of the same material with no imperfections. This is not the case for the real rig, where the casing and hydrofoil is made of stainless steel and aluminum, respectively, containing pressure taps, bolts and slots for strain gages to be discussed later. Such differences may affect the material properties, and thereby also the natural frequencies.

As is evident from the presented results, the experiment does not give sufficient data for determining the vortex shedding frequency, and a comparison with the simulated results may thereby not be performed for validation. For a reliable comparison, three-dimensional experimental data in the spanwise direction of the hydrofoil is required. Performing PIV measurements in this region will provide such data and give an impression of the three-dimensionality of the flow and a more complete vision of its behavior and frequencies.

¹ Determined using external excitation.

4.2 Francis turbine

In the need of further knowledge of RSI and FSI occurring in Francis turbines, several investigations have been performed on a scaled model turbine in the Waterpower Laboratory, both numerically and experimentally. The model turbine is a scaled model turbine of one of four Francis turbines in operation in Tokke powerplant, Norway. Numerical simulations of the flow from turbine inlet to draft tube outlet has been performed at several turbine operating conditions, including transient operations [61], [85], [86]. Experimental data from measurements e.g. pressure measurements along the lower cover in the vaneless space and in the draft tube have previously been acquired [87]. However, none of the previous experimental measurements provide data which may be directly compared to the measurements to be performed in this thesis, i.e. velocity measurements in the vaneless space. This section will therefore be devoted to the relevant numerical investigations covering the vaneless space region. A brief overview of the key results and parameters that may be utilized in preparing the experimental measurements to be performed will be presented

4.2.1 Flow Simulation in the Vaneless Space

Trivedi [61], [85], has performed numerous simulations of the flow in the vaneless space of the Francis-turbine to be investigated. Variations in both flows and operating conditions have been investigated numerically using ANSYS, with primary focus on the RSI and pressure pulsations occurring in the turbine. A detailed description of his results will not be given in this thesis, but a brief overview of some key results will be presented as they may serve as a useful tool in preparing the PIV measurements to be carried out on the Francis-model. For the scope of this thesis, the simulated values of the velocity field is of primary interest as this may be directly utilized to estimate PIV system settings. They may also serve as a basis for comparisons to the experimentally obtained velocity field.

The flow conditions during high load are of particular interest as this is the operating condition with the highest flow rate and flow velocities occurring in the turbine. Higher velocities may limit the ability of the PIV system to capture and describe the velocity field, and the high load operating condition therefore represents the “worst case” scenario for the PIV system.

Figure 4.6 shows the mesh used in the simulations by Trivedi. Compared to the mesh utilized by Heggebø, this is much larger, with fewer cells located at the TEs of the vanes, and the corresponding simulations may therefore not give a similar resolution of the vortices. If this mesh is fine enough for reliable comparisons of vortex streets and vortex strengths with the experimental PIV measurements remains to be investigated through experimental work.

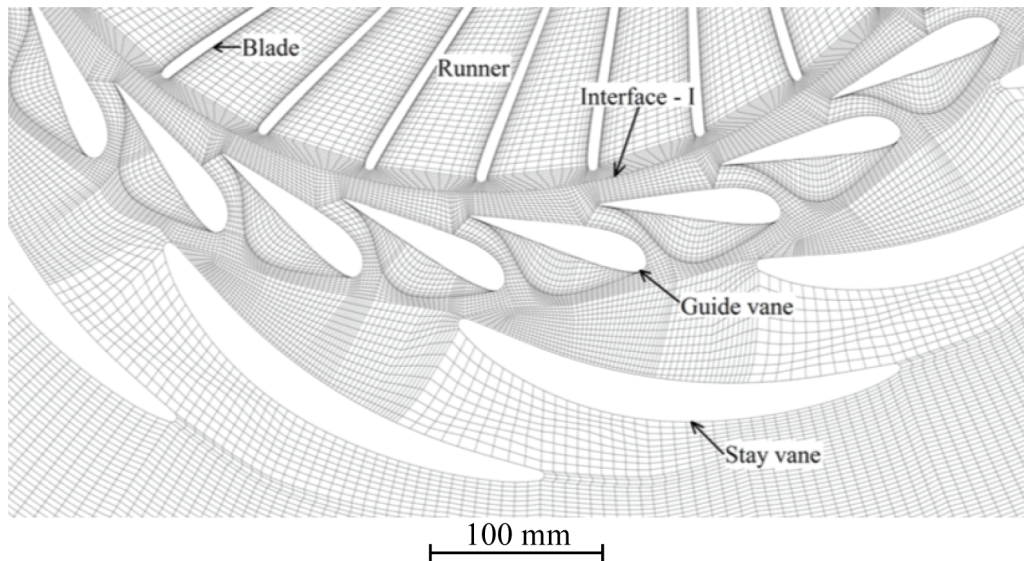


Figure 4.6 – Hexahedral mesh utilized in Trivedi's simulations. Adapted from [85].

At high load, the turbine is operated at a volumetric flow of $0.23 \text{ m}^3/\text{s}$, runner speed of 380.4 rpm and a net head of 12.61 m . Figure 4.7 presents the simulated high resolved velocity field at BEP ($0.21 \text{ m}^3/\text{s}$, 344.4 rpm , 12.77 m) (a), and the less resolved velocity field at high load (b). The simulated velocity field for BEP show a distinct wake at the TEs of both SVs and GVs. At BEP, velocities up to approximately 12 m/s are achieved, while at high load, peak velocities up to 15 m/s occur in the vaneless space [88].

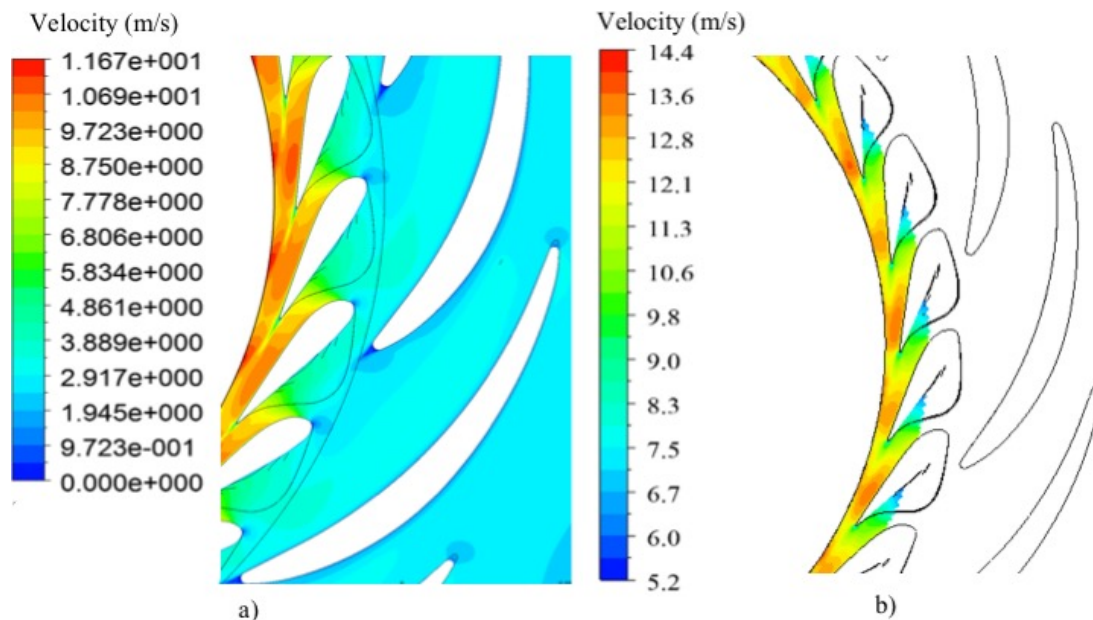


Figure 4.7 – Velocity plot for the Francis-model at BEP. Adapted and modified from [89].

For further details regarding the operating conditions and the specific simulations, the reader is referred to the overview presented by Trivedi [87][86].

Chapter 5

Experimental Procedure and Setup

As part of the main objective of this thesis, the following is to be determined:

- The velocity distribution and vortex shedding characteristics downstream two hydrofoils, and its relation to FSI at velocities in- and around lock-in.
- The velocity distribution in the vaneless space of a Francis turbine for different operating conditions.

PIV is the method of choice for achieving these intermediate objectives. All measurements are to be carried out in the Waterpower Laboratory at NTNU. The hydrofoils are to be mounted in the blade cascade section utilized by Ting and Bergan, and the previously mentioned Francis model is to be utilized for vaneless space measurements.

This chapter gives a brief presentation of the hydraulic system in the laboratory and the experimental equipment utilized, followed by a description of the specific designs, experimental setups and methods used for data analysis for the two experiments. It is to be noted that the experimental measurements on the MHF were not performed due to time-constraints, and measurements on the Francis turbine could not be performed due to technical issues with the turbine setup itself. The experimental setups and methodology of these is therefore to be considered as a guide or suggestion for the measurements to be performed in future work.

5.1 Hydraulic System

The system shown in figure 5.1 will be utilized for both the hydrofoil and Francis-turbine measurements. The hydrofoils are mounted in the blade cascade test-section located as indicated in the figure. Water is flowing through the main loop and further through either the Francis-loop or blade-cascade loop, depending on which case that is to be investigated. In both cases the water is circulated by one or two centrifugal pumps depending on the required flowrate, with the capacity of delivering a flowrate of $0.5 \text{ m}^3/\text{s}$ and a head of 100 m in total. The pipe-lines consist of both $\text{Ø}600 \text{ mm}$ and $\text{Ø}300 \text{ mm}$ pipes with lengths according to the scale in the figure.

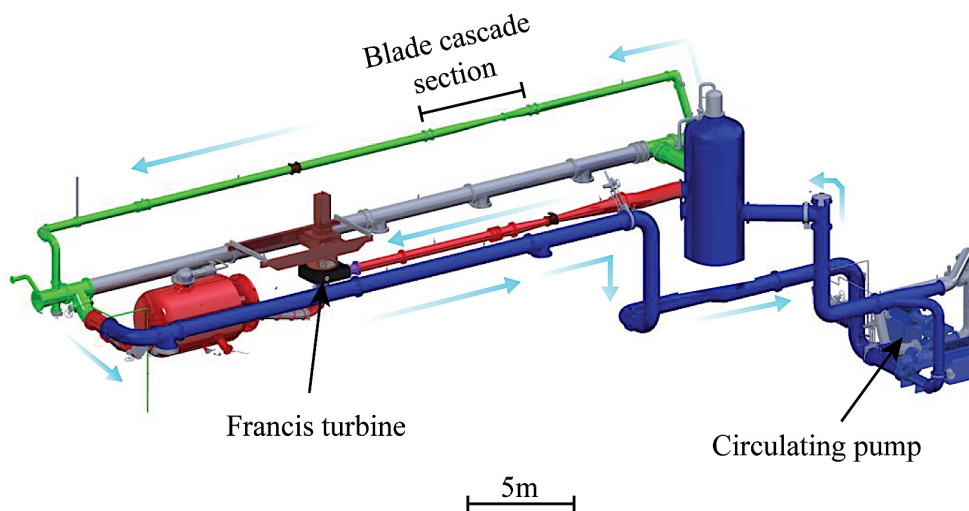


Figure 5.1 – Closed-loop hydraulic system in the waterpower laboratory. Water circulates through the main loop (blue) and further through either the Francis-loop (red) or blade cascade-loop (green). Both loops are driven by the same circulating pump.

5.2 PIV Analysis and Equipment

Both the blade cascade setup and the Francis turbine are studied using the same PIV system and software in the laboratory, with an overview of the equipment used given in table 5.1. A high-speed Complementary Metal-Oxide Semiconductor (CMOS) camera is used for image recording of the AOI which is illuminated by a double cavity Neodymium-doped yttrium lithium fluoride (Nd:YLF) laser. The laser head emits the laser-light generated by the laser's power unit. The power unit and the high-speed camera is connected through a programmable timing unit (PTU), which is further connected to and controlled by the system computer and software. The PTU provides a synchronous triggering of the camera and laser, and sets the rate and duration of the signals according to the parameters set in the system's software. A laser timing stabilizer (LTS) connected to the PTU synchronizes the laser's actual emission pulses with the input triggering pulses through an optical feedback loop from the laser's head. The system settings are controlled using the software Davis 8.4 and CW Diode client PIV 1.0.

Use of such high-power lasers present a risk of eye-injuries, and a thorough risk-assessment is to be conducted prior to measurements. The equipment is also of high value, and the potential risk of equipment damage should also be included in the assessment.

Table 5.1 – PIV Equipment Used

Camera:	FastCam Mini UX100
Lens:	Tokina AT-X Pro 100mm, 2.8
Synchronization unit:	LaVision PTU X
Timing stabilizer:	LaVision LTS
Laser:	Litron LDY 300 PIV
Seeding particles:	Potters, Spherichel 10 – 20 μm
Software:	Davis v.8.4 and CW Diode client PIV v.1.0

Figure 5.2 presents the general iterative procedure performed in the PIV process. Image settings, i.e. settings regarding size of FOV and evaluation of IW size, laser intensity, laser sheet focus, camera focus, seeding particle density and size, are adjusted according to the design rules presented in section 3.2. Adjustments of dt , frequency and synchronization during image acquisition is performed according to the recommendations set by (3.1). Depending on the quality of the recorded images, the images are more or less pre-processed through a non-linear filter and a time-series filter to remove undesired reflections and reduce the effect of particle agglomerations. The PIV- and post-processing is performed through cross-correlation of double frames, with a resolution depending on the IW-settings. Evaluations regarding accuracy, quality, uncertainty and conformity with expected results of the measurements are thereby performed. If the processed results show lack of accuracy and room for optimizations, the process is adjusted and repeated until sufficient measurements are obtained. If the obtained velocity field are evaluated as reliable, the swirling strength is calculated, followed by a discrete-time Fourier Transform (DTFT) analysis of the velocity field.

The specific settings, parameters and methods of processing for the two experimental setups will be described in their corresponding sections.

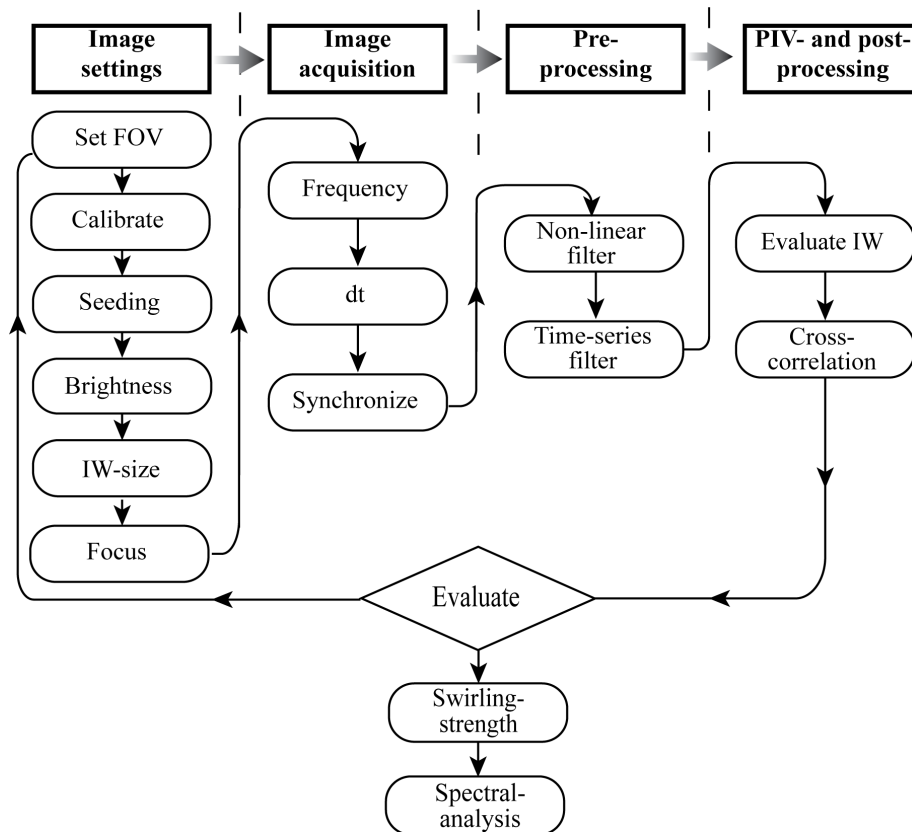


Figure 5.2 – PIV procedure for the experimental setups.

5.3 Blade Cascade

This section presents the blade cascade in which the hydrofoils are mounted, the experimental setup and the measurement techniques utilized in the hydrofoil investigations. Measurements were performed on the OHF, but unfortunately, time did not allow for measurements to be carried out on the MHF. However, the requirements of the measurements to be performed on the MHF will be described based on the design suggested by Heggebø.

5.3.1 Test Unit Description

The existing blade cascade setup consists of a section of pipes and a test unit, initially designed to be utilized in pressure- and vibration measurements on a hydrofoil as part of the HiFrancis project at NTNU [90]. This test unit has been modified in previous work by the author to be suitable for PIV measurements [3]. As seen in figure 5.3, the unit is a relatively complicated structure.

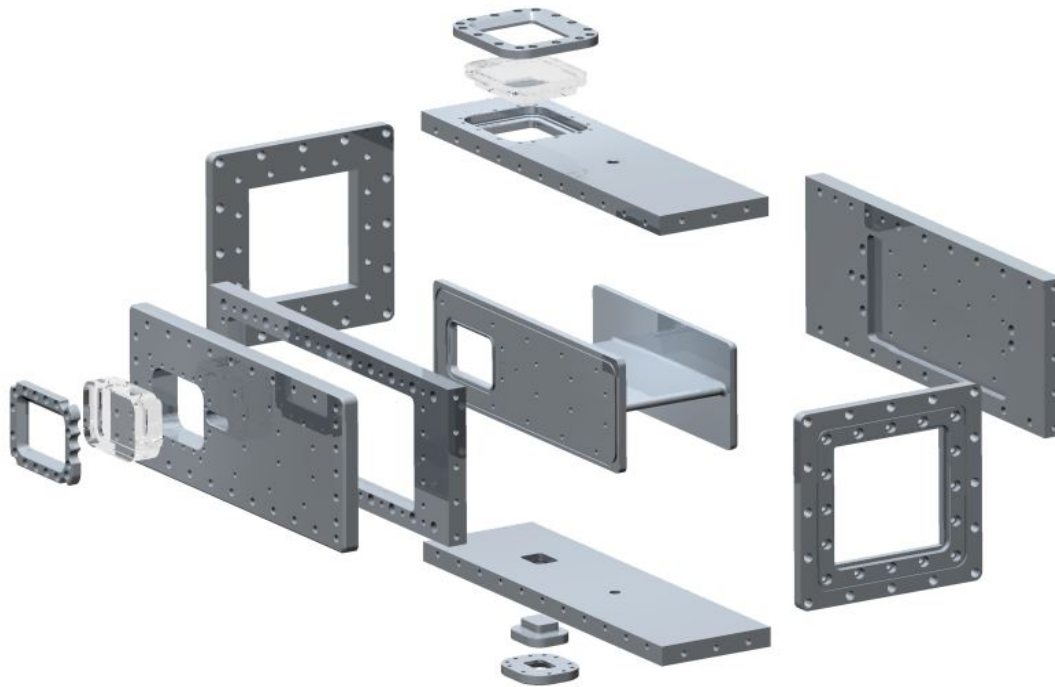


Figure 5.3 – Exploded view of main parts of the test section. Notice that the hydrofoil and its sidewalls are a unified unit. Adapted from [91].

The test unit is a square $150\text{ mm} \times 150\text{ mm}$ pipe section made of 25 mm thick walls of stainless steel, partly welded, to ensure no deformation or vibration of the structure when the system is pressurized. It consists of an inlet and outlet, a back wall with pressure taps, a top wall with window, a front wall with window, an outer lid, a bottom wall with window and an interchangeable hydrofoil in aluminium. The front wall is only attached by bolts which makes it possible to replace the hydrofoil to be studied with one of a modified geometry. The hydrofoil and its associated sidewalls are manufactured as one unit, permitting foil interchangeability as long as the side walls of the hydrofoils fits the side walls of the casing. The bottom wall has a small plexiglas window allowing for vibrational measurements of the foil using laser doppler vibrometry (LDV). The top window is of length and width $100\text{ mm} \times 85\text{ mm}$ respectively, allowing for laser illumination, while the corresponding measurements for the side window is $90\text{ mm} \times 61\text{ mm}$ which gives optical access for the camera. Combined, these windows give optical and laser sheet access allowing for PIV investigations of an area of approximately $100\text{ mm} \times 70\text{ mm}$ just downstream of the TE, covering the fine-mesh area of the simulations by Heggebø. The entire interior of the test unit, including the hydrofoil, is painted black to reduce the risk of disturbing reflections and uncertainty during PIV measurements.

Figure 5.4 shows the location of the pressure sensors, strain gage and piezoelectric patch utilized in the FSI studies by Ting and Bergan. For the scope of this thesis, only the strain gage will be utilized.

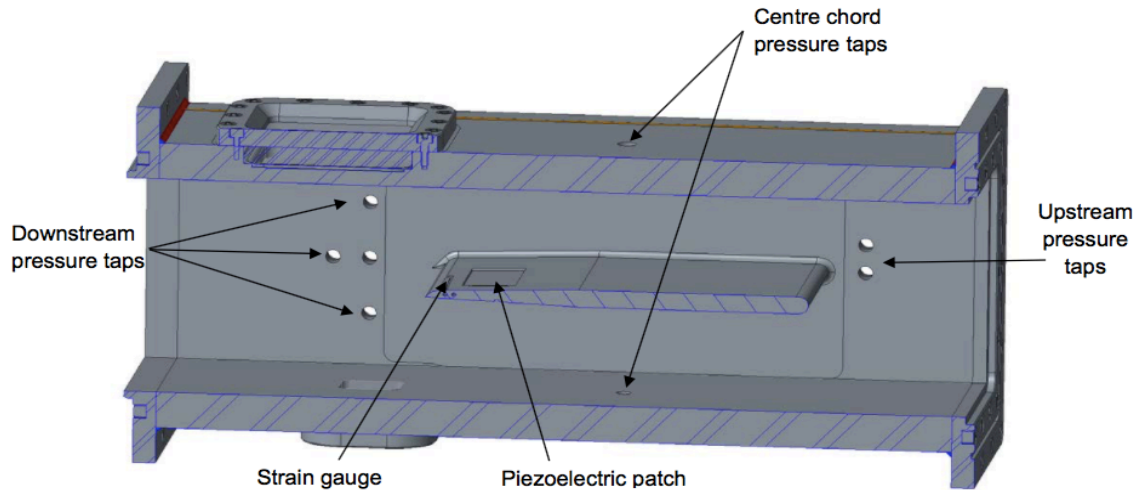


Figure 5.4 – Flow wise cross section of test section of blade cascade, with pressure taps, piezoelectric path and strain gage. Adapted from [91].

The test unit is mounted between two square $150\text{ mm} \times 150\text{ mm}$ pipes connected to a $\text{Ø}300\text{ mm}$ pipe through an upstream contractor and a downstream diffuser. Water flows through the test section and further through the closed loop system already described.

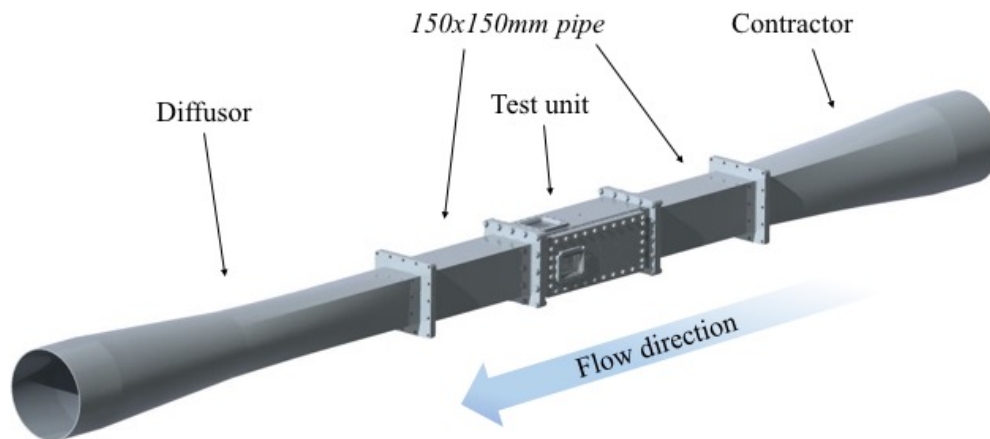


Figure 5.5 – Blade cascade test section.

5.3.2 Original Hydrofoil

The OHF is 12 mm thick with a characteristic length of 250 mm and a width of 150 mm . The upper and lower side, i.e. the suction and pressure side respectively, are symmetrically designed to avoid any lift-force being generated. 150 mm downstream the leading edge, the thickness starts tapering down to a TE thickness of $t = 4.5\text{ mm}$ before it is chamfered and rounded. This design gives a TE similar to that of a typical Francis turbine runner blade, and the geometry factor of $B = 131$ may be utilized in (2.10). When mounted in the experimental setup, the hydrofoil is fixed with an angle of attack of 0° . The lift and corresponding vibration of the foil may therefore to a larger extent be assumed to be generated solely by vortex

shedding at the TE. A chord wise cross section of the foil is shown in figure 5.6, while a 3D view is already presented in figure 4.2.

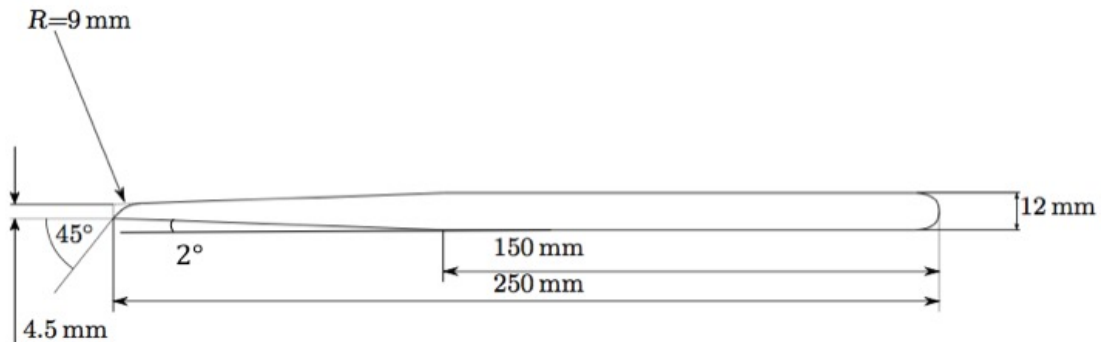


Figure 5.6 – Original hydrofoil design with dimensions. Adapted and modified from [82].

5.3.3 Modified Hydrofoil

The MHF has the same geometry as the OHF, except at the TE where the sinusoidal-serrated edges has been added. Figure 5.7 shows the TE design, with six troughs and five peaks added. The resulting radius from the sinusoidal pattern, length between serrations and length of sides are defined and tabulated in the figure and table 5.2, respectively.

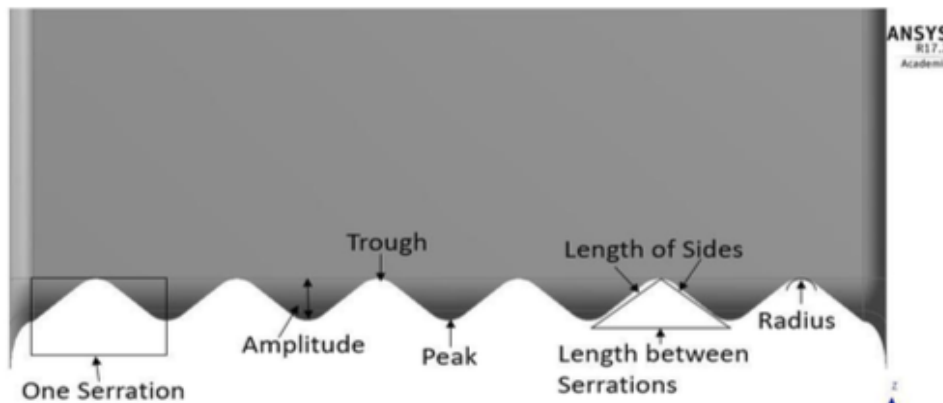


Figure 5.7 – Modified hydrofoil trailing edge geometry. The trailing edge nomenclature is indicated as shown. Adapted from [84].

Table 5.2 – MHF TE design properties

Length between serrations:	0.0241m
Length of sides:	0.0160m
Radius:	0.0040m

5.3.4 Experimental Setup

The experimental setup is shown in figure 5.8. Water circulates through the blade cascade-loop system described in this chapter's introduction, where the test section is positioned close to the middle of a straight, 28 m long $\text{\O}300\text{ mm}$ pipe. To avoid the need of saturating the entire water volume of seeding particles, a feeding pump was located upstream of the test section which injected seeding particles approximately 8 m upstream the test unit. The pump fed a mixture of water and seeding particles from a seeding storage tank when PIV recordings were made. The pipe bend and distance from the test unit was assumed to ensure a homogenous mixing of the seeding particles with the unmixed water. Laser light was emitted from the laser head, through a guide arm and finally through a lens positioned above the top window which distributed the light as a thin laser sheet. The high speed camera was positioned with its FOV in the downstream region of the TE, with a perpendicular view to the laser sheet.

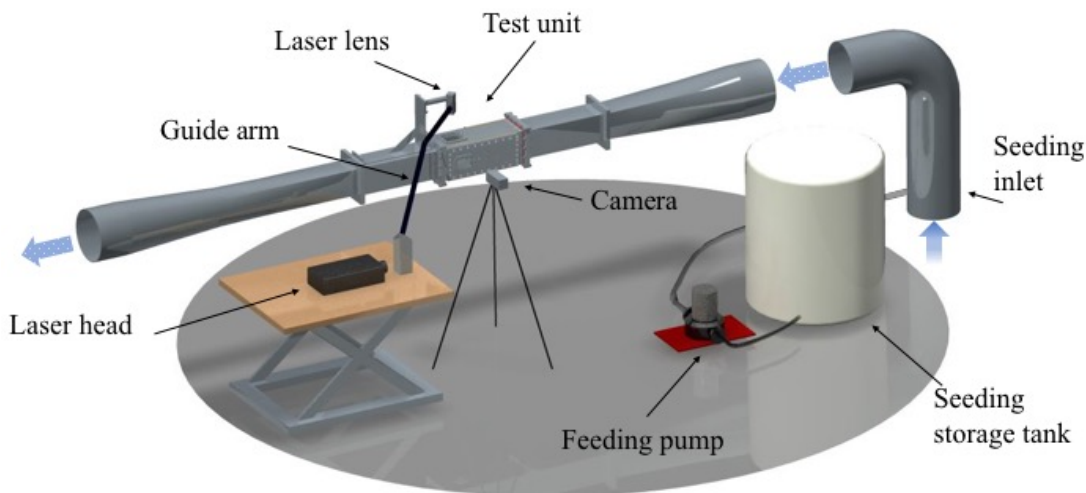


Figure 5.8 – Experimental setup for blade cascade.

An ABB FSM400 electromagnetic flowmeter positioned in the 300 mm pipe approximately 15 m downstream of the test unit was used to determine the average velocity through the test unit. The vibration of the foil was measured using semiconductor strain gages from Kulite. A logging computer connected to the flowmeter, strain gage and PIV system logged the data from these three systems using LabVIEW for a set measuring period.

To avoid the vortex shedding frequency and the natural frequency of the foil in being affected by cavitation, the system was pressurized to the minimum pressure of approximately 1 bar at the test section inlet to avoid cavitation in the test section. This was kept at a minimum as the feeding pump was not capable of injecting seeding particles at high pressure.

The objective of the measurements was to determine if the difference between the natural frequency and vortex shedding frequency could be increased, and to serve as experimental data for the simulations by Heggebø. The majority of the measurements were therefore performed at approximately the same velocity as in the simulations and as where the foil has been found to have its largest vibrational amplitude, i.e. close to 11 m/s in the test section.

5.3.5 Flow and Strain Analysis

The logging computer logged the output signals from the strain gage, flowmeter and PIV system, all at a sampling rate of 10 000 *Hz* for 60 seconds. The PIV signal was only a voltage-signal from the PIV system indicating the exact time-period of when the PIV image acquisitions were made. The logged data was converted to a MATLAB compatible format, before being processed and analysed further using MATLAB. The volumetric flow and test section velocity was found based on the test unit area and the average of the measured flow for the PIV measuring period, while the power spectrum for foil vibration was obtained through a FFT of the measured strain signal for the same period. For details regarding the MATLAB-analysis the reader is referred to appendix A.

5.3.6 PIV Measurements and Analysis

Measurements on the OHF were performed at the same spanwise positions as in Heggebo's simulations. For the OHF, this corresponded to the spanwise center, i.e. at a distance of 75 *mm* from the back wall. One measurement was also performed at a 10 *mm* offset, i.e. at a distance of 85 *mm* from the back wall to study the spanwise location-dependency of the vortex shedding frequency. For the MHF, measurements are to be performed at the spanwise center peak and in its neighboring trough, for direct comparison with Heggebo's simulations, which corresponds to a distance of 75 *mm* and 87 *mm* from the back wall, respectively.

The camera was positioned with a distance of 95 *mm* and 105 *mm* between lens and window for the measurements in the spanwise centered and offset position of the OHF, respectively. This gave a FOV of approximately 21 *mm*×17 *mm* using a 100 *mm* lens. The downstream location of the FOV started at 45 *mm* downstream of the TE. The FOV was thereby within the fine-mesh area in the simulations shown in figure 4.4, and large enough to capture both the upper and lower vortices of the vortex street. These distances and dimensions should be utilized for the measurements on the MHF as well for a proper comparison. Figure 5.9 shows the actual PIV setup used for the measurements.

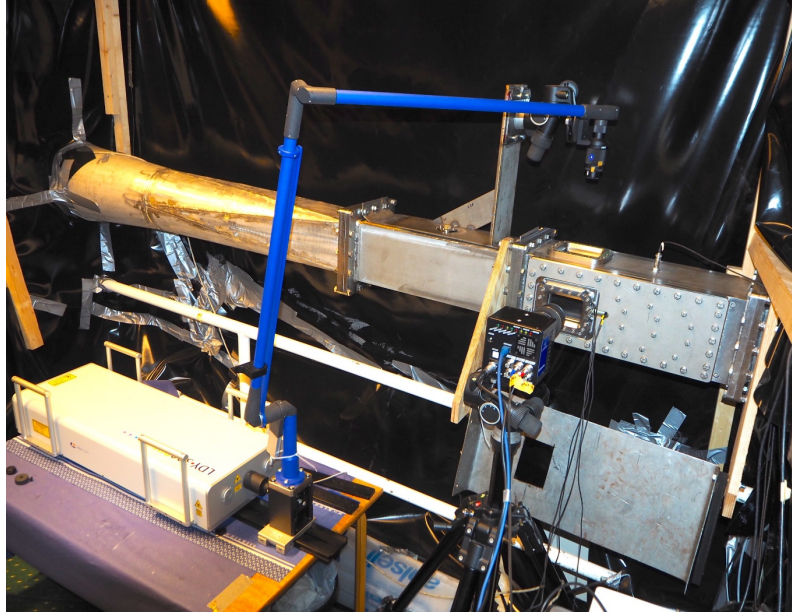


Figure 5.9 – Blade cascade PIV setup.

The measurements themselves were carried out in the following manner; first, the system logging the strain, the flow and PIV measuring-period signal was set to record. After approximately 15 seconds, the seeding pump was set to its maximum feeding of approximately 0.25 l/s for about 7 seconds. Approximately 2 seconds of image acquisition was initiated when the cloud of seeding particles entered the AOI, which occurred after approximately 6 seconds after feeding, at the velocity of 11 m/s in the test section.

Measurements were performed two times at 11.1 m/s , separated by a time gap of 20 minutes. The piping and PIV system thereafter went through a full shutdown and restart, followed by a new measurement at the same settings to verify the repeatability of the experiment. The laser sheet and camera was then moved to the offset position, and a new measurement was performed. This was followed by a partial draining of the system and a new calibration for the offset position, to be discussed further. As time allowed for it, and due to having achieved a high seeding density in the loop-system, a range of velocities were investigated to better map the relation between foil vibration and vortex shedding frequency. These measurements were performed at alternating steps of 0.5 m/s in the range $9.1 \text{ m/s} < U < 13.1 \text{ m/s}$ without external seeding, i.e. only using the remaining seeding particles in the loop system. Table 5.3 presents an overview of the hydraulic system parameters for the measurements performed at 11.1 m/s and in the velocity range. The pressure was slightly increased during these measurements to avoid cavitation at the higher velocities.

Table 5.3 – Hydraulic system parameters for PIV-measurements

Single velocity measurements	Flow rate:	$0.25 \text{ m}^3/\text{s}$
	Test section inlet velocity:	11.1 m/s
	Pressure at inlet:	$\sim 1.1 \text{ bar}$
	$\text{Ø}300$ pipe system velocity	3.5 m/s
Velocity range measurements	Flow rate:	$0.21 \text{ m}^3/\text{s} - 0.30 \text{ m}^3/\text{s}$
	Test section inlet velocity:	$9.1 \text{ m/s} - 13.1 \text{ m/s}$
	Pressure at inlet:	$\sim 2 \text{ bar}$
	$\text{Ø}300$ pipe system velocity:	$2.9 \text{ m/s} - 4.2 \text{ m/s}$
	Velocity increment:	0.5 m/s

Calibration

The PIV setup was calibrated using a calibration device together with a laser-sliding device as shown in figure 5.10, both designed and produced by the author. The device was mounted in the top window frame, and had a dotted plate designed to fulfill the design conditions mentioned in section 3.2 attached to it. The device was positioned such that the dotted plate was parallel to the flow direction, and perpendicular to the camera's view. Two screws on the backside of the device set the mentioned distances from the back wall in the test unit. The system was then calibrated according to the design rules mentioned in section 3.2, using the software's calibration dialog [69]. Further, the laser sheet was aligned to the plane of the dotted plate, ensuring the spanwise location of the PIV measurements to be correct.

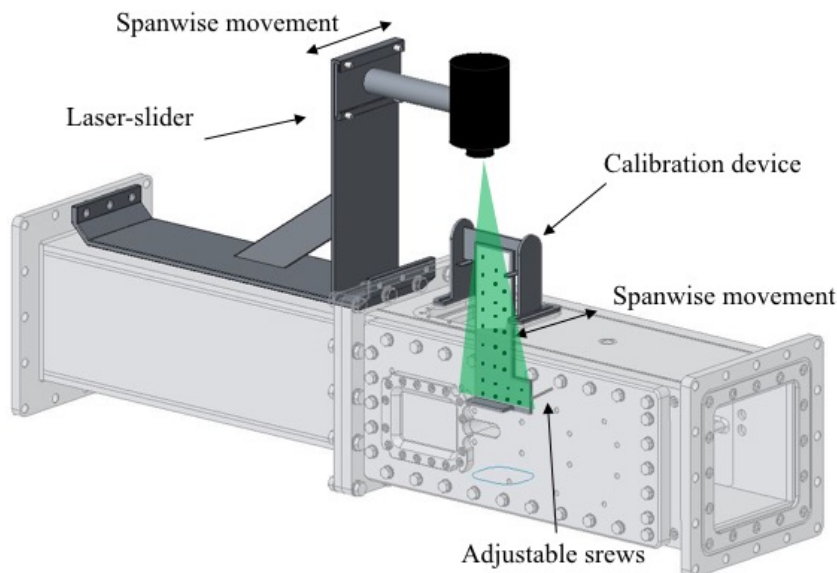


Figure 5.10 – Calibration setup showing the laser slider device, laser sheet, calibration device with dotted plate and the adjustable screws for spanwise positioning.

The system was calibrated prior to measurements for each spanwise position. Each calibration required the entire water level in the system to be lowered to avoid water from exiting through the top window. In addition, the system was recalibrated after completed measurements to assure the camera and laser had not been altered during measurements.

Settings

The camera's image resolution was set to its maximum of 1280×1024 . According to the previously discussed empirical, simulated and experimental data, the expected vortex shedding frequency was in the range $540 \text{ Hz} - 630 \text{ Hz}$ for the OHF, and $f_s \sim 100$ for the MHF. For these frequencies, (2.11) results in a required sampling rate of 1260 Hz and 200 Hz for the OHF and MHF respectively. As the camera allowed for higher frequencies at full resolution, the sampling frequency was set to 2 kHz for increased time resolution. The dt was set to $10 \mu\text{s}$. For each measurement, the maximum of 4367 double framed images was acquired, giving 4367 vector images and 8734 image frames. This resulted in a sampling time of 2.1835 s , which according to (2.12) results in a frequency increment of approximately 0.5 Hz in the power spectrum, regarded as sufficient for the measurements.

The IW size was set to 64 which resulted in a vector resolution of 20×16 vectors. With this IW, FOV size and scaling factor, the resulting spatial resolution was approximately $1 \text{ mm} \times 1 \text{ mm}$.

Processing

The images were pre-processed using a non-linear sliding-minimum filter which enhanced particle contrasts. This was primarily enabled to reduce the image size of large agglomerated particles and other random particles in the system. This was followed by a time series subtraction which removed disturbing background intensities. Figure 5.11 shows the effect of this pre-processing on the raw images.

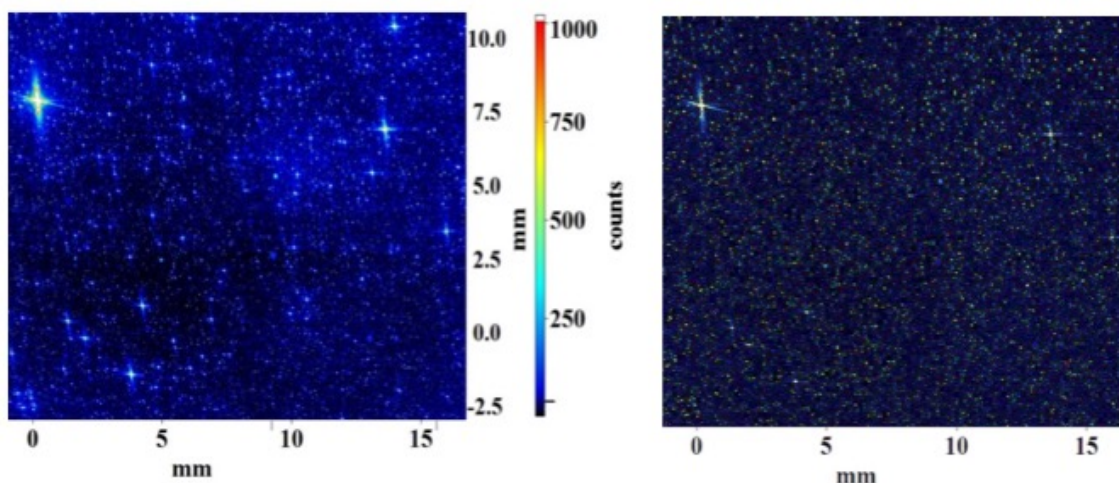


Figure 5.11 – Raw image before and after pre-processing. Notice the large agglomerated particles in the raw-image.

The PIV analysis was performed as a multi-pass cross-correlation with decreasing IW size from 96 to 64, with and overlap of 75 % and 50 %, respectively. Finally, the swirling strength was calculated for a better visual of the vortices followed by a power-spectrum analysis. The power spectrum was obtained through a discrete-time Fourier transform (DTFT)

of the average of vertical velocity fluctuation. Seven neighboring velocity vectors located furthest upstream in the center of the wake were averaged and evaluated as representative for this wake fluctuation. All operations were performed using the system software, but the results were imported and further analysed in MATLAB for comparison with the data logged by the logging computer.

5.4 Francis Turbine

The Francis turbine to be investigated is a scaled 1:5.1 model of the prototype turbine utilized in Tokke powerplant, Norway [92]. The objective is to obtain PIV measurements of the flow in the vaneless space. These measurements will serve as a comparative basis for previous and future numerical analysis e.g. the simulations presented in section 4.2.1, and future pressure measurements inside the turbine runner. As the PIV measurements were not performed, the experimental setup-description is partly a description of that which is already prepared on the setup together with recommendations or suggestions by the author to the final setup. This sections gives a brief description of the turbine unit, the turbine's GVs and the planned experimental setup to be utilized for PIV measurements. A description of the turbine design and previous measurements on the turbine unit may be found in [86], [92].

5.4.1 Unit Description

The Francis turbine is equipped with 14 SVs in the spiral casing, 28 GVs in the wicket gate, a runner with 15 full-length blades and 15 splitters and an elbow type draft tube. At high load the GVs are positioned at an angle of 14° at maximum, giving a flow rate of $0.242 \text{ m}^3/\text{s}$. The runner inlet diameter is 0.625 m , which at the turbine's high load speed of 332.59 rpm results in a runner blade tip velocity of 10.9 m/s .

The turbine has been modified to be suitable for PIV measurements as shown in figure 5.12. A narrow, $32 \text{ mm} \times 580 \text{ mm}$ plexiglas slit in the spiral casing gives access for laser illumination to the inside of the casing. Two SVs and three GVs are manufactured in plexiglas, allowing for laser illumination in the vaneless space, i.e. in the AOI of the turbine. A plexiglas window has been added in the bottom cover of the wicket gate, giving optical access for the high speed camera to the AOI. This has a circumferential length of approximately 260 mm along the centerline and a width of 70 mm , spanning three plexiglas GVs and the runner inlet, as seen in the figure.

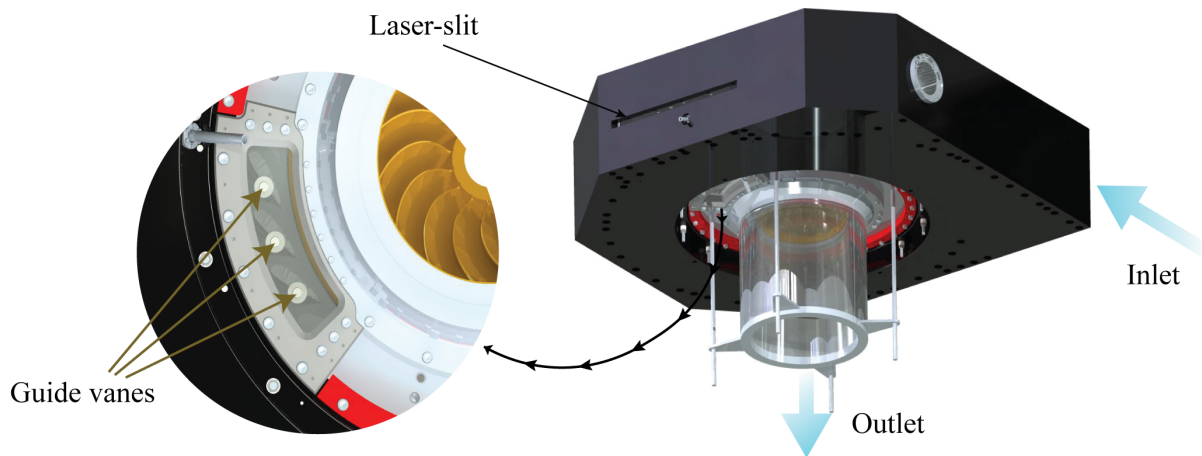


Figure 5.12 – Model turbine showing the laser slit and plexiglas guide vanes. Water flows in through the turbine inlet and out through the runner outlet.

The GVs in the turbine model have a fairly symmetrical shape, as shown in figure 5.13. They measure 21 mm at their thickest, have a characteristic length of 105 mm and a height of 58.6 mm , as shown in the figure. The TE is oblique and rounded, similar to that of the OHF, but with a more narrow TE thickness of 1.18 mm . The curvature in the spanwise direction serves the purpose of reducing the generation of horseshoe vortices in the gap between the top and bottom cover in the wicket gate.

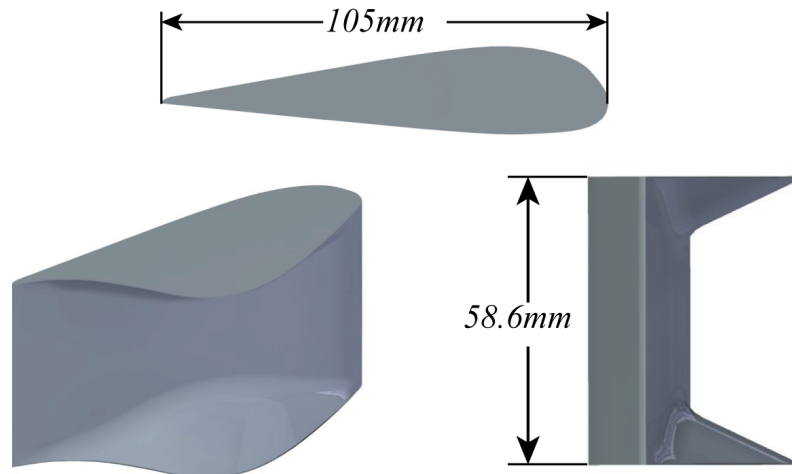


Figure 5.13 – Guide vane geometry in the model turbine. The height and characteristic length is indicated.

5.4.2 Experimental Setup

The experimental setup is to be set up as shown in figure 5.14. Water is now flowing through the Francis-loop, with system parameters summarized in table 5.4, [86]. In a similar manner as with the blade cascade setup, a feeding pump and seeding tank is to be positioned in the upstream region of the turbine. The laser and laser head is located on the side of the turbine, with the guide arm attached to a positioning device for a steady and adjustable configuration. The camera is mounted to a rigid plate attached to the turbine casing's bottom by two threaded rods. The threading on the rods allows for adjustments regarding the camera's distance from the AOI, and a device mounted to the camera itself allows for angular positioning, i.e. aiming of the FOV.

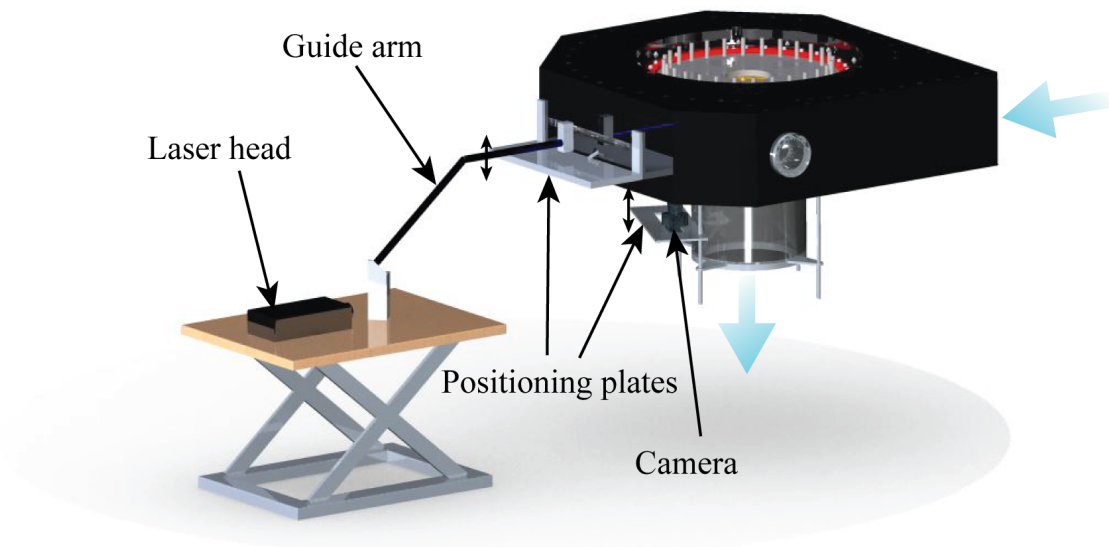


Figure 5.14 – Experimental setup for PIV-measurements on Francis turbine showing camera, laser head, guide arm and the adjustable positioning plates. Notice the indicated direction of possible adjustments of the plates.

A flowmeter is located approximately 9 m upstream the turbine inlet. Pressure sensors are located at incremental steps along an estimated streamline throughout the entire turbine from turbine inlet to outlet, including on the runner itself.

Whether the existing feeding pump is capable of delivering the required seeding flow rate or not at the tabulated system parameters, should be evaluated prior to performing the measurements. If the system is incapable of providing the required seeding flow, the possibility of either pressurizing the seeding tank or position it at a higher floor should be considered.

Table 5.4 – System parameters at high load [86]

Head (m)	11.88
Flow rate (m^3/s)	0.242
Inlet pressure abs. (kPa)	212.4
GV angle ($^\circ$)	12.43
Turbine speed (rpm)	332.59

5.4.3 PIV Measurements

The PIV system is set up as shown in figure 5.14, with a section view presented in figure 5.15. The laser is positioned such that its laser sheet illuminates the entire AOI. The camera should be set such that its FOV covers both the TEs of the GVs and the runner inlet, as this makes it possible to study the entire velocity field for a full runner blade-passing.

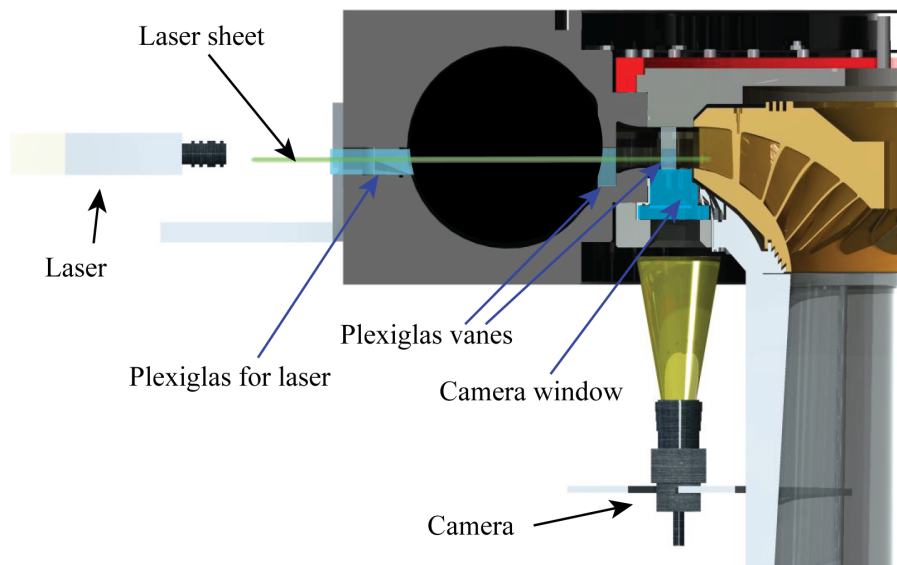


Figure 5.15 – Section-view of the PIV setup for the Francis turbine, indicating the position of laser, laser window, plexiglas vanes, camera and camera window.

Several pressure- and strain measurements are planned to be performed simultaneously as the PIV measurements. A similar synchronization-system as the one utilized for the measurements in the blade cascade, i.e. having a signal-coupling between the PIV system, flowmeter and pressure- and strain logging system, should be developed.

System Settings

A FOV covering the GVs and runner inlet will be significantly larger than the one used for the blade cascade setup. If a similar particle density is achieved in the flow, this will give a

significantly higher image particle density, and the resulting recordings may be analysed using a higher vector resolution, i.e. smaller IWs.

According to the simulations presented in section 4.2.1, velocities up to 15 m/s are expected to occur in the vaneless space. This is in the same order as in the blade cascade, and the system settings utilized for the blade cascade setup may therefore be used as a guide.

The GVs TEs are distanced approximately 70 mm from each other. With the runner blade tip velocity of 10.9 m/s, a blade requires approximately 0.0064 s to perform a full passing. Using the pixel resolution and camera frequency as in the blade cascade, the system would acquire approximately 12 double-framed images for one blade-passing. The system may also be set to a lower pixel resolution to obtain higher frequencies, or alternatively to shoot in single-frame mode for even higher frequencies.

For measurements of the wake and vortex shedding from the GV, the size of the FOV should be approximately 5.5 mm×4.5 mm, scaled according to the ratio between TE size and FOV size used for the hydrofoil measurements. If a similar seeding density as that of the hydrofoil measurements is achieved in the Francis turbine setup, an IW size of 128 will give an IW particle density approximately similar as in the hydrofoil measurements. This will give a vector resolution of 10×8, which is significantly lower than that of the hydrofoil measurements.

Calibration

The system is to be calibrated in a similar manner as for the blade cascade setup. A calibration plate which allows for an exact positioning in the AOI is to be used. The calibration procedure should be performed while the system is filled with water, to ensure no errors regarding differences in refraction angles.

5.5 Uncertainty of Tests

As measurements were only performed on the OHF, uncertainties related to the Francis-setup and MHF are not considered here. This section gives only a brief discussion of the uncertainties regarded as most significant for the performed measurements. The analysis is based primarily on the definitions given in IEC 60193 [93] and in section 2.8.

5.5.1 Uncertainty in Test Section Velocity

The test section velocity was determined based on the flow rate measured by the flowmeter and the area of the test section.

Uncertainty in Flow Rate

Uncertainties related to systematic and random errors in the calibration errors is based on the calibration performed by Ting [38], the work by Solemslie [94] and the calculations by Storli [95]. The random uncertainties in the flow measurements themselves are found through use of (2.13) - (2.15). The total uncertainty is then found using (2.16) and (2.17). Flow measurements were performed only once for each velocity in the velocity range, and the uncertainty is therefore related to the uncertainty in the sample mean. The maximum values are presented in table 5.5.

Table 5.5 – Uncertainty in flow rate

Uncertainty	Description	Value
$P_{Q,cal}$	<i>Systematic uncertainty in the calibration</i>	$\pm 0.125\%$ [38]
$P_{Q,rand}$	<i>Random error in the sample</i>	$\pm 0.002\%$
$w_{Q,tot}$	<i>Total uncertainty in sample</i>	$\pm 0.125\%$

The calibration data was adapted from the calibration performed by Ting, and is regarded sufficient for the required accuracy of the performed experiments.

Uncertainty in Test Section Area

The test unit is made of machined parts, and the uncertainties related to the area is expected to be small. However, the test unit has been partly welded, and a certain degree of deformation is likely to have occurred. An accurate mapping of the test section area and the specific error has not been performed, but for the scope of this thesis, an error of $e_b = \pm 0.5\text{ mm}$ in the side lengths b forming the test section area is used as an estimation.

Uncertainty in Test Section Velocity

The test section velocity is calculated as $U = Q/b^2$, and the uncertainty in velocity may be estimated using the following expression [63]

$$w_U = \sqrt{w_{Q,tot}^2 + \left(\frac{2e_b}{l}\right)^2} \quad (5.1)$$

Resulting in an uncertainty of $w_U = 0.67\%$ in test section velocity.

5.5.2 Uncertainty in Frequency and Repeatability

The frequencies of foil vibration and vortex shedding were obtained based on Fourier transforms of fluctuating strain signals and velocity vectors. Due to a combination of time-constraints and software limitations, the propagation of uncertainty in the measure value was not propagated into the Fourier transform. An uncertainty analysis of the individual frequencies was therefore not performed. However, three measurements were performed at the velocity of 11 m/s , and the uncertainty in repeatability of the measured frequency may therefore be quantified. Using (2.17) the values may be determined as presented in table 5.6.

Table 5.6 – Uncertainty in repeatability

Uncertainty	Description	Value
$w_{f,Strain}$	<i>Uncertainty in repeatability of vibrational frequency</i>	$\pm 0.070\%$
$w_{f,PIV}$	<i>Uncertainty in repeatability of vortex shedding frequency</i>	$\pm 0.102\%$

5.5.3 Uncertainty in PIV Measurements

Despite numerous applications, theory and contributions, a thorough, widely accepted framework for reliable quantification of PIV measurement uncertainty has not yet been presented [96], [97]. PIV methods include several variables and involve instrument and algorithm chains with coupled uncertainty sources which makes uncertainty quantification far more complex than most measurement techniques [75], [96]. Choice of IW size, particle size, seeding density, image acquisition settings all contribute to the random uncertainty of the system [66]. Incorrect positioning of laser sheet and camera contribute to the systematic error, but is somewhat included in the calibration error. For the scope of this thesis, only a discussion of some of the individual errors are provided.

In an ideal and noise-free measurement, all particles are recognized in both image frames of an image recording. In the real case however, this is not the case, and uncertainties are related to individual uncertainties in the location of the cross-correlation peaks [73]. The individual uncertainty in velocity vectors is calculated using statistical comparative methods which analyses each pixels contribution in the cross-correlation calculation [73], [97]. The basis of this analysis is the statistical methods of finding the average, standard deviation, variance and covariance of the sample and implement this in the correlation function [97]. The average and standard deviation over time, i.e. over the entire range of samples, may then be calculated by taking the uncertainty of the individual scalar values into account [67]. The uncertainty in the

velocity field may then be visualised as scalar plots of the average uncertainty of the instantaneous velocity uncertainty of all the sampled velocities.

As the PIV measurements in this thesis were of a fluctuating phenomenon, an average of such instantaneous velocity uncertainties would not be representable. However, an uncertainty analysis for each of the obtained velocity fields was performed to get an impression of the uncertainty distribution. Figure 5.16 shows an instantaneous uncertainty plot from the first measurement at 11.1 m/s. The velocity field it represents the uncertainty of is presented in the next chapter. The uncertainty is observed in a range from approximately 2 % up to approximately 6 %. Details regarding this uncertainty analysis will not be discussed further as it is performed by the software, but a full review may be found in the software manual or other literature covering cross-correlation uncertainty analysis [97].

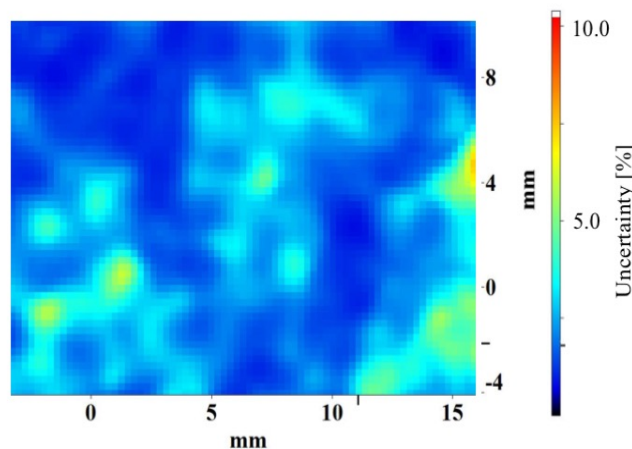


Figure 5.16 – Uncertainty distribution of the instantaneous velocity field at 11.1m/s to be presented in figure 6.3.

Outliers or spurious datasets were discovered for some of the raw datasets, and were mostly related to improper synchronization, visible as blacked-out images. For the few datasets this occurred for, the entire dataset was deleted. The PIV software did not present the option of propagating the uncertainty in velocity into the power spectrum analysis, and the uncertainty in frequency for each measurements is therefore not quantified.

For more information on PIV errors and quantification of PIV uncertainty, the reader is referred to [66].

Chapter 6

Results and Discussion

This chapter presents the results obtained from the PIV- and strain measurements. The results are divided into those regarding the measurements in the blade cascade and those in the Francis turbine. For the Francis turbine, only the expected results are presented, as the measurements themselves were not carried out. Each of the two sections include a discussion of the obtained results in light of theoretical background, previous work, experimental setup and experimental observations.

6.1 Blade Cascade

Obtaining PIV measurements of sufficient accuracy proved to be far more challenging than expected. This was mainly related to the physical size of the hydraulic system compared to the size and frequency of the phenomenon to be investigated. For PIV systems to give accurate and reliable results it is crucial that the design and recording-rules defined in Chapter 3 is fulfilled to the extent possible. For this reason, several weeks, even months, were spent in the laboratory optimizing the experimental setup to achieve sufficient system conditions for the investigations to be made. Achieving a sufficiently high seeding density for the required IW size for vortex detection, and reducing the impact of random particles and particle agglomerations proved to be the most substantial challenges, to be discussed further.

PIV measurements were eventually successfully performed for the OHF. A full risk assessment was performed prior to measurements, with the full report found in appendix C. Due to time constraints and the desire of analyzing the results from the OHF thoroughly before modifying its geometry, it was, in agreement with the supervisor of this work, decided to postpone the measurements on the MHF. However, as the MHF is expected to generate vortices at lower frequencies, performing these measurements should not introduce any unfaced challenges of concern regarding the experimental setup.

The following sections presents the results from the measurements on the blade cascade setup. These are divided into the hydrofoil strain and downstream velocity field results, followed by the results from the frequency and swirling strength analysis of the measured velocity field. Each section includes a discussion of the corresponding results.

6.1.1 Strain Measurements

The vibration of the foil was successfully measured during all of the PIV measurements, and the vibrational frequencies were determined using the MATLAB-scripts found in appendix A1. Table 6.1 summarizes the measured vibrational frequencies for the three measurements at the spanwise center and velocity of 11.1 m/s , while the obtained power spectrum is found in B1. The foil vibrated at a frequency of approximately 644 Hz for all three measurements. This differs by approximately 9 Hz from the vibrational frequency of 635 Hz measured by Ting at 11.0 m/s . The difference may be related to a difference in system parameters e.g.

temperature and pressure, between the experiments, and the use of the PIV seeding system. Another explanation is the slight difference in test section velocity, which, as discussed in section 2.4.1, affects the vibrational behavior of the foil. However, measurements are performed within the lock-in velocity range, and as exacerbated by Bergan et.al, this situation may be problematic to analyse regarding frequencies, and differences are expected to occur [82]. The measured vibrational frequency is observed as being close to the frequency of 631 Hz observed by Ting, where peak vibrational amplitudes were measured using excitation at the corresponding velocity.

Table 6.1 – Peak vibrational frequency for the three measurements at 11.1 m/s, with external seeding

<i>Measurement no. [-]</i>	<i>Vibrational frequency [Hz]</i>
1	643.8
2	643.5
3	643.8

Figure 6.1 presents the power spectrum for the investigated velocity range. The amplitude of the strain measurements were not quantified or calibrated during the experiments as it was primarily the relations of amplitudes and the specific frequencies that were of interest. The amplitude in the power spectrum therefore only represent the amount of the specific frequency in the measurement. Note that these measurements were performed without the external seeding system in use. The measurements revealed the peak vibrational amplitude to occur at 11.6 m/s, and not at 11.1 m/s as expected from Ting's measurements. This is believed to be due to the difference in pressure, possible difference in temperature and the high seeding density.

As the frequency amplitude of the power spectrum represents the amount of the certain frequency present in the original time-varying signal, a high amplitude indicates a high presence of the corresponding frequency in the input signal. The high frequency amplitude for the 11.1 m/s – 12.1 m/s measurement therefore indicates a significantly more consistent vibrational frequency in this velocity range. According to the definitions presented of lock-in, this suggests the foil to be in lock-in mode and vibrate close to its natural frequency. This is in agreement to Bergan's findings where lock-in was found in the 10 m/s – 12 m/s range.

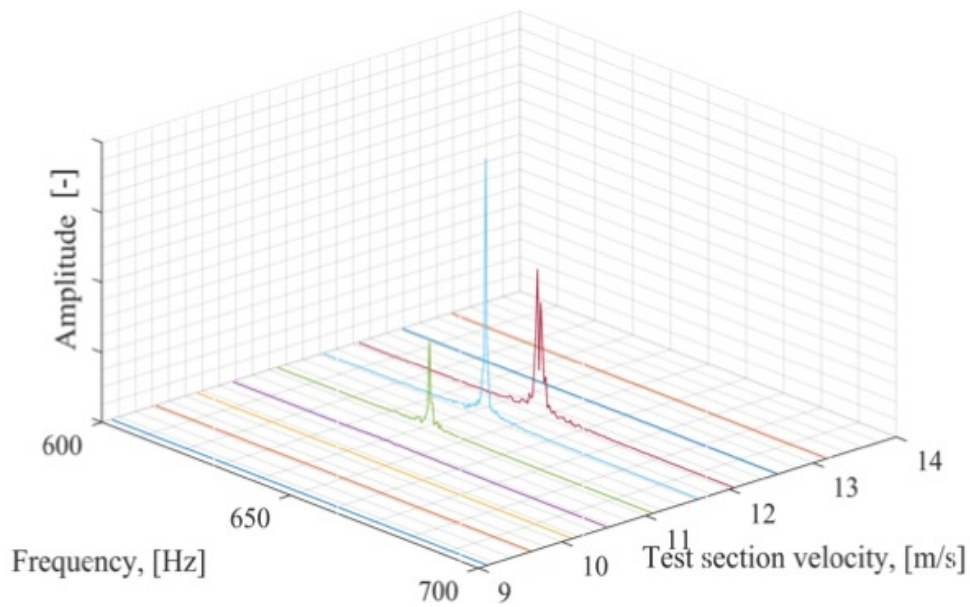


Figure 6.1 – Foil vibrational frequency for velocity range from 9.1 – 13.1m/s, at steps of 0.5 m/s.

The plot in figure 6.1 only gives useful information regarding identification of the region where the foil vibrates the most, and does not provide useful information on the foil's vibrational behavior for the remaining velocities. By normalizing the power spectrum amplitudes to the corresponding maximum amplitude for each velocity, the frequency distribution becomes more evident as shown in figure 6.2. The foil vibration at all velocities is now more thoroughly mapped, with the peak vibrational frequencies in the power spectrum tabulated in table 6.2.

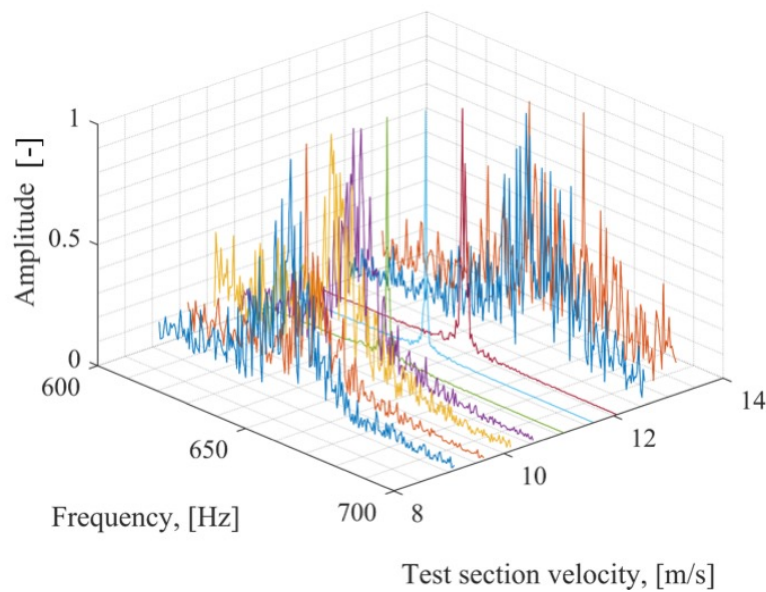


Figure 6.2 - Normalised foil vibrational frequency for velocity range from 9.1 m/s – 13.1 m/s.

The normalized power spectrum shows that outside the 11.1 m/s – 12.1 m/s range, several frequencies coexist, while a clear, distinctive frequency occurs in this range, also suggesting the situation to be locked-in.

An interesting observation is the measured frequency at 11.1 m/s, which has decreased by approximately 3 Hz compared to the one measured with the external seeding system active. This supports the argument of foil frequency to be affected by the presence of a higher density of seeding particles or the possible disturbance in pressure from the seeding system. A slight decrease in vibrational frequency is observed from 9.1 m/s-10.1 m/s before it is fairly steady at approximately 640 Hz - 644 Hz in the velocity range 10.1 m/s-11.6 m/s, suggesting the foil and vortex shedding to be locked-in. For velocities above 11.6 m/s the frequency seems to increase drastically. However, conclusions regarding trends outside the lock-in velocity range would require more data as the performed measurements only show the vibrational frequencies for a limited velocity range.

Table 6.2 – Peak vibrational frequency for velocity range of 9.1 m/s-13.6 m/s, without external seeding

U [m/s]	Frequency [Hz]
9.1	644.7
9.6	640.2
10.1	639.6
10.6	641.6
11.1	640.7
11.6	643.5
12.1	648.1
12.6	659.9
13.1	668.3

6.1.2 Velocity Field Measurements

Obtaining a sufficiently resolved velocity field turned out to be highly challenging as mentioned. Similar measurements of flow around hydrofoils of comparable size are usually performed in closed loops with significantly lower volume than the one utilized in this experiment. Such smaller loops may easily be saturated by seeding particles, allowing for both a steady and highly adjustable system seeding density. As saturating the entire system in the Waterpower Laboratory to the ideal density would require an enormous amount of particles, possibly deteriorating system components and affecting other ongoing experiments, this was not possible. However, a certain degree of saturation was achieved in the blade cascade loop after numerous particle feedings, but this water had to be interchanged for other ongoing projects to be carried out. The main challenge of in this work was therefore related to achieving a sufficiently high seeding density for PIV measurements. The requirement of high seeding density was further accentuated by the objective of investigating vortices, which requires a high vector resolution to be identified, as exemplified in figure 3.3 in section 3.2. The initially installed seeding pump was not capable of delivering a sufficiently high seeding flowrate, and a new system had to be developed. Seeding the system locally, i.e. close to the AOI, using an external seeding pump and a pitot tube was tested, but did not provide a sufficiently high density. A centrifugal pump capable of delivering a sufficiently high flowrate at pressures less than 1.3 *bar* was eventually installed and used.

Large amounts of random particles, i.e. particles not originating from the added seeding e.g. rust flakes and sand, together with problems with particle agglomerations in the seeding tank, made the optimization procedure of the PIV setup highly challenging. Large particles have a larger surface and therefore reflect more light when illuminated. This introduced challenges regarding the dynamic range of the camera chip and the digital size of the particles. For the camera chip not to be saturated in the presence of large particles in the FOV, the laser intensity had to be reduced, which in turn reduced the visibility of the added non-agglomerated seeding particles. For this reason, a compromise between laser intensity, particle visibility, particle size and dynamic range was required. The laser intensity was adjusted such that the seeding particles were sufficiently illuminated, while the illumination of the random and agglomerated particles highly exceeded the dynamic range of the camera chip – appearing as large, bright particles voiding the design condition regarding dynamic

chip – appearing as large, bright particles voiding the design condition regarding dynamic range and particle size. However, reducing the impact of these large particles digitally through pre-process-filtering proved to be highly efficient as shown in section 5.3.6.

Eventually, sufficient seeding density for the required IW size for vortex detection was achieved at the desired velocities. The optimum FOV size had to be found through trial and error, and recalibration and design of calibration plates was necessary for each FOV size. The obtained velocity fields revealed a fairly unsteady flow field containing a large amount of smaller fluctuations and disturbances, for all measurements. For the velocity range investigated, (2.3) results in a Reynolds number range of $2.2 \cdot 10^6 < Re < 3.4 \cdot 10^6$, and a narrow, turbulent and three-dimensional wake affected by disturbances and several eddy frequencies was indeed to expect according to the wake flow description given in Chapter 2.

Figure 6.3 shows an instantaneous velocity field obtained from the first PIV measurement at 11.1 m/s . No obvious local extremums or rotation for vortex identification in the flow was found by visual inspection of the velocity field. The wake and its fluctuations however, were easily observed in a relatively steady manner, represented by the light blue color in the figure. Following the directions of the velocity vectors gives a slightly curved streamline as indicated by the bold dashed line in the figure. Such wavy behavior was observed for the majority of observed velocity fields, and will be analysed further in the next section.

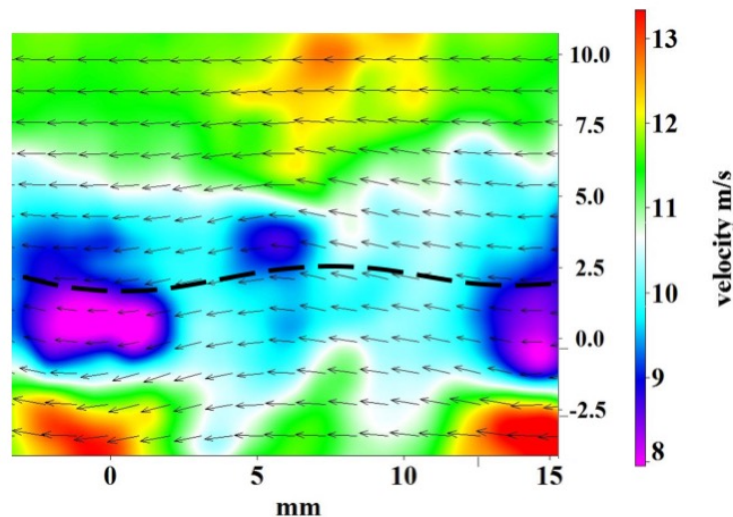


Figure 6.3 – Instantaneous velocity field for the first measurement at 11.1 m/s .

In agreement with the wake-flow analysis given in Chapter 2, the velocity field was time-averaged to investigate the wake profile. The time-averaged velocity field for the first measurement at 11 m/s is presented in figure 6.4. The average wake thickness is observed to be of a width of approximately 12 mm , which is reasonable compared to the foil thickness of 12 mm . The average velocity outside the wake was measured to approximately 12 m/s . Based on the volumetric flow rate and the flow area past the hydrofoil, a rough estimation of the average velocity gives a velocity of approximately 12.0 m/s past the foil, excluding BL displacement thicknesses. The PIV-measured average velocity of 12 m/s may therefore be regarded as reasonable.

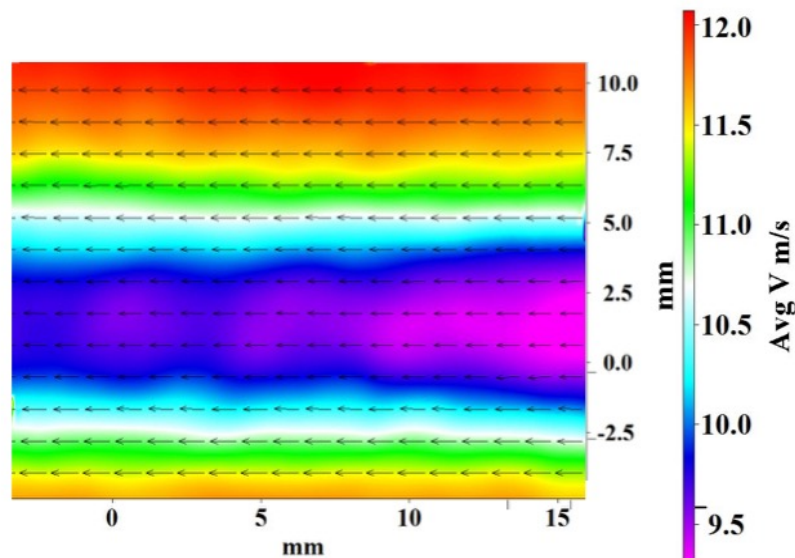


Figure 6.4 – Average velocity field for first measurement at 11.1 m/s.

Following the wake's center line in the downstream direction shows a decrease in downstream velocity. This indicates that the maximum wake velocity has been achieved, and that measurements are performed in the mixing-region of the wake. Vortices should therefore be properly formed in the AOI according to the vortex formation length defined in 2.1.

6.1.3 Swirling Strength Analysis

As discussed in section 2.2, identifying vortices in a flow may be challenging, which was also accentuated in the previous section. None of the obtained velocity fields showed any distinct rotational motion, and they could be interpreted as being vortex-free. This is mostly related to the fact that the vortices themselves are moving downstream, which makes the rotational motion to be detectable only by analyzing the amplitude of neighboring vectors in the velocity field, i.e. through an operation e.g. a swirling strength analysis. The swirling strength analysis in Davis revealed clear vortices as shown in figure 6.5, which confirms that a velocity extremum is not required for the existence of a vortex, as discussed in 2.2. These vortices occurred in a regular manner periodically, i.e., steady vortex streets were observed for certain periods of the sample, separated by periods of non-evident vortices. Counting vortices per time, and calculating the vortex shedding frequency by use of (2.6) was therefore concluded as inadequate for an accurate frequency calculation.

Depending on the degree of applicability of the flow region description presented in table 2.1, for hydrofoils, it may be argued that the investigated flow is spanning both the fully turbulent and transitional regime regarding vortex shedding. This implies that both a fully turbulent vortex street and a disorganized wake may be expected. Several smaller eddy swirls were observed in the swirling strength field, supporting the expected disturbances and presence of multiple frequencies in turbulent flow. However, the swirling strength analysis did confirm the presence of distinct, dominating vortices in a vortex street formation for certain periods of time, with a frequency best determined through a spectral analysis to be discussed in the next section. The vortices appeared with diameters of approximately 2 mm – 4 mm determined by visual inspection, which is in agreement with being in the scale of the TE thickness as expected.

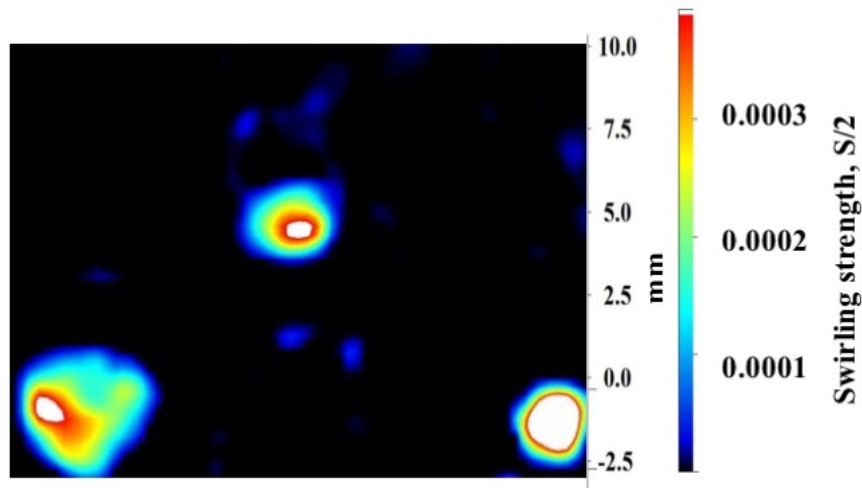


Figure 6.5 – Instantaneous swirling strength field of the velocity field in figure 6.3.

If the swirling field in figure 6.5 is assumed to represent the general vortex distribution in the downstream region, and assuming this to be steady, the strength of the vortices may also be determined using (2.4) for empirical comparison. The longitudinal distance a_l may be determined from the swirling strength field, and the velocity in- and outside the wake may be estimated from the measured velocity field. However, the slope factor k requires the slope of the frequency versus velocity curve to be determined, and this requires a more extensive mapping of the frequency-velocity relationship than performed in this work. In addition, the frequency versus velocity curve is expected to be relatively flat in the lock-in velocity range, and the validity of (2.4) in lock-in is therefore uncertain.

For the work performed in this thesis, the swirling strength analysis was primarily performed for a visual analysis as a confirmation of the presence of vortices in the flow. Although the swirling strength field gives useful information regarding vortex location, it does not provide a visual of the rotational direction and tangential velocities. To obtain a visual of the rotational motion, the velocity field was further processed. The swirling field was used to locate the center of the vortices, and the velocity of the vortices in the downstream direction was found from the corresponding vortex locations in the velocity field. This velocity was then subtracted from the entire velocity field, resulting in a velocity field where the vortices are seemingly stationary as presented in figure 6.6. The fluid rotation and its direction is now clearly visible, with a behavior similar to that of the free vortex introduced in Chapter 2 with a relatively distinct vortex center. The difference from a free vortex is seen in the non-constant tangential velocity around the center, which makes (2.2) inadequate for simple strength estimations. Although these images may provide improved understanding of the downstream flow, such images are rough approximations as they assume each vortex to move with the same downstream velocity, and primarily serve a visual purpose.

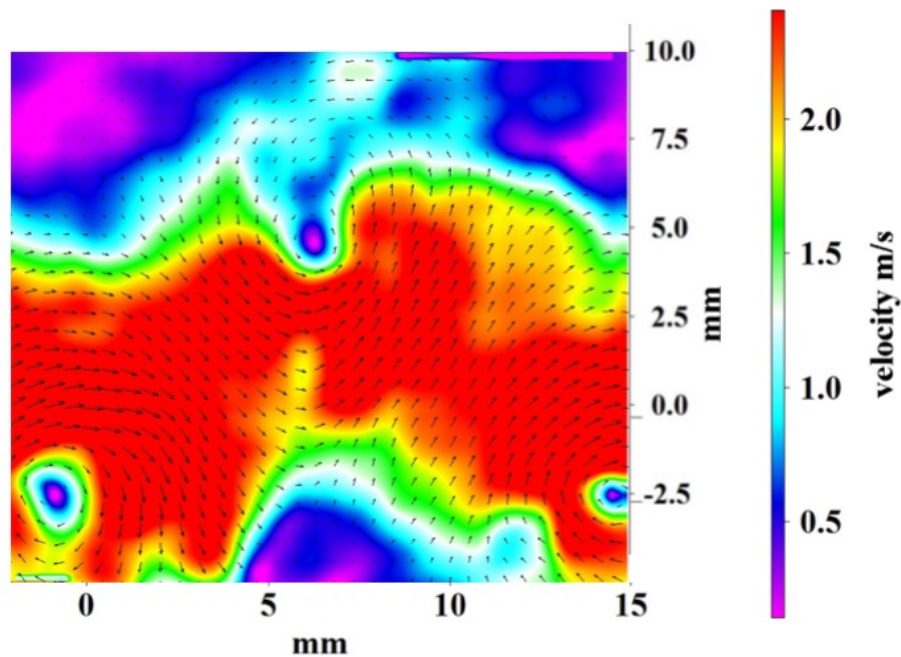


Figure 6.6 – Instantaneous vortex-velocity field representation of the velocity field in figure 6.3.

6.1.4 Vortex Shedding Frequency Analysis

From the velocity field it was evident that a fairly steady wake fluctuation was apparent, and a clear relation between the wake's velocity field fluctuations and the presence of vortices has been presented in the previous section. Hence, an analysis of the velocity field fluctuation frequency is analogous to an analysis of the vortex shedding frequency. The PIV power spectrum data was imported into MATLAB and analysed using the scripts found in appendix A2.

Measurements at 11 m/s

The power spectrum based on the fluctuation showed distinct peaks for all measurements performed at 11.1 m/s, with the three-dimensional power spectrum itself is found in appendix B2. Figure 6.7 shows the two-dimensional power spectrum for all four measurements, which serves as a visual comparison for the power spectrum presented by Heggebø in figure 4.5. Notice how the measured frequencies overlap. A similar plot with a more narrow frequency range is found in appendix B2, indicating the precision of the peak and degree of overlap.

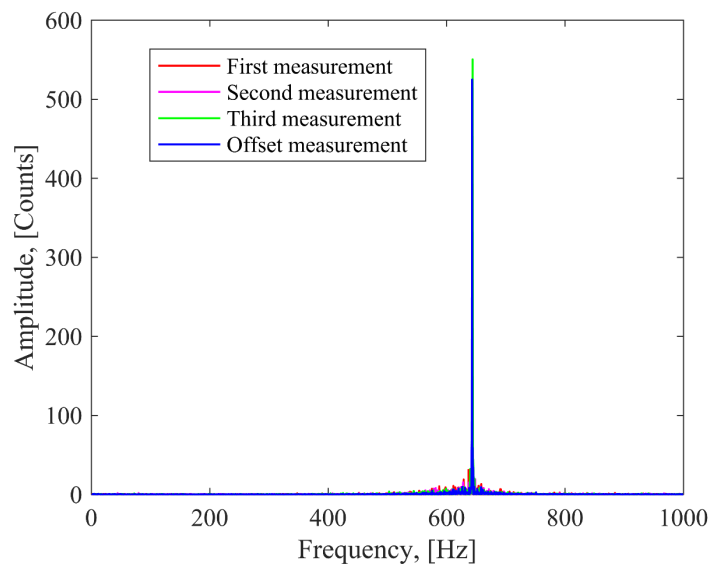


Figure 6.7 – Power spectrum for the four measurements at 11.1 m/s. Three measurements in the spanwise center and one in the 10mm spanwise offset position.

The dominating frequencies, tabulated in table 6.3, was found to be approximately 644 Hz for the three measurements in the spanwise center, and 643 Hz for the 10 mm offset position. The difference of 1 Hz suggests the position-dependency of the vortex shedding frequency in the mid-part of the foil to be insignificant. However, a larger spanwise range should be investigated before such conclusions can be made.

The frequency distribution in the spanwise center was mapped for several additional areas in the velocity field to determine the frequencies' dependency of downstream position. No significant variation was observed, and the chosen area was therefore concluded as representable for the flow.

Table 6.3 – Vortex shedding frequency for the four measurements at 11.1m/s, with external seeding.

<i>Measurement</i>	<i>Vortex shedding frequency</i> [Hz]
<i>1</i>	<i>643.9</i>
<i>2</i>	<i>643.5</i>
<i>3</i>	<i>643.9</i>
<i>10mm offset</i>	<i>643.0</i>

The measured frequency peaks dominated the power spectrum, and other coexisting frequencies were seemingly negligible. This was not entirely as expected, as the velocity field and swirling plots showed a high degree of disturbances expected to have a significant impact on the power spectrum. The distinct frequency of approximately 644 Hz coincides with the measured vibrational frequency at this velocity, also suggesting the frequencies to be locked-in. However, whether the lock-in situation persists for a change in velocity or not, which is the

true nature of the lock-in phenomenon, is best answered by analyzing the velocity range measurements – to be discussed later.

According to (2.10), the vortex shedding frequency is determined to 546.1 *Hz* at the corresponding velocity investigated. This deviates by approximately 100 *Hz*, or 15 %, from the measured value. This may be related to the simplification of the constant Strouhal number and BL thickness in the equation. Assuming the $St - Re$ relationship presented in figure 2.5 to be representative for hydrofoils, the measurements are performed in a region with increasing Strouhal-numbers, i.e. increasing from the constant value of 0.2. Using (2.7), (2.8) and (2.9) with the measured vortex shedding frequency of 644 *Hz*, gives Strouhal numbers of approximately 0.28 and 0.22 respectively, i.e. the Strouhal number without and with the TE geometry taken into account. This suggests the Strouhal number to be higher than 0.19 as assumed in (2.10), which is reasonable concerning the previously mentioned Strouhal number range of 0.15-0.3 found for hydrofoils.

Another, more likely explanation for the deviation between empirical values and measured values may be related to lock-in and FSI. FSI is a two-way interaction, and as discussed in section 2.4.1, the vortex shedding and vibrational frequencies remain locked-in until the deviation between the vortex shedding frequency following the Strouhal-law and the structure's natural frequency becomes sufficiently large. A constant Strouhal-number as used in (2.10) implies a constant, linear relationship between velocity and vortex shedding frequency, which is not the case in lock-in. As the measurements are performed in the lock-in velocity range of the foil it is, by the definition of lock-in, highly reasonable that the measured vortex shedding frequency deviates from the empirically calculated value.

The validity of the experimental formulas for the specific structure investigated would best be determined by obtaining experimental measurements of vortex shedding frequencies for a large velocity range both in-and outside lock-in, followed by a thorough comparison with empirical data. This would be interesting measurements and should be considered as further work.

The measured vortex shedding frequency is approximately 114 *Hz*, or 21 %, higher than the one found through Heggebø's simulations. This is believed to be related to the simplification of a two-way FSI simulation, as is also the conclusion by Heggebø. The one-way FSI in Heggebø's simulations does not include the foil's vibrational impact on the surrounding fluid and thereby the vortex shedding. Hence, the simulated vortex shedding will only be valid, and describe the vortex-shedding, for a velocity outside the velocity-range of lock-in, i.e. in a flow regime where the vortex shedding follows the Strouhal-law. This is in agreement with the correspondence between the simulated and empirically calculated frequency. However, CFD contain uncertainties related to choice of mesh, turbulence models and time-steps, and obtaining accurate estimations of a phenomena as complex as turbulent vortex shedding is highly challenging [98], [99]. Further work should be performed for the simulations, and a two-way FSI should be performed to include the effects of lock-in.

Velocity Range

The PIV measurements for the velocity range turned out to give some highly interesting results. Figure 6.8 presents the power spectrum obtained for all PIV measurements, where the amplitude refers to the number of counts in the DTFT of the velocity field. A distinct peak occurs for the velocity of 11.6 m/s, and the power spectrum is generally similar to that obtained for the foil vibration for the velocity range, again suggesting lock-in behavior.

As previously mentioned, the vortices observed in the swirling strength plots occurred in a relatively steady manner for periods of time. The high frequency amplitude for the 11.6 m/s measurement may indicate a more steady velocity fluctuation, i.e. a more steady vortex shedding frequency at this velocity. A lack of such high amplitudes for the other velocities therefore implies a less steady vortex shedding frequency, i.e. longer periods of unsteady vortex shedding.

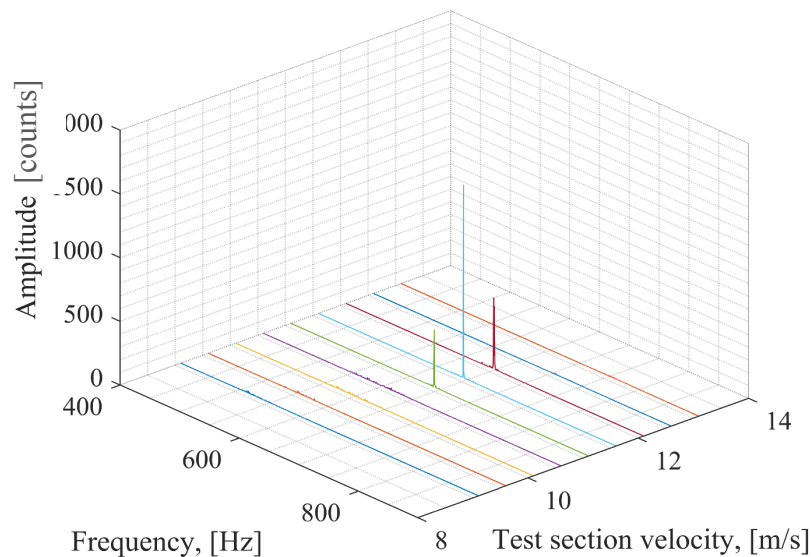


Figure 6.8 – Power spectrum of vortex shedding frequency for velocity range from 9.1 m/s – 13.1 m/s, at steps of 0.5 m/s.

Figure 6.9 presents the power spectrum normalised in a similar manner as the strain-measurements, i.e. according to the individual power spectrums' peak amplitude, with the peak values tabulated in table 6.4. The normalised power spectrums show that a range of frequencies coexist with large amplitudes relative to the maximum amplitude, for the velocities below 10.6 m/s and above 12.1 m/s. For the measurement in the 10.6 m/s – 12.1 m/s range however, these coexisting frequencies become negligible compared to the high amplitude of the peak frequency, visible by the single distinct amplitude and frequency of the peak. This suggests the vortex shedding frequencies and the foil vibrational frequencies to be locked in in this velocity range, in agreement with the findings by Bergan et.al, but again, it is the non-changing vortex shedding frequency for a velocity change which truly determines whether the situation is locked-in or not. A comparative two-dimensional plot showing the low-amplitude power spectrum for the velocity range is found in appendix B2, showing the coexisting frequencies for the lock-in velocity range measurements also.

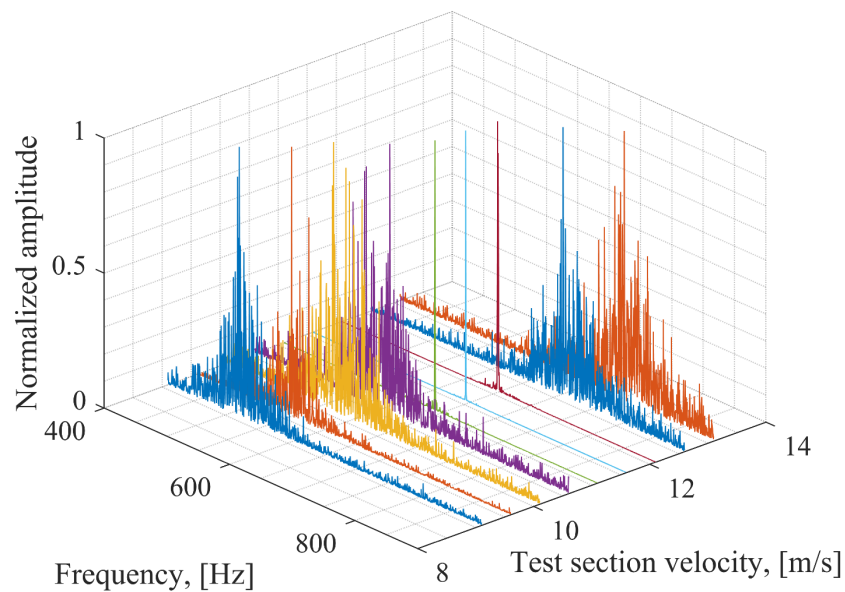


Figure 6.9 – Normalized power spectrum of vortex shedding frequency for velocity range from 9.1 – 13.1 m/s, at steps of 0.5 m/s.

The frequency peaks are tabulated in table 6.4, and indicate an increase in vortex shedding frequency to occur from 9.1 m/s to 11.1 m/s. From here it stays relatively unchanged up to 12.1 m/s before it increases again. Recall that these measurements were performed without using the external seeding system. The vortex shedding frequency has dropped by approximately 4 Hz at the velocity of 11.1 m/s compared to the measurements where the external seeding system was active. This is believed to be related to the previously discussed impact of the seeding system.

Table 6.4 – Measured vortex shedding frequencies for velocity range of 9.1m/s-13.6m/s, without external seeding.

U [m/s]	Frequency [Hz]
9.1	513.9
9.6	551.0
10.1	571.6
10.6	615.1
11.1	640.7
11.6	643.5
12.1	648.0
12.6	706.2
13.1	757.5

6.1.5 General Discussion

The plot in figure 6.10 summarises the measurements performed in the blade cascade, and may be regarded as the key result of the blade cascade experiment. The dominating vibrational- and vortex shedding frequencies are plotted together with the empirically estimated frequencies by (2.10) using both 0.19 and the suggested 0.22 as Strouhal numbers. From this plot it is evident that the vortex shedding frequency and foil vibrational frequency coincide in the velocity range 11.1 m/s to 12.1 m/s, at frequencies increasing from approximately 640 Hz to 648 Hz. This indicates that the vortex shedding frequency tend to stay unchanged despite a change in velocity, and it may thereby be concluded that the lock-in phenomena indeed occurred in the measurements. This confirms the need of a two way FSI-analysis for a proper vortex shedding simulation. Comparing this plot to the typical lock-in plot as presented in Chapter 2, figure 2.7, the lock-in behavior is well recognized and identified.

Compared to the empirically estimated vortex shedding frequency indicated by the green line in figure 6.10, the measured vortex shedding frequency is higher for all velocities. As already discussed, the empirical formula is not believed to give reliable vortex shedding frequency estimations in the lock-in region, but it was expected to do so outside the lock-in velocity range. However, as the empirical formula seems to undershoot the measured vortex shedding frequency with a seemingly constant offset, this may suggest the assumed Strouhal number to be too low. The dashed line show the empirically estimated frequency using (2.10) with the Strouhal value of 0.22 as calculated previously, which seem to give results in more agreement with the measured value. Although the increased Strouhal number gives more reasonable values for the investigated velocity range, i.e. close to lock-in velocities, a larger velocity range should be investigated before any conclusions are drawn.

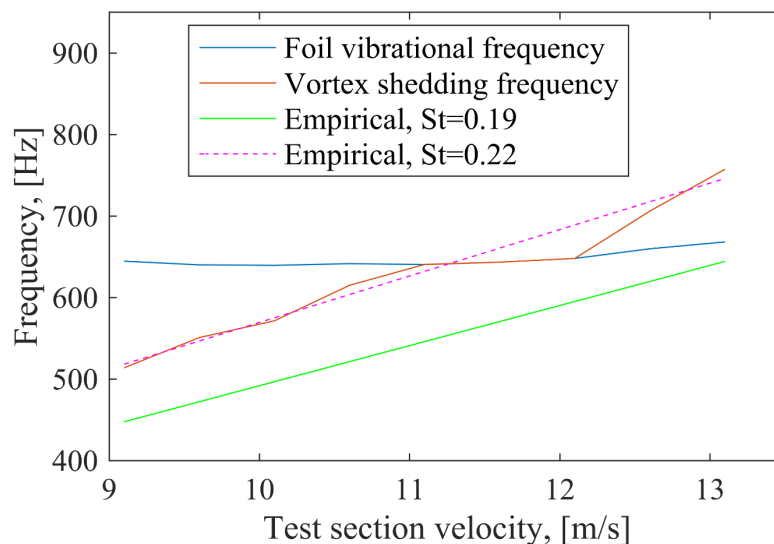


Figure 6.10 – Measured vortex shedding frequency, foil vibrational frequency and empirically estimated vortex shedding frequency using Strouhal numbers of 0.19 and 0.22.

From the measured data and discussions above, it is clear that the vibrational behavior of the foil has a direct impact on the downstream velocity field. The vortex shedding is shown to have significantly more distinct characteristics in lock-in mode.

For the MHF, all measurements performed on the OHF should be carried out. The strain measurements are not expected to change significantly, but the vortex shedding frequencies should be observed as significantly lower compared to that of the OHF. By calculating the swirling strength and vortex-velocity field using the same system settings as for the OHF, comparisons regarding strength, velocities and velocity distributions can be performed and used as indicators for changes regarding the individual vortices in the vortex street. The power spectrum should be obtained for a velocity range, and a similar analysis as for the OHF should be performed. In addition, a thorough evaluation of TKE from the PIV measurements should be included for a more thorough comparison with the simulations.

From the findings by Thomareis and Papadakis, discussed in section 2.5.2, the serrations are expected to generate a spanwise decorrelation of the vortices, as is also evident from the power spectrum by Heggebø in figure 4.5 which shows that multiple distinct frequencies are present. A large spanwise area of the MHF should therefore be investigated to determine the degree of spanwise decorrelation experimentally. This could also give an indication of which of the frequencies along the TE is the primary, or dominating, vortex shedding frequency. Whether a shift in lock-in velocity range as that presented in figure 2.7 is achieved or not, should be investigated by obtaining a corresponding plot as that in figure 6.10, for the MHF. The velocity range should be even larger to gain a thorough understanding and mapping of the vortex shedding behavior of the MHF.

6.2 Francis Turbine

Due to time-constraints, no measurements were performed on the Francis turbine. However, parts of the experimental setup was prepared, and a recommended experimental setup has been provided. Measurements are to be performed in future work, and this section presents a discussion of the requirements of the experimental setup together with the expected results.

As the particle-feeding system has already been developed and tested, the remaining main challenges for the Francis measurements are related to the development of an adequate calibration device and a proper synchronization system for the measurements which are to be carried out simultaneously.

The Francis turbine setup presents a challenge regarding positioning of calibration plates in the AOI. Compared to the test unit in the blade cascade, the Francis turbine is a more complex structure with less accessibility to the AOI. In addition, the system needs to be drained and filled for mounting the calibration device and performing the calibration, respectively. In the blade cascade, the AOI could be accessed while the system was partially filled, allowing for easy calibration and mounting of the calibration device. For the Francis turbine, however, the turbine must be completely drained for mounting of the calibration device, refilled for calibration, and drained again for removal of the calibration device. This makes the calibration procedure a time consuming process. As the laser sheet enters the spiral casing through a curved surface, the calibration device should also contain indicators which allows for a proper alignment of the laser sheet.

Another challenge is related to refraction of the laser light as it passes through the multiple plecgilas parts. The degree of refraction has already been studied by the author on a small unit replicating the PIV-section of the Francis turbine, showing adequate illumination in the AOI [3]. However, the refraction depends on the exact position of the laser, and challenges with shadows in the AOI is expected to occur.

For the PIV measurements, the main dynamics of the velocity field is expected to be acquired without any challenges of concern related to the PIV equipment's capacity. For capturing vortex shedding however, similar challenges as those in the blade cascade setup is expected to occur, i.e. problems with achieving sufficient seeding density. As explained in section 3.2, the required seeding particle amount increases with reduced IW size. Obtaining a similar vector resolution as for the blade cascade measurements would require approximately a quadruple seeding density, as the Francis IW size would need to be reduced from the estimated size of 128 to 64.

The flow in the wicket gate is expected to achieve velocities up to 15 m/s . According to (2.10), the expected vortex shedding frequency from the GV's TEs is approximately 2145 Hz . From (2.11), the required sampling frequency would then be 4290 Hz . This requires the system frequency to be increased, on the cost of reduced image resolution. However, as previously discussed, being able to spot wake fluctuations may be used to indicate vortex shedding frequency, despite not having clearly visible vortices. The system is believed to be able to capture these fluctuations. These measurements may then ultimately be utilized to observe if the vortex shedding frequency may be altered by means of modifying the GV's of the turbine.

Chapter 7

Conclusion

The work presented in this thesis has been part of the ongoing work in the Waterpower Laboratory at NTNU on gaining knowledge and possible mitigation of fluid-structure interaction (FSI) and pressure-pulsations occurring in a high head Francis turbine. Two experimental setups have been investigated with the purpose of determining the relation between the velocity field and FSI for flow around a hydrofoil and in the vaneless space of a Francis turbine. A review of the fundamentals of FSI and particle image velocimetry (PIV) has been presented and used to design and optimize the experimental setups.

The first experimental setup was devoted to PIV measurements in the downstream region of a hydrofoil resembling a Francis runner blade, to map the vortex shedding frequencies for a velocity range where lock-in occurred. Simultaneous measurements of foil vibration were also performed to determine the degree of FSI. The objective was to investigate if the vortex shedding frequency and lock-in velocity-range could be altered by means of adding a sinusoidal-serrated trailing edge (TE) to the hydrofoil. Due to time-constraints, the TE modifications were not implemented, and whether the modifications work as intended or not remains to be answered in further work.

PIV measurements on the original hydrofoil, however, were successfully performed. The vortex shedding and foil vibrational frequency were observed as locked-in for a velocity range of 11.1 m/s - 12.1 m/s , at frequencies increasing from approximately 640 Hz to 648 Hz . The downstream velocity field of the foil proved to be highly dependent on whether the hydrofoil was in lock-in mode or not, where a significant increase in vortex shedding frequency stability was found during lock-in. Outside the lock-in velocity range the vortex shedding frequency was found to follow the Strouhal law for hydrofoils, where a Strouhal number of 0.22 was suggested to be used instead of the empirically estimated value of 0.19. The measured vortex shedding frequency was observed to be approximately 21 % higher than the frequency found through simulations. This deviation is expected to be related to the simplification of a one-way FSI, not including the effect of lock-in on the vortex shedding frequency.

Numerous challenges in obtaining reliable PIV measurements were faced during the work. Achieving a sufficiently high seeding density for vortex detection and the occurrence of random particles and seeding particle agglomerations proved to be the most substantial challenges. A dynamic particle seeding system capable of assuring high particle densities in a large, pressurized piping system was developed and is regarded as a significant part of the achieved results.

The second experimental setup was devoted to PIV measurements in the vaneless space of a modified Francis turbine model to determine the velocity distribution in this area. The objective was to use the measurements as a comparative basis for flow simulations in the region, in addition to couple the velocity field development to pressure pulsations in the turbine runner and rotor stator interaction (RSI). Due to time-constraints, these measurements

were not performed. However, a description and recommendation for the experimental setup have been provided, together with a discussion of the expected results.

Chapter 8

Further Work

Based on the measurements and investigations carried out in this work, areas in need of optimizations have been discovered and recommendations for further work have been made.

Blade Cascade

Similar measurements as the ones performed should be carried out for a larger velocity range for the OHF to gain knowledge and data of the hydrofoil's behavior outside lock-in. This may be used to evaluate the reliability of the suggested Strouhal number, and may also serve as useful comparative data for the measurements to be made on the MHF. A larger spanwise position-range should also be investigated to determine three-dimensionality of the vortex shedding.

Obviously, measurements should also be carried out on the MHF to determine whether the modifications have the desired effect or not. Further measurements should also include an analysis of TKE as this allows for a more detailed comparison with the simulated data, but also between the measurements on the OHF and MHF. Measurements should be performed at several different spanwise positions, to determine the decorrelation of vortices and the primary, or dominating, frequency/frequencies of the vortex shedding.

From the measurements it is evident that the simulated results require adjustments. A two-way FSI analysis is suggested, to include the effects of lock-in. Whether a one-way FSI is adequate outside the lock-in velocity range should also be investigated, as this might save computational time for conditions where lock-in is known to not occur.

Regarding the experimental setup itself, it remains to determine the possible impact of the seeding system on the system parameters and resulting measurements. If the impact is regarded as significant, alternative seeding systems or system saturation should be evaluated.

Francis Turbine

The experimental setup for the Francis turbine should be set up according to the suggestions given. Measurements of the overall velocity distribution in the wicket gate and vaneless space should be performed. A calibration device allowing for a proper, spatial calibration in the vaneless space should be designed and produced. The PIV system should be coupled to the pressure measurements to be made, for correlational purposes, and a system allowing for synchronization of pressure- and PIV measurements should be developed. These measurements should then be compared to simulated data for this region as a validation of the simulations. The PIV system's ability of determining the vortex shedding frequency from the turbine's GVs should also be investigated.

Ultimately, if the modifications on the MHF work as intended, this TE geometry should be applied to the turbine's GVs, followed by PIV investigations of the resulting impact of this on the vaneless space velocity field and RSI.

References

- [1] J. Twidell and T. Weir, *Renewable Energy Resources*, 3 edition. London ; New York: Routledge, 2015.
- [2] N. Kroner, R. Bérubé, and B. N. Kroner, “Maintaining power grid reliability through individual unit stability,” *HydroVision*, pp. 1–10, 2008.
- [3] M. T. Bolstad, “Design and Investigation of Experimental Setups for Vortex Shedding Measurements in a Francis Turbine,” Project Thesis, Norwegian University of Science and Technology, Trondheim, 2017.
- [4] H. Brekke, “A Review on Oscillatory Problems in Francis Turbine,” *New Trends Technol. Devices Comput. Commun. Ind. Syst. Sciyo*, pp. 217–232, 2010.
- [5] A. Coutu, M. D. Roy, C. Monette, and B. Nennemann, “Experience with rotor-stator interactions in high head Francis runner,” in *24th IAHR Symposium on Hydraulic Machinery and Systems (IAHR, 2008)*, 2008.
- [6] P. Dörfler, M. Sick, and A. Coutu, *Flow-Induced Pulsation and Vibration in Hydroelectric Machinery*. London: Springer London, 2013.
- [7] C. Trivedi, “A review on fluid structure interaction in hydraulic turbines: A focus on hydrodynamic damping,” *Eng. Fail. Anal.*, 2017.
- [8] T. J. Mueller, “Low Reynolds number aerodynamics,” in *Proceedings of the Conference Notre Dame, IN*, 1989, vol. 54.
- [9] G. M. Lilley, “A study of the silent flight of the owl,” *AIAA Pap.*, vol. 2340, no. 1998, p. 1-6, 1998.
- [10] “The secrets of owls’ near noiseless wings.” [Online]. Available: <https://phys.org/news/2013-11-secrets-owls-noiseless-wings.html>. [Accessed: 03-Jun-2017].
- [11] E. Sarradj, C. Fritzsche, and T. Geyer, “Silent owl flight: bird flyover noise measurements,” *AIAA J*, vol. 49, no. 4, pp. 769–779, 2011.
- [12] T. Y. T. Wu, “Cavity and Wake Flows,” *Annu. Rev. Fluid Mech.*, vol. 4, no. 1, pp. 243–284, 1972.
- [13] Ø. Antonsen, “Unsteady flow in wicket gate and runner with focus on static and dynamic load on runner,” PhD Thesis, Norwegian University of Science and Technology, Trondheim, 2007.
- [14] H. Schlichting, K. Gersten, E. Krause, H. Oertel, and K. Mayes, *Boundary-layer theory*, 8th ed. Germany: Springer, 2000.
- [15] F. M. White and I. Corfield, *Viscous fluid flow*, vol. 3. McGraw-Hill New York, 2006.
- [16] J. H. Lienhard, *Synopsis of lift, drag, and vortex frequency data for rigid circular cylinders*, vol. 300. Technical Extension Service, Washington State University, 1966.
- [17] Y. A. Cengel and J. M. Cimbala, *Fluid Mechanics*. Boston: McGraw-Hill Education Singapore, 2005.
- [18] J. Anderson, *Fundamentals of Aerodynamics*, 5th ed. New York: McGraw Hill Higher Education, 2010.
- [19] C. H. Berdahl and D. S. Thompson, “Eduction of swirling structure using the velocity gradient tensor,” *AIAA J.*, vol. 31, no. 1, pp. 97–103, 1993.
- [20] V. Kolář, “Brief notes on vortex identification,” in *8th WSEAS International Conference on Fluid Mechanics, 8th WSEAS International Conference on Heat and Mass Transfer*, 2011, pp. 23–28.
- [21] V. Holmén, “Methods for vortex identification,” Master Thesis, Lund University, 2012.

-
- [22] Z.-P. Zang, F.-P. Gao, and J.-S. Cui, "Physical modeling and swirling strength analysis of vortex shedding from near-bed piggyback pipelines," *Appl. Ocean Res.*, vol. 40, pp. 50–59, 2013.
- [23] P. W. Bearman, "Vortex shedding from oscillating bluff bodies," *Annu. Rev. Fluid Mech.*, vol. 16, no. 1, pp. 195–222, 1984.
- [24] D. A. Bourgoyne, S. L. Ceccio, and D. R. Dowling, "Vortex shedding from a hydrofoil at high Reynolds number," *J. Fluid Mech.*, vol. 531, pp. 293–324, 2005.
- [25] B. S. Thapa, O. G. Dahlhaug, and B. Thapa, "Sediment erosion in hydro turbines and its effect on the flow around guide vanes of Francis turbine," *Renew. Sustain. Energy Rev.*, vol. 49, pp. 1100–1113, Sep. 2015.
- [26] B. S. Thapa, "Effects of sediment erosion in guide vanes of Francis turbines," PhD Thesis, Norwegian University of Science and Technology, 2016.
- [27] G. Heskestad and D. R. Olberts, "Influence of trailing-edge geometry on hydraulic-turbine-blade vibration resulting from vortex excitation," *J. Eng. Power*, vol. 82, no. 2, pp. 103–109, 1960.
- [28] A. Zobeiri, "Effect of hydrofoil trailing edge geometry on the wake dynamics," PhD Thesis, École polytechnique fédérale de Lausanne, Lausanne, 2012.
- [29] J. H. Gerrard, "The mechanics of the formation region of vortices behind bluff bodies," *J. Fluid Mech.*, vol. 25, no. 2, pp. 401–413, 1966.
- [30] "Von Karman Vortex." [Online]. Available: <http://juandelacuerva.blogspot.com/2007/04/la-magia-del-movimiento-fluido.html>. [Accessed: 04-May-2017].
- [31] C. A. Gongwer, "A study of vanes singing in water," *J. Appl. Mech.-Trans. ASME*, vol. 19, no. 4, pp. 432–438, 1952.
- [32] C. H. Williamson, "Vortex dynamics in the cylinder wake," *Annu. Rev. Fluid Mech.*, vol. 28, no. 1, pp. 477–539, 1996.
- [33] A. H. Techet, "Lecture notes: Vortex Induced Vibrations," Massachusetts Institute of Technology, 21-Apr-2005.
- [34] R. L. Campbell, "Fluid–structure interaction and inverse design simulations for flexible turbomachinery," PhD Thesis, The Pennsylvania State University, 2010.
- [35] P. Ausoni, M. Farhat, Y. Ait Bouziad, J.-L. Kueny, and F. Avellan, "Kármán vortex shedding in the wake of a 2D hydrofoil: Measurement and numerical simulation," in *IAHR Int. Meeting of WG on Cavitation and Dynamic Problems in Hydraulic Machinery and Systems*, 2006.
- [36] O. M. Griffin, "A universal Strouhal number for the 'locking-on' of vortex shedding to the vibrations of bluff cylinders," *J. Fluid Mech.*, vol. 85, no. 03, pp. 591–606, 1978.
- [37] P. Ausoni, "Turbulent vortex shedding from a blunt trailing edge hydrofoil," PhD Thesis, École Polytechnique Fédérale de Lausanne, Lausanne, 2009.
- [38] M. Mui Bank Ting, "Study of Vortex Shedding From a Vibrating Hydrofoil," Master Thesis, Norwegian University of Science and Technology, Trondheim, 2017.
- [39] C. Monette, B. Nennemann, C. Seeley, A. Coutu, and H. Marmont, "Hydro-dynamic damping theory in flowing water," in *IOP Conference Series: Earth and Environmental Science*, 2014, vol. 22, p. 032044.
- [40] A. Coutu, C. Seeley, C. Monette, B. Nennemann, and H. Marmont, "Damping measurements in flowing water," in *IOP Conference Series: Earth and Environmental Science*, 2012, vol. 15, p. 062060.
- [41] Z. Yao, F. Wang, M. Dreyer, and M. Farhat, "Effect of trailing edge shape on hydrodynamic damping for a hydrofoil," *J. Fluids Struct.*, vol. 51, pp. 189–198, 2014.
- [42] C. E. Brennen, "A Review of Added Mass and Fluid Inertial Forces.," BRENNEN (CE) SIERRA MADRE CA, 1982.
-

-
- [43] T. Rodríguez, F. X. Escaler Puigoriol, E. Egusquiza Estévez, M. Dreyer, and M. Farhat, "The effect of cavitation on the natural frequencies of a hydrofoil," in *Proceedings of the 8th International Symposium on Cavitation*, 2012, pp. 1–4.
- [44] A. Zobeiri, P. Ausoni, F. Avellan, and M. Farhat, "Vortex shedding from blunt and oblique trailing edge hydrofoils," in *3rd IAHR International Meeting of the Workgroup on Cavitation and Dynamic Problems in Hydraulic Machinery and Systems*, 2009, pp. 2005–2009.
- [45] A. Muratoglu and M. I. Yuce, "Performance Analysis of Hydrokinetic Turbine Blade Sections," *J. ISSN*, vol. 2, 2015.
- [46] K. Oshima and Y. Oshima, "Lift generation due to vortex shedding," *Title Inst. Space Astronaut. Sci. Repot SP*, vol. 1, p. 65, 1983.
- [47] R. M. Donaldson, "Hydraulic turbine runner vibration," *ASME J Eng Power*, vol. 78, pp. 1141–1147, 1956.
- [48] Øyvind Antonsen and Torbjørn K. Nielsen, "CFD simulation of von Karman vortex shedding," *IAHR Symposium*, 2004.
- [49] T. Vu, B. Nennemann, P. Ausoni, M. Farhat, and F. Avellan, *Unsteady CFD Prediction of von Kármán Vortex Shedding in Hydraulic Turbine Stay Vanes*. 2007.
- [50] J. O. Young and J. W. Holl, "Effects of cavitation on periodic wakes behind symmetric wedges," *J. Basic Eng.*, vol. 88, no. 1, pp. 163–176, 1966.
- [51] B. Belahadji, J. P. Franc, and J. M. Michel, "Cavitation in the rotational structures of a turbulent wake," *Int. J. Multiph. Flow*, vol. 22, pp. 126–127, 1996.
- [52] P. Ausoni, M. Farhat, X. Escaler, E. Egusquiza, and F. Avellan, "Cavitation Influence on von Kármán Vortex Shedding and Induced Hydrofoil Vibrations," *J. Fluids Eng.*, vol. 129, no. 8, pp. 966–973, Mar. 2007.
- [53] N. Thomareis and G. Papadakis, "Effect of trailing edge shape on the separated flow characteristics around an airfoil at low Reynolds number: A numerical study," *Phys. Fluids*, vol. 29, no. 1, 2017.
- [54] J. Nedić and J. C. Vassilicos, "Vortex shedding and aerodynamic performance of airfoil with multiscale trailing-edge modifications," *AIAA J.*, vol. 53, no. 11, pp. 3240–3250, 2015.
- [55] S. J. Yang and J. D. Baeder, "Effect of Wavy Trailing Edge on 100meter Flatback Wind Turbine Blade," *J. Phys. Conf. Ser.*, vol. 753, no. 2, p. 022060, 2016.
- [56] S. Oerlemans, M. Fisher, T. Maeder, and K. Kögler, "Reduction of wind turbine noise using optimized airfoils and trailing-edge serrations," *AIAA J.*, vol. 47, no. 6, pp. 1470–1481, 2009.
- [57] M. Gruber, P. Joseph, and T. P. Chong, "Experimental investigation of airfoil self noise and turbulent wake reduction by the use of trailing edge serrations," in *16th AIAA/CEAS aeroacoustics conference*, 2010, p. 3803.
- [58] L. E. Jones and R. D. Sandberg, "Acoustic and hydrodynamic analysis of the flow around an aerofoil with trailing-edge serrations," *J. Fluid Mech.*, vol. 706, p. 295, 2012.
- [59] M. S. Howe, "Noise produced by a sawtooth trailing edge," *J. Acoust. Soc. Am.*, vol. 90, no. 1, pp. 482–487, 1991.
- [60] Z. Wei, P. H. Finstad, G. Olimstad, E. Walseth, and M. Eltvik, "High pressure hydraulic machinery," *Compendium*, 2009.
- [61] C. Trivedi, "Investigations of Transient Pressure Loading on a High Head Francis Turbine," PhD Thesis, Luleå University of Technology, Luleå, 2015.
- [62] Øyvind Antonsen, "Ustabile driftsområder for Francisturbiner," PhD Thesis, Norwegian University of Science and Technology, Trondheim, 2002.
- [63] A. J. Wheeler and A. R. Ganji, *Introduction to Engineering Experimentation*, 3 edition. Upper Saddle River, N.J: Pearson, 2009.
-

-
- [64] “Example: Fourier transform,” *PGFPlots.net*. 15-Mar-2014.
- [65] T. Schiwietz and R. Westermann, “GPU-PIV,” in *VMV*, 2004, pp. 151–158.
- [66] M. Raffel, C. E. Willert, S. Wereley, and J. Kompenhans, *Particle image velocimetry: a practical guide*. Springer, 2013.
- [67] *Product Manual: Davis 8.4 Software*. Germany: LaVision GmbH, 2017.
- [68] R. D. Keane and R. J. Adrian, “Theory of cross-correlation analysis of PIV images,” *Appl. Sci. Res.*, vol. 49, no. 3, pp. 191–215, 1992.
- [69] *Product Manual: Imaging Tools*. Germany: LaVision GmbH, 2017.
- [70] *Product Manual: Flowmaster getting started*. Germany: LaVision GmbH, 2017.
- [71] A. Melling, “Tracer particles and seeding for particle image velocimetry,” *Meas. Sci. Technol.*, vol. 8, no. 12, p. 1406, 1997.
- [72] C. J. Kähler, S. Scharnowski, and C. Cierpka, “On the resolution limit of digital particle image velocimetry,” *Exp. Fluids*, vol. 52, no. 6, pp. 1629–1639, 2012.
- [73] *Product Manual: Flowmaster*. Germany: LaVision GmbH, 2017.
- [74] “List of refractive indices,” *Wikipedia*, 15-Feb-2017. [Online]. Available: https://en.wikipedia.org/w/index.php?title=List_of_refractive_indices&oldid=765636904. [Accessed: 21-Mar-2017].
- [75] B. S. Thapa, O. G. Dahlhaug, and B. Thapa, “Flow measurements in the distributor of Francis Turbine: A PIV approach,” in *Effects of Sediment Erosion in Guide Vanes of Francis Turbines*, PhD Thesis., Trondheim: Norwegian University of Science and Technology, 2016.
- [76] R. J. Adrian, K. T. Christensen, and Z.-C. Liu, “Analysis and interpretation of instantaneous turbulent velocity fields,” *Exp. Fluids*, vol. 29, no. 3, pp. 275–290, Sep. 2000.
- [77] Q. Chen, Q. Zhong, X. Wang, and D. Li, “An improved swirling-strength criterion for identifying spanwise vortices in wall turbulence,” *J. Turbul.*, vol. 15, no. 2, pp. 71–87, Feb. 2014.
- [78] B. G. Seim, “Study of Hydrofoil Wakes Using PIV and CFD,” Master Thesis, Norwegian University of Science and Technology, Trondheim, 2009.
- [79] W. Kim, J. Sung, J. Y. Yoo, and M. H. Lee, “High-definition PIV analysis on vortex shedding in the cylinder wake,” *J. Vis.*, vol. 7, no. 1, pp. 17–24, 2004.
- [80] J. H. Tu, C. W. Rowley, J. N. Kutz, and J. K. Shang, “Spectral analysis of fluid flows using sub-Nyquist-rate PIV data,” *Exp. Fluids*, vol. 55, no. 9, p. 1805, Sep. 2014.
- [81] L. Wang, Y. Wang, and Z. Li, “A method to estimate vortex shedding frequency in turbulence,” in *Image and Signal Processing (CISP), 2010 3rd International Congress on*, 2010, vol. 7, pp. 3386–3390.
- [82] C. W. Bergan, B. W. Solemslie, O. G. Dahlhaug, and P. Østby, “Hydrodynamic damping of a fluttering hydrofoil in high-speed flows,” *Submitt. Int. J. Fluid Mach. Syst.*, May 2017.
- [83] K. Heggebø, “CFD analysis of a guide vane,” Project Thesis, Norwegian University of Science and Technology, Trondheim, 2016.
- [84] K. Heggebø, “FSI Investigation of a Hydrofoil,” Master Thesis, Norwegian University of Science and Technology, Trondheim, 2017.
- [85] C. Trivedi, M. J. Cervantes, and B. K. Gandhi, “Investigation of a High Head Francis Turbine at Runaway Operating Conditions,” *Energies*, vol. 9, no. 3, p. 149, 2016.
- [86] C. Trivedi, M. Cervantes, and O. G. Dahlhaug, “A comprehensive report on Francis-99 workshop series,” NTNU, Trondheim, 2017.
- [87] C. Trivedi, M. Cervantes, and O. Dahlhaug, *Experimental and Numerical Studies of a High-Head Francis Turbine: A Review of the Francis-99 Test Case*, vol. 9. 2016.
-

- [88] C. Trivedi, "Investigations of Compressible Turbulent Flow in a High-Head Francis Turbine," *J. Fluids Eng.*, vol. 140, no. 1, p. 011101, 2018.
- [89] C. Trivedi, "Velocity distribution plots." [E-mail]. Available e-mail: chirag.trivedi.ntnu.no., 16-Dec-2016.
- [90] C. Fossen, "HiFrancis - NVKS." [Online]. Available: <https://www.ntnu.edu/nvks/hifrancis>. [Accessed: 06-Jun-2017].
- [91] C. Bergan and B. Solemslie, "MEMO: 3D model of the cascade rig." Norwegian Hydropower Centre, Norwegian University of Science and Technology, 2016.
- [92] "NTNU Reference Turbine Model and Procedure," NTNU, Trondheim, 2007.
- [93] International Electrotechnical Commission, "IEC 60193: Hydraulic turbines, storage pumps and pump turbines - model acceptance tests.," 1999.
- [94] B. W. Solemslie, "Optimalisering av ringledning for peltonturbin," NTNU, Trondheim, 2010.
- [95] P.-T. Storli, "Modelltest av Francis turbin i Vannkraftlaboratoriet ved NTNU," Master Thesis, NTNU, Trondheim, 2006.
- [96] Z. Xue, J. J. Charonko, and P. P. Vlachos, "Signal-to-noise ratio, error and uncertainty of PIV measurement," 2013.
- [97] B. Wieneke, "PIV uncertainty quantification from correlation statistics," *Meas. Sci. Technol.*, vol. 26, no. 7, p. 074002, 2015.
- [98] H. Deconinck and E. Dick, *Computational Fluid Dynamics 2006: Proceedings of the Fourth International Conference on Computational Fluid Dynamics, ICCFD4, Ghent, Belgium, 10-14 July 2006*. Springer Science & Business Media, 2009.
- [99] C. D. Mhalungekar and S. P. Wadkar, "CFD and EXPERIMENTAL ANALYSIS of VORTEX SHEDDING BEHIND D-SHAPED CYLINDER," *Int. J. Innov. Res. Adv. Eng.*, vol. 1, no. 5, 2014.

APPENDICES

APPENDIX A: **Matlab Scripts**

A.1: Strain Analysis

Strain analysis of 11.1m/s measurements

```

% Foil Vibration 11.1m/s.

clc;
clear;
close all;

Data = dir('*Measure.mat');
V_m= zeros(numel(Data, 1));
Q_m= zeros(numel(Data, 1));
Std_dev_Q= zeros(numel(Data, 1));
Std_dev_V= zeros(numel(Data, 1));
f_max= zeros(numel(Data, 1));
mySize = [13,10];

figure(1);
clf;
hold on;
grid minor;
ax=gca;
ylabel('Measurement no., [-]')
xlabel('Frequency, [Hz]', 'fontsize', 12 );
zlabel('Amplitude', 'fontsize', 12);
set(gca, 'FontSize', 12, 'zticklabel', []);
set(gca, 'FontName', 'Times New Roman');

for i = 1:numel(Data)
    load(Data(i).name);
    File = Measurements;
    flow_scale = str2double(File.Flow.properties.Scale); %Scale similar for all
sets
    flow_offset = str2double(File.Flow.properties.Offset); %Offset similar for all
sets

%Detecting PIV pulse
    yPiv=File.PIVpulse.Values;
    Strain = File.Strain.Values;

%Digitalizing PIV pulse
    yPivDigital = yPiv;
    yPivDigital(yPivDigital>2.5)=5;
    yPivDigital(yPivDigital<2.5)=0;
    dy = diff(yPivDigital);
    indRise = find(dy>0);
    indFall = find(dy<0);

%Determining PIV measuring range
    captureRange = indRise(end):indFall(end);
    yPiv = yPiv/max(yPiv);

%Flow, velocity and uncertainty determination
    FlowRAW = File.Flow.Values(captureRange);
    Q = FlowRAW*flow_scale + flow_offset;
    Q_m(i)=mean(Q);
    Std_dev_Q(i)=std(Q);
    VRaw = Q/(0.15*0.15);
    V_m(i) = mean(VRaw);
    Std_dev_V(i)=std(VRaw);

%Foil vibration power spectrum calculation
    Strain_FFT = fft(Strain(captureRange)-mean(Strain(captureRange)));
    Strain_FFT= Strain_FFT(1:ceil(length(Strain_FFT)/2));

```

APPENDICES

```
%Normalizing amplitude
%Strain_FFT=Strain_FFT/max(Strain_FFT);
f=linspace(0,5000,length(Strain_FFT)); %Frequency bins equal for all sets
[amp, ind] = max(Strain_FFT);
f_max(i) = f(ind);
[f, Strain_FFT] = trimData(f, Strain_FFT, 500, 800);

plot3(f, i*ones(size(f)), abs(Strain_FFT));
ylim([0 4]);
yticks([1 2 3]);
yticklabels({'#1', '#2', '#3'});
end
ax.View=[48,35];
save_fig('figur2', 'png', mySize);
save_fig('figur2', 'fig', mySize);

%Uncertainty in repeatability:
std_dev_f=std(f_max);
P_f = 4.303*(std_dev_f/sqrt(3)); %Student t-value of 5%=4.303
```

Strain analysis of velocity range

```
%Foil vibration velocity range
clc;
clear;
close all;

Data = {'91measure.mat', '96measure.mat',
        '101measure.mat', '106measure.mat', '111measure.mat', '116measure.mat', '121measure.mat',
        '126measure.mat', '131measure.mat', };
V_m= zeros(numel(Data, 1));
Q_m= zeros(numel(Data, 1));
Std_dev_Q= zeros(numel(Data, 1));
Std_dev_V= zeros(numel(Data, 1));
P_Q= zeros(numel(Data, 1));
f_max= zeros(numel(Data, 1));
A_max= zeros(numel(Data, 1));
w_cal = 0.12530;

figure(1);
mySize = [16,10];
clf;
hold on;
grid minor;
ax=gca;
ylabel('Test section velocity, [m/s]')
xlabel('Frequency, [Hz]', 'fontsize', 12 );
zlabel('Amplitude', 'fontsize', 12);
set(gca, 'FontSize', 12);
set(gca, 'FontName', 'Times New Roman', 'zticklabel', []);
ax.View=[48,35];
set(0, 'defaultfigurecolor', [1 1 1]);
set(get(gca, 'ylabel'), 'Position', [720, 12, -580]);
set(get(gca, 'xlabel'), 'Position', [650, 8, -600]);

for i = 1:(numel(Data))
    load(Data{i});
    File = Measurements;

    flow_scale = str2double(File.Flow.properties.Scale); %Scale similar for all
sets
    flow_offset = str2double(File.Flow.properties.Offset); %Offset similar for all
sets
```

APPENDICES

```
%FirstMeasure. Detecting PIV pulse
yPiv=File.PIVpulse.Values;
Strain = File.Strain.Values;

%Digitalizing PIV pulse
yPivDigital = yPiv;
yPivDigital(yPivDigital>2.5)=5;
yPivDigital(yPivDigital<2.5)=0;
dy = diff(yPivDigital);
indRise = find(dy>0);
indFall = find(dy<0);

if isempty(indFall)
    disp('empty');
    indFall = length(dy);
end

%Determining PIV measuring range
captureRange = indRise(end):indFall(end);
yPiv = yPiv/max(yPiv);
Strain = Strain/max(Strain);

%Flow, velocity and uncertainty determination
FlowRAW = File.Flow.Values(captureRange);
Q = FlowRAW*flow_scale + flow_offset;
Q_m(i)=mean(Q);
Std_dev_Q(i)=std(Q);
P_Q(i)=1.96*(Std_dev_Q(i)/sqrt(size(Q,1)));
rel_Q(i)=(P_Q(i)/Q(i))*100;
w_tot(i)=sqrt(rel_Q(i)^2+w_cal^2);
VRaw = Q/(0.15*0.15);
V_m(i) = mean(VRaw);
Std_dev_V(i)=std(VRaw);

%Foil vibration power spectrum calculation
Strain_FFT = fft(Strain(captureRange)-mean(Strain(captureRange)));
Strain_FFT= Strain_FFT(1:ceil(length(Strain_FFT)/2));
f=linspace(0,5000,length(Strain_FFT)); %Frequency bins equal for all sets
[amp, ind] = max(Strain_FFT);
f_max(i) = f(ind);
A_max(i)=abs(amp);
[f, Strain_FFT] = trimData(f, Strain_FFT, 600, 700);
plot3(f, V_m(i)*ones(size(f)), abs(Strain_FFT));

end

save_fig('PowerSpectrumVelRange', 'png', mySize);
save_fig('PowerSpectrumVelRange', 'fig', mySize);

figure (2);
mySize = [10,8];
plot(V_m, f_max);
ax=gca;
set(gca, 'FontName', 'Times New Roman');
set(gca,'FontSize', 12);
xlabel('Test section velocity, [m/s]','fontsize', 12 );
ylabel('Foil vibrational frequency, [Hz]','fontsize', 12 );
ylim([600, 700]);
%save_fig('Natural_frequency', 'png', mySize);
%save_fig('Natural_frequency', 'fig', mySize);
```


A.2: PIV analysis

PIV 11.1 m/s analysis

```

%PIV velocity 11m/s
clc;
clear all;
close all;

%Import firstmeasure
FM = importdata('FM.txt');
f1=FM(:,1);
A1=FM(:,3);
z1=FM(:,2)+1;
[YPeak1, xID1] = max(A1);
idxmax = find(f1==max(f1));

%Import secondmeasure
SM = importdata('SM.txt');
f2=SM(:,1);
A2=SM(:,3);
z2=SM(:,2)+2;
[YPeak2, xID2] = max(A2);
XPeak2 = f2(xID2);

%Import repeatedmeasure
RM = importdata('RM.txt');
f3=RM(:,1);
A3=RM(:,3);
z3=RM(:,2)+3;
[YPeak3, xID3] = max(A3);
XPeak3 = f3(xID3);

%Import offsetMeasure
OM = importdata('PIV1185.txt');
f4=OM(:,1);
A4=OM(:,3);
z4=OM(:,2)+4;
[YPeak4, xID4] = max(A4);
XPeak4 = f4(xID4);

%Normalization, uncomment to activate:
% A1=A1/max(A1);
% A2=A2/max(A2);
% A3=A3/max(A3);

mySize = [13,10];

figure(1)
plot3(z1,f1, A1,'r',z2, f2, A2,'m',z3, f3, A3,'g',z4, f4, A4,'b', 'LineWidth', 1,
'MarkerIndices',[idxmax], 'MarkerSize', 20 );
xlabel('Measurement no., [-]')
ylabel('Frequency, [Hz]', 'fontsize', 12 );
zlabel('Amplitude, [Counts]', 'fontsize', 12);
set(gca,'FontSize', 12);
set(gca, 'FontName', 'Times New Roman');
%grid on;
grid minor;
set(gca, 'Ydir', 'reverse');
xlim([0 5]);
xticks([1 2 3 4]);
xticklabels({'#1', '#2', '#3', '#4'});
ylim([500 700])
hold on;
ax = gca;

```

APPENDICES

```
ax.View = [-45,37];
% save_fig('3DPowerSpectrum11_Shedding', 'png', mySize);
% save_fig('3DPowerSpectrum11_Shedding', 'fig', mySize);

figure(2)
plot(f1, A1,'r', f2, A2,'m', f3, A3,'g',f4, A4,'b', 'LineWidth', 1);
xlabel('Frequency, [Hz]', 'fontsize', 12 );
ylabel('Amplitude, [Counts]', 'fontsize', 12);
set(gca,'FontSize', 12);
set(gca, 'FontName', 'Times New Roman');
legend('First measurement', 'Second measurement', 'Third measurement', 'Offset
measurement');

% save_fig('2DPIVPowerSpectrumLarge', 'png', mySize);
% save_fig('2DPIVPowerSpectrumLarge', 'fig', mySize);

figure(3)
plot(f1, A1,'r', f2, A2,'m', f3, A3,'g',f4, A4,'b', 'LineWidth', 1);
xlabel('Frequency, [Hz]', 'fontsize', 12 );
ylabel('Amplitude, [Counts]', 'fontsize', 12);
set(gca,'FontSize', 12);
set(gca, 'FontName', 'Times New Roman');
axis([640 650 0 600]);
legend('First measurement', 'Second measurement', 'Third measurement', 'Offset
measurement');

% save_fig('2DPIVPowerSpectrumZoom', 'png', mySize);

%Uncertainty in repeatability:
f_max=[f1(xID1), f2(xID2), f3(xID3)];
std_dev_f=std(f_max);
P_f = 4.303*(std_dev_f/sqrt(3)); %Student t-value of 5%=4.303
```

PIV velocity range analysis

```

%PIV velocity range
clc;
clear all;
close all;

mySize = [13,10];
Data={'PIV91.txt',
'PIV96.txt', 'PIV101.txt', 'PIV106.txt', 'PIV111.txt', 'PIV116.txt', 'PIV121.txt', 'PIV126.txt', 'PIV131.txt'};
f_max=zeros(numel(Data),1);
V=[9.1, 9.6, 10.1, 10.6,11.1,11.6,12.1,12.6,13.1];

%3D plot of power spectrum of PIV data
figure(1);
hold on;
grid minor;
ax=gca;
ylabel('Test section velocity, [m/s]')
xlabel('Frequency, [Hz]', 'fontsize', 12 );
zlabel('Amplitude', 'fontsize', 12);
set(gca,'FontSize', 12);
set(gca, 'FontName', 'Times New Roman');
ax.View=[48,35];
set(0,'defaultfigurecolor',[1 1 1]);
xlim([400, 900]);

for i = 1:numel(Data)
    File=load(Data{i});
    f=File(:,1);
    A=File(:,3);
    %Uncomment to normalize:
    A=A/max(A);
    plot3(f,V(i)*ones(size(f)),A);
    [YPeak1, xID] = max(A);
    f_max(i)=f(xID);
    idxmax = find(f==max(f));
end
save_fig('PIVPowerSpectrumRange', 'png', mySize);

%Zoomed plot power spectrum of PIV data
figure (2)
hold on;
ax=gca;
xlabel('Frequency, [Hz]', 'fontsize', 12 );
ylabel('Amplitude', 'fontsize', 12);
set(gca,'FontSize', 12);
set(gca, 'FontName', 'Times New Roman');
set(0,'defaultfigurecolor',[1 1 1]);
ylim([0, 20]);

for i = 1:numel(Data)
    File=load(Data{i});

```

APPENDICES

```
f=File(:,1);
A=File(:,3);
plot(f,A);
end
legend('9.1m/s', '9.6m/s', '10.1m/s', '10.6m/s','11.1m/s','11.6m/s',
'12.1m/s','12.6m/s', '13.1m/s');
save_fig('PIVPowerSpectrumRangeZoom', 'png', mySize);
save_fig('PIVPowerSpectrumRange', 'png', mySize);
```

APPENDIX B: **Measurement Results**

B.1: Strain Measurements

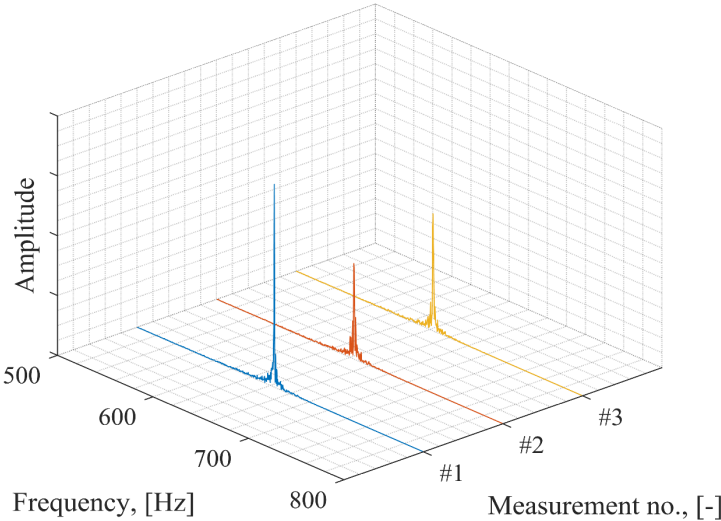


Figure B-1: Three-dimensional power spectrum for the three strain measurements at the spanwise center and 11.1m/s.

B.2: PIV measurements

Lock-in velocity

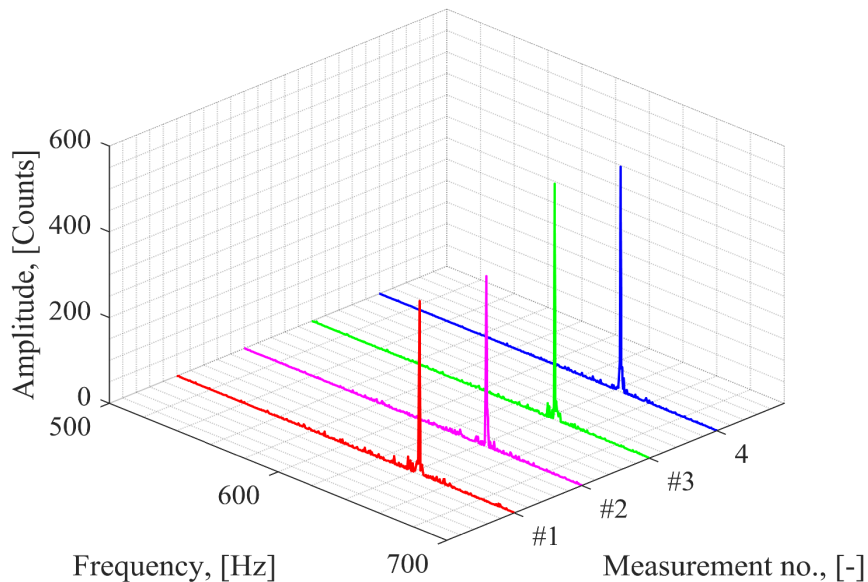


Figure B-2: Three-dimensional power spectrum for the four PIV measurements at 11.1 m/s. The fourth measurements is the 10mm spanwise offset position.

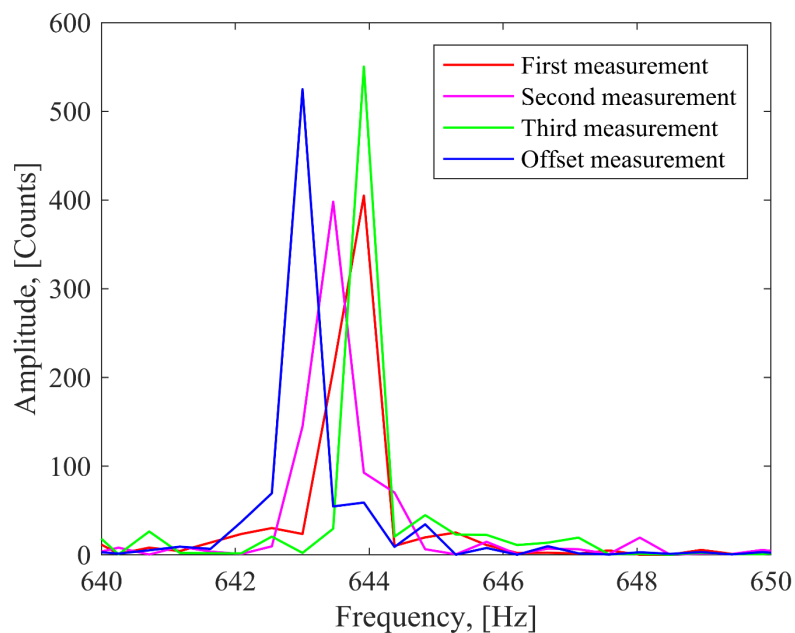


Figure B.3: 2D power spectrum for the four PIV measurements at 11.1 m/s, including the 10 mm spanwise-offset location.

Velocity Range

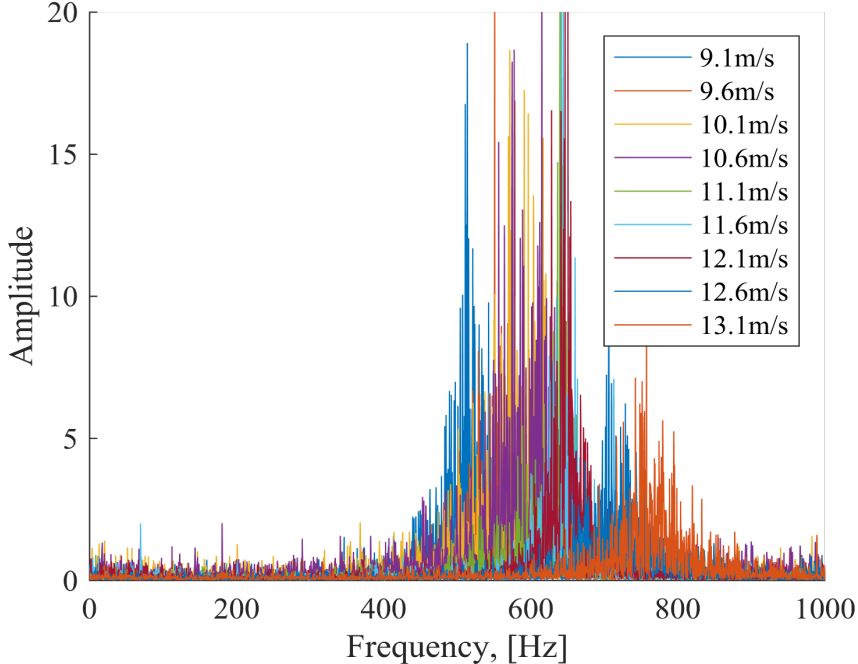


Figure B.4: Two-dimensional zoomed power spectrum for the PIV measurements for the velocity range. Notice the limited amplitude range for a higher resolved comparison.

APPENDIX C: Risk Assessment Report

Risk Assessment Report

HiFrancis Blade Cascade

Project name	PIV measurements on blade cascade for HiFrancis project
Apparatus	Double-Cavity High speed laser, 2*10mJ, 1000Hz, 527nm
Unit	EPT
Equipment manager	Bård Brandåstrø
Project leader	Pål Tore Storli
HSE coordinator	Morten Grønli
HSE responsible (linjeleder)	Therese Løvås
Location	Waterpower Laboratory
Room number	11
Risk assessment performed by	Magne Tveit Bolstad

Approval:

Apparatur kort (UNIT CARD) valid for:	12 months
Forsøk pågår kort (EXPERIMENT IN PROGRESS) valid for:	12 months

Rolle	Navn	Dato	Signatur
Project leader	Pål Tore Storli		
HSE coordinator	Morten Grønli		
HMS responsible (linjeleder)	Therese Løvås		

TABLE OF CONTENTS

1	INTRODUCTION	1
2	CONCLUSION	ERROR! BOOKMARK NOT DEFINED.
3	ORGANISATION	1
4	RISK MANAGEMENT IN THE PROJECT	1
5	DESCRIPTIONS OF EXPERIMENTAL SETUP	2
6	EVACUATION FROM THE EXPERIMENTAL AREA.....	2
7	WARNING	2
7.1	Before experiments.....	2
7.2	Non-conformance	2
8	ASSESSMENT OF TECHNICAL SAFETY	3
8.1	HAZOP	3
8.2	Flammable, reactive and pressurized substances and gas.....	3
8.3	Pressurized equipment.....	4
8.4	Effects on the environment (emissions, noise, temperature, vibration, smell)	4
8.5	Radiation	4
8.6	Chemicals	4
8.7	Electricity safety (deviations from the norms/standards).....	4
9	ASSESSMENT OF OPERATIONAL SAFETY	4
9.1	Procedure HAZOP.....	4
9.2	Operation and emergency shutdown procedure.....	4
9.3	Training of operators.....	5
9.4	Technical modifications.....	5
9.5	Personal protective equipment.....	5
9.5.1	General Safety	5
9.6	Safety equipment	5
9.7	Special predations	5
10	QUANTIFYING OF RISK - RISK MATRIX.....	5
11	REGULATIONS AND GUIDELINES	6
12	DOCUMENTATION.....	6
13	GUIDANCE TO RISK ASSESSMENT TEMPLATE.....	7

1 INTRODUCTION

PIV measurements will be performed on a Site Acceptance Test-rig in accordance with the new PIV equipment at the waterpower laboratory. Measurements will be performed in May-June 2017.

2 ORGANISATION

Role	
Project leader	Pål Tore Storli
Equipment manager	Bård Brandåstrø
Room manager	Bård Brandåstrø
HSE coordinator	Morten Grønli
HSE responsible (linjeleder):	Therese Løvås

3 RISK MANAGEMENT IN THE PROJECT

Hovedaktiviteter risikostyring	Nødvendige tiltak, dokumentasjon	DATE
Prosjekt initiering Project initiation	Prosjekt initiering mal	X
Veiledningsmøte Guidance Meeting	Skjema for Veiledningsmøte med pre-risikovurdering	x
Innledende risikovurdering Initial Assessment	Fareidentifikasjon – HAZID Skjema grovanalyse	x
Vurdering av teknisk sikkerhet Evaluation of technical security	Prosess-HAZOP Tekniske dokumentasjoner	x
Vurdering av operasjonell sikkerhet Evaluation of operational safety	Prosedyre-HAZOP Opplæringsplan for operatører	x
Sluttvurdering, kvalitetssikring Final assessment, quality assurance	Uavhengig kontroll Utstedelse av apparaturkort Utstedelse av forsøk pågår kort	

4 DESCRIPTIONS OF EXPERIMENTAL SETUP

- Drawings and photos describing the setup.
- Process and Instrumentation Diagram (PID) with list of components
- Location of the operator, gas bottles, shutdown valves for water / air.

5 EVACUATION FROM THE EXPERIMENTAL AREA

Evacuate at signal from the alarm system or local gas alarms with its own local alert with sound and light outside the room in question, see 6.2

Evacuation from the rigging area takes place through the marked emergency exits to the assembly point, (corner of Old Chemistry Kjelhuset or parking 1a-b.)

Action on rig before evacuation:

Describe in which condition the rig should be left in case of evacuation (emergency shutdown procedure, water, gas, electric supply, etc.)

6 WARNING

6.1 Before experiments

Send an e-mail with information about the planned experiment to:
iept-experiments@ivt.ntnu.no

The e-mail must include the following information:

- Name of responsible person:
- Experimental setup/rig:
- Start Experiments: (date and time)
- Stop Experiments: (date and time)

You must get the approval back from the laboratory management before start up. All running experiments are notified in the activity calendar for the lab to be sure they are coordinated with other activity.

6.2 Non-conformance

FIRE

If you are NOT able to extinguish the fire, activate the nearest fire alarm and evacuate area. Be then available for fire brigade and building caretaker to detect fire place.

If possible, notify:

NTNU	SINTEF
Morten Grønli, Mob: 918 97 515	Harald Mæhlum, Mob: 930 14 986
Therese Løvås, Mob: 91897007	Anne Karin T. Hemmingsen Mob: 930 19 669
NTNU – SINTEF Beredskapstelefon	800 80 388

GAS ALARM

If a gas alarm occurs, close gas bottles immediately and ventilate the area. If the level of the gas concentration does not decrease within a reasonable time, activate the fire alarm and evacuate the lab. Designated personnel or fire department checks the leak to determine whether it is possible to seal the leak and ventilate the area in a responsible manner.

PERSONAL INJURY

- First aid kit in the fire / first aid stations
- Shout for help
- Start life-saving first aid
- **CALL 113** if there is any doubt whether there is a serious injury

OTHER NON-CONFORMANCE (AVVIK)

NTNU:

You will find the reporting form for non-conformance on:

<https://innsida.ntnu.no/wiki/-/wiki/Norsk/Melde+avvik>

SINTEF:

Synergi

7 ASSESSMENT OF TECHNICAL SAFETY

7.1 HAZOP

See Chapter 13 "Guide to the report template".

The experiment set up is divided into the following nodes:

Node 1	Blade cascade
Node 2	Laser class IV
Node 3	Tent/enclosure

Attachments, Form: Hazop_mal

Conclusion

Node 1:

- Pinch points clearly marked

Node 2:

- Radiation area shielded
- Appropriate signalling and lights in place, light active during operation

Node 3:

- Appropriate signalling and lights in place, light active during operation

7.2 Flammable, reactive and pressurized substances and gas

See Chapter 13 "Guide to the report template".

NO	
----	--

7.3 Pressurized equipment

See Chapter 13 "Guide to the report template".

YES	
-----	--

7.4 Effects on the environment (emissions, noise, temperature, vibration, smell)

See Chapter 13 "Guide to the report template".

NO	
----	--

7.5 Radiation

See Chapter 13 "Guide to the report template".

YES	Radiation Sources need to have an own risk assessment
-----	---

Attachments: Radiation risk assessment

Conclusion:

7.6 Chemicals

See Chapter 13 "Guide to the report template".

NO	
----	--

7.7 Electricity safety (deviations from the norms/standards)

See Chapter 13 "Guide to the report template".

NO	
----	--

8 ASSESSMENT OF OPERATIONAL SAFETY

Ensure that the procedures cover all identified risk factors that must be taken care of. Ensure that the operators and technical performance have sufficient expertise.

8.1 Procedure HAZOP

See Chapter 13 "Guide to the report template".

The method is a procedure to identify causes and sources of danger to operational problems.

Attachments:: HAZOP_MAL_Prosegyre

8.2 Operation procedure and emergency shutdown procedure

See Chapter 13 "Guide to the report template".

The operating procedure is a checklist that must be filled out for each experiment.

Emergency procedure should attempt to set the experiment set up in a harmless state by unforeseen events.

Attachments: Procedure for running experiments

Emergency shutdown procedure:

8.3 Training of operators

8.4 Technical modifications

8.5 Personal protective equipment

- *It is mandatory use of appropriate eye protection in the rig zone*

8.6 General Safety

- *The area around the staging attempts shielded.*
- *Operator has to be present during experiments.*

8.7 Safety equipment

- *Warning signs and warning light, see the Regulations on Safety signs and signalling in the workplace*

8.8 Special predations

9 QUANTIFYING OF RISK - RISK MATRIX

See Chapter 13 "Guide to the report template".

The risk matrix will provide visualization and an overview of activity risks so that management and users get the most complete picture of risk factors.

IDnr	Aktivitet-hendelse	Frekv-Sans	Kons	RV
1	<i>Unintentional refraction/reflection of laser beam</i>	1	A	1A
2	<i>People without protective goggles entering radiation area</i>	1	C	1C
3	<i>Damaging lab equipment</i>	2	B	2B
4	<i>Water-damage on lab equipment</i>	3	B	3C
5	<i>Structural failure due to high pressure</i>	1	C	1C

Conclusion: There is little remaining risk. The most prominent risk is that people unintentionally wander into the radiation area without protective goggles, but proper signalling and blocking should prevent this. The risk is therefore acceptable.

10 REGULATIONS AND GUIDELINES

Se <http://www.arbeidstilsynet.no/regelverk/index.html>

- Lov om tilsyn med elektriske anlegg og elektrisk utstyr (1929)
- Arbeidsmiljøloven
- Forskrift om systematisk helse-, miljø- og sikkerhetsarbeid (HMS Internkontrollforskrift)
- Forskrift om sikkerhet ved arbeid og drift av elektriske anlegg (FSE 2006)
- Forskrift om elektriske forsyningsanlegg (FEF 2006)
- Forskrift om utstyr og sikkerhetssystem til bruk i eksplosjonsfarlig område NEK 420
- Forskrift om håndtering av brannfarlig, reaksjonsfarlig og trykksatt stoff samt utstyr og anlegg som benyttes ved håndteringen
- Forskrift om Håndtering av eksplosjonsfarlig stoff
- Forskrift om bruk av arbeidsutstyr.
- Forskrift om Arbeidsplasser og arbeidslokaler
- Forskrift om Bruk av personlig verneutstyr på arbeidsplassen
- Forskrift om Helse og sikkerhet i eksplosjonsfarlige atmosfærer
- Forskrift om Høytrykksspyling
- Forskrift om Maskiner
- Forskrift om Sikkerhetsskiltning og signalgivning på arbeidsplassen
- Forskrift om Stillaser, stiger og arbeid på tak m.m.
- Forskrift om Sveising, termisk skjæring, termisk sprøyting, kullbuemeisling, lodding og sliping (varmt arbeid)
- Forskrift om Tekniske innretninger
- Forskrift om Tungt og ensformig arbeid
- Forskrift om Vern mot eksponering for kjemikalier på arbeidsplassen (Kjemikalieforskriften)
- Forskrift om Vern mot kunstig optisk stråling på arbeidsplassen
- Forskrift om Vern mot mekaniske vibrasjoner
- Forskrift om Vern mot støy på arbeidsplassen

Veiledninger fra arbeidstilsynet

se: <http://www.arbeidstilsynet.no/regelverk/veiledninger.html>

11 DOCUMENTATION

- Tegninger, foto, beskrivelser av forsøksoppsetningen
- Hazop_mal
- Sertifikat for trykkpåkjent utstyr
- Håndtering avfall i NTNU
- Sikker bruk av LASERE, retningslinje
- HAZOP_MAL_Prosedyre
- Forsøksprosedyre
- Opplæringsplan for operatører
- Skjema for sikker jobb analyse, (SJA)
- Apparatorkortet
- Forsøk pågår kort

12 GUIDANCE TO RISK ASSESSMENT TEMPLATE

Chapter 7 Assessment of technical safety.

Ensure that the design of the experiment set up is optimized in terms of technical safety.

Identifying risk factors related to the selected design, and possibly to initiate re-design to ensure that risk is eliminated as much as possible through technical security.

This should describe what the experimental setup actually are able to manage and acceptance for emission.

7.1 HAZOP

The experimental set up is divided into nodes (eg motor unit, pump unit, cooling unit.). By using guidewords to identify causes, consequences and safeguards, recommendations and conclusions are made according to if necessary safety is obtained. When actions are performed the HAZOP is completed.

(e.g. "No flow", cause: the pipe is deformed, consequence: pump runs hot, precaution: measurement of flow with a link to the emergency or if the consequence is not critical used manual monitoring and are written into the operational procedure.)

7.2 Flammable, reactive and pressurized substances and gas.

According to the Regulations for handling of flammable, reactive and pressurized substances and equipment and facilities used for this:

<p>Flammable material: Solid, liquid or gaseous substance, preparation, and substance with occurrence or combination of these conditions, by its flash point, contact with other substances, pressure, temperature or other chemical properties represent a danger of fire.</p>
--

<p>Reactive substances: Solid, liquid, or gaseous substances, preparations and substances that occur in combinations of these conditions, which on contact with water, by its pressure, temperature or chemical conditions, represents a potentially dangerous reaction, explosion or release of hazardous gas, steam, dust or fog.</p>
--

<p>Pressurized : Other solid, liquid or gaseous substance or mixes having fire or hazardous material response, when under pressure, and thus may represent a risk of uncontrolled emissions</p>
--

Further criteria for the classification of flammable, reactive and pressurized substances are set out in Annex 1 of the Guide to the Regulations "Flammable, reactive and pressurized substances"

<http://www.dsb.no/Global/Publikasjoner/2009/Veiledning/Generell%20veiledning.pdf>

http://www.dsb.no/Global/Publikasjoner/2010/Tema/Temaveiledning_bruk_av_farlig_stoff_Del_1.pdf

Experiment setup area should be reviewed with respect to the assessment of Ex zone

- Zone 0: Always explosive atmosphere, such as inside the tank with gas, flammable liquid.
- Zone 1: Primary zone, sometimes explosive atmosphere such as a complete drain point
- Zone 2: secondary discharge could cause an explosive atmosphere by accident, such as flanges, valves and connection points

7.4 Effects on the environment

With pollution means: bringing solids, liquid or gas to air, water or ground, noise and vibrations, influence of temperature that may cause damage or inconvenience effect to the environment.

Regulations: <http://www.lovddata.no/all/hl-19810313-006.html#6>

NTNU guidance to handling of waste: <http://www.ntnu.no/hms/retningslinjer/HMSR18B.pdf>

7.5 Radiation

Definition of radiation

Ionizing radiation: Electromagnetic radiation (in radiation issues with wavelength <100 nm) or rapid atomic particles (e.g. alpha and beta particles) with the ability to stream ionized atoms or molecules.

Non ionizing radiation: Electromagnetic radiation (wavelength >100 nm), og ultrasound₁ with small or no capability to ionize.

Radiation sources: All ionizing and powerful non-ionizing radiation sources.

Ionizing radiation sources: Sources giving ionizing radiation e.g. all types of radiation sources, x-ray, and electron microscopes.

Powerful non ionizing radiation sources: Sources giving powerful non ionizing radiation which can harm health and/or environment, e.g. class 3B and 4. MR₂ systems, UVC₃ sources, powerful IR sources₄.

₁Ultrasound is an acoustic radiation ("sound") over the audible frequency range (> 20 kHz). In radiation protection regulations are referred to ultrasound with electromagnetic non-ionizing radiation.

₂MR (e.g. NMR) - nuclear magnetic resonance method that is used to "depict" inner structures of different materials.

₃UVC is electromagnetic radiation in the wavelength range 100-280 nm.

₄IR is electromagnetic radiation in the wavelength range 700 nm - 1 mm.

For each laser there should be an information binder (HMSRV3404B) which shall include:

- General information
- Name of the instrument manager, deputy, and local radiation protection coordinator
- Key data on the apparatus
- Instrument-specific documentation
- References to (or copies of) data sheets, radiation protection regulations, etc.
- Assessments of risk factors
- Instructions for users
- Instructions for practical use, startup, operation, shutdown, safety precautions, logging, locking, or use of radiation sensor, etc.
- Emergency procedures
- See NTNU for laser: <http://www.ntnu.no/hms/retningslinjer/HMSR34B.pdf>

7.6 The use and handling of chemicals.

In the meaning chemicals, a element that can pose a danger to employee safety and health

See: <http://www.lovddata.no/cgi-wift/ldles?doc=/sf/sf/sf-20010430-0443.html>

Safety datasheet is to be kept in the HSE binder for the experiment set up and registered in the database for chemicals.

Chapter 8 Assessment of operational procedures.

Ensures that established procedures meet all identified risk factors that must be taken care of through operational barriers and that the operators and technical performance have sufficient expertise.

8.1 Procedure Hazop

Procedural HAZOP is a systematic review of the current procedure, using the fixed HAZOP methodology and defined guidewords. The procedure is broken into individual operations (nodes) and analyzed using guidewords to identify possible nonconformity, confusion or sources of inadequate performance and failure.

8.2 Procedure for running experiments and emergency shutdown.

Have to be prepared for all experiment setups.

The operating procedure has to describe stepwise preparation, startup, during and ending conditions of an experiment. The procedure should describe the assumptions and conditions for starting, operating parameters with the deviation allowed before aborting the experiment and the condition of the rig to be abandoned.

Emergency procedure describes how an emergency shutdown have to be done, (conducted by the uninitiated),

what happens when emergency shutdown, is activated. (electricity / gas supply) and which events will activate the emergency shutdown (fire, leakage).

Chapter 9 Quantifying of RISK

Quantifying of the residue hazards, Risk matrix

To illustrate the overall risk, compared to the risk assessment, each activity is plotted with values for the probability and consequence into the matrix. Use task IDnr.

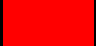


Example: If activity IDnr. 1 has been given a probability 3 and D for consequence the risk value become D3, red. This is done for all activities giving them risk values.

In the matrix are different degrees of risk highlighted in red, yellow or green. When an activity ends up on a red risk (= unacceptable risk), risk reducing action has to be taken

CONSEQUENCES	Catastrophic	E1	E2	E3	E4	E5
	Major	D1	D2	D3	D4	D5
	Moderate	C1	C2	C3	C4	C5
	Minor	B1	B2	B3	B4	B5
	Insignificant	A1	A2	A3	A4	A5
		Rare	Unlikely	Possible	Likely	Almost
		PROBABILITY				

Table 8. Risk's Matrix

Table 9. The principle of the acceptance criterion. Explanation of the colors used in the matrix

COLOUR		DESCRIPTION
Red		Unacceptable risk Action has to be taken to reduce risk
Yellow		Assessment area. Actions has to be considered
Green		Acceptable risk. Action can be taken based on other criteria

Attachment to Risk Assessment report

HiFrancis Blade Cascade PIV LDY300

Project name	PIV measurements on blade cascade for HiFrancis project
Apparatus	Double-Cavity High speed laser, 2*10mJ, 1000Hz, 527nm
Unit	EPT
Equipment manager	Bård Brandåstrø
Project leader	Pål Tore Storli
HSE coordinator	Morten Grønli
HSE responsible (linjeleder)	Therese Løvås
Location	Waterpower Laboratory
Room number	11
Risk assessment performed by	Magne Tveit Bolstad

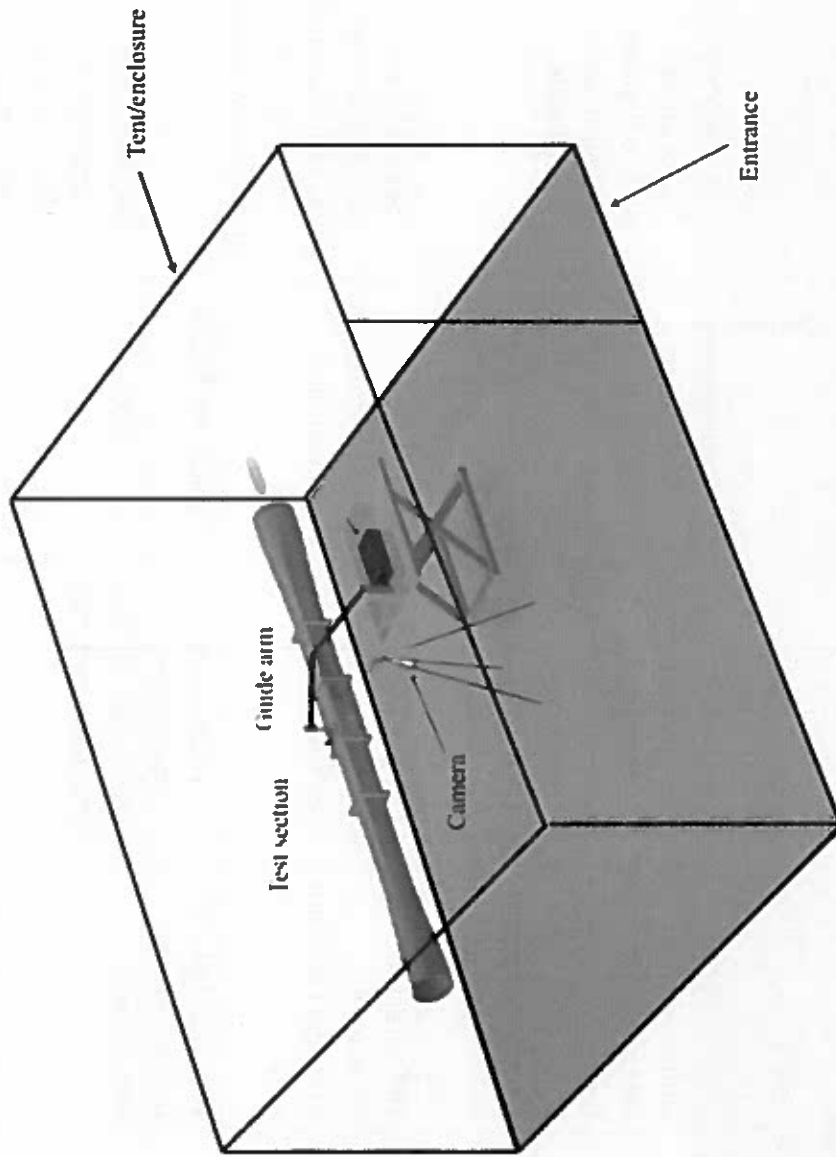
TABLE OF CONTENTS

ATTACHMENT A: PROCESS AND INSTRUMENTATION DIAGRAM.....	1
ATTACHMENT B: HAZOP TEMPLATE	2
ATTACHMENT C: TEST CERTIFICATE FOR LOCAL PRESSURE TESTING	3
ATTACHMENT D: HAZOP PROCEDURE (TEMPLATE).....	4
ATTACHMENT E: PROCEDURE FOR RUNNING EXPERIMENTS	5
ATTACHMENT F: TRAINING OF OPERATORS	7
ATTACHMENT G: FORM FOR SAFE JOB ANALYSIS	8
APPARATURKORT / UNITCARD.....	10
FORSØK PÅGÅR /EXPERIMENT IN PROGRESS	11

ATTACHMENT A: PROCESS AND INSTRUMENTATION DIAGRAM

Radiation area is blocked on all sides by light-blocking fabric (this includes a roof), working as a sealed tent. The entrance is overlapping fabric.

A warning light by the entrance will activate when the laser is on.



ATTACHMENT B: HAZOP TEMPLATE

Project: Node: Laser							Page
Ref	Guideword	Causes	Consequences	Safeguards	Recommendations	Action	Date/Sign
	Unintentional rarefaction of beam	Poor alignment of laser beam, unintentional beam obstruction	Damage to personnel, damage to equipment	Laser emitter latched in place, radiation area enclosed	Careful instrument handling		
	Laser generation unit temperature rise	Cooling system failure	Equipment will overheat and break	-	Be aware of equipment condition		
	Unprotected personnel entering radiation area	Insufficient signalling, radiation area too accessible	Possibility of severe damage to personnel	Signalling and warning light in place, radiation area enclosed with physical obstruction	Always run experiments with warning light on		
	Electrical failures in apparatuses	Wear, poor construction	Equipment failure				
	Fire hazard	Laser beam hitting flammable material	Fire	Enclosing fabric approved for shielding laser experiments.	Make sure a fire extinguisher is easily available		
	Beam interception by operator	Careless equipment handling, obstructed work area	Damage to personnel, severe if lacking protective gear	Goggles approved for laser in use worn by operator	Careful instrument handling		

ATTACHMENT C: TEST CERTIFICATE FOR LOCAL PRESSURE TESTING

Trykkpåkjent utstyr:	Rør
Benyttes i rigg:	
Design trykk for utstyr (bara):	10bar
Maksimum tillatt trykk (bara): (i.e. burst pressure om kjent)	10bar
Maksimum driftstrykk i denne rigg:	10bar

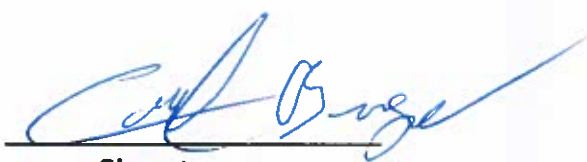
Prøvetrykket skal fastlegges i følge standarden og med hensyn til maksimum tillatt trykk.

Prøvetrykk (bara):	10bar		
X maksimum driftstrykk: I følge standard			
Test medium:	Vann		
Temperatur (°C)			
Start tid:	Fall 2016	Trykk (bara):	
Slutt tid:	Fall 2016	Trykk (bara):	
Maksimum driftstrykk i denne rigg:			

Eventuelle repetisjoner fra atm. trykk til maksimum prøvetrykk:.....

Test trykket, dato for testing og maksimum tillatt driftstrykk skal markers på (skilt eller innslått)

Trondheim 29.08.2017
Sted og dato


Signatur

...

...

...

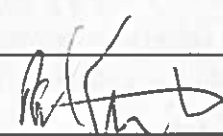
...

...

ATTACHMENT D: HAZOP PROCEDURE (TEMPLATE)

Project: Node: 1		Page					
Ref#	Guideword	Causes	Consequences	Safeguards	Recommendations	Action	Date/Sign
	Not clear procedure	Procedure is to ambitious, or confusingly					
	Step in the wrong place	The procedure can lead to actions done in the wrong pattern or sequence					
	Wrong actions	Procedure improperly specified					
	Incorrect information	Information provided in advance of the specified action is wrong					
	Step missing	Missing step, or step requires too much of operator					
	Step unsuccessful	Step has a high probability of failure					
	Influence and effects from other	Procedure's performance can be affected by other sources					

ATTACHMENT E: PROCEDURE FOR RUNNING EXPERIMENTS

PIV measurements on blade cascade for HiFrancis project	Dato	Signatur
Apparatur Double-Cavity High speed laser, 2*10mJ, 1000Hz, 527nm		
Prosjektleder Pål Tore Storli	20/8-2017	

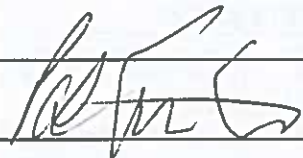
Conditions for the experiment:	Completed
Experiments should be run in normal working hours, 08:00-16:00 during winter time and 08.00-15.00 during summer time. Experiments outside normal working hours shall be approved.	
One person must always be present while running experiments, and should be approved as an experimental leader.	
An early warning is given according to the lab rules, and accepted by authorized personnel.	
Be sure that everyone taking part of the experiment is wearing the necessary protecting equipment and is aware of the shut down procedure and escape routes.	
Preparations	Carried out
1. Make sure the tent is closed.	
2. Post the "Experiment in progress" sign.	
3. Rotate emergency button so that it clicks in the out position.	
4. Turn the system key to "on".	
5. Turn the pump on in either internal or external mode.	
6. Turn on the warning light to open this laser interlock.	
7. Put on laser goggles.	
8. Block the entrance to the experimental area using warning chains.	
9. Turn the laser on in either internal or external mode.	
10. Open the shutter when ready to operate safely.	
During the experiment	
<i>Keep unauthorized personnel out of radiation area</i>	
<i>Avoid wearing jewellery and/or shiny objects</i>	
End of experiment	
<i>Close the shutter.</i>	

	Turn the LASER OFF.	
	Turn the warning light off.	
	Allow the pump to run for approximately 2 minutes to avoid excess heat to damage the equipment.	
	Turn the pump off	
	Turn the system off	
	Press the emergency button	
	To reflect on before the next experiment and experience useful for others	
	Was the experiment completed as planned and on scheduled in professional terms?	
	Was the competence which was needed for security and completion of the experiment available to you?	
	Do you have any information/ knowledge from the experiment that you should document and share with fellow colleagues?	

Operator(s):

Name	Date	Signature
Magne Tveit Bolstad	21.08.17	<i>Magne Tveit Bolstad</i>
Kristian Sagmo	21.08.17	<i>Kristian Sagmo</i>



ATTACHMENT F: TRAINING OF OPERATORS

Project	Date	Signature
PIV measurements on blade cascade for HiFrancis project		
Apparatus Double-Cavity High speed laser, 2*10mJ, 1000Hz, 527nm		
Project Leader Pål Tore Storli	21/8-17	

Knowledge about EPT LAB in general	
Lab	
<ul style="list-style-type: none"> • Access • routines and rules • working hour 	
Knowledge about the evacuation procedures.	
Activity calendar for the Lab	
Early warning, iept-experiments@ivt.ntnu.no	
Knowledge about the experiments	
Procedures for the experiments	
Emergency shutdown.	
Nearest fire and first aid station.	

I hereby declare that I have read and understood the regulatory requirements has received appropriate training to run this experiment and are aware of my personal responsibility by working in EPT laboratories.

Operator(s):

Name	Date	Signature
Magne Tveit Bolstad	21.08.17	
Kristian Sagmo	21.08.17	

ATTACHMENT G: FORM FOR SAFE JOB ANALYSIS

SJA name:	
Date:	Location:
Mark for completed checklist:	

Participators:		
SJA-responsible:		

Specification of work (What and how?):
Risks associated with the work:
Safeguards: (plan for actions, see next page):
Conclusions/comments:

Recommended/approved	Date/Signature:	Recommended/approved	Date/Signature:
SJA-responsible:		HSE responsible:	
Responsible for work:		Other, (position):	

HSE aspect	Yes	No	NA	Comments / actions	Resp.
Documentation, experience, qualifications					
Known operation or work?	X				
Knowledge of experiences / incidents from similar operations?		X			
Necessary personnel?	X				
Communication and coordinating					
Potential conflicts with other operations?		X			
Handling of an eventually incident (alarm, evacuation)?		X			
Need for extra assistance / watch?		X			
Working area					
Unusual working position		X			
Work in tanks, manhole?		X			
Work in ditch, shaft or pit?		X			
Clean and tidy?	X				
Protective equipment beyond the personal?		X			
Weather, wind, visibility, lighting, ventilation?	X				
Usage of scaffolding/lifts/belts/ straps, anti-falling device?		X			
Work at heights?		X			
Ionizing radiation?		X			
Influence of escape routes?		X			
Chemical hazards					
Usage of hazardous/toxic/corrosive chemicals?		X			
Usage of flammable or explosive chemicals?		X			
Risk assessment of usage?	X				
Biological materials/substances?		X			
Dust/asbestos/dust from insulation?		X			
Mechanical hazards					
Stability/strength/tension?		X			
Crush/clamp/cut/hit?		X			
Dust/pressure/temperature?		X			
Handling of waste disposal?		X			
Need of special tools?		X			
Electrical hazards					
Current/Voltage/over 1000V?		X			
Current surge, short circuit?		X			
Loss of current supply?		X			
Area					
Need for inspection?	X				
Marking/system of signs/rope off?	X				
Environmental consequences?		X			
Key physical security systems					
Work on or demounting of safety systems?		X			
Other					

FORSØK PÅGÅR

Enhet (unit) og bygg/romnr. (building/room no.):

NTNU-E 324 11 1. etg

Laboratorium

Dette kortet SKAL henges opp før forsøk kan starte!
This card MUST be posted on the unit before the experiment startup!

Apparatur (Unit) Double-Cavity High speed laser, 2*10mJ, 1000Hz. 527nm	Dato godkjent (Date Approved) onsdag 23. august 2017									
Prosjektleder (Project Leader) Pål Tore Selbo Storli	Telefon mobil/privat (Phone no. mobile/private) 97782146									
Apparaturansvarlig (Unit Responsible) Bård Aslak Brandåstrø	Telefon mobil/privat (Phone no. mobile/private) 91897257									
Godkjente operatører (Approved Operators) <table border="1"><thead><tr><th>Navn/Name</th><th>Telefon/Phone</th><th>Mobil</th></tr></thead><tbody><tr><td>Sagmo, Kristian</td><td></td><td>452 44 270</td></tr><tr><td>Bolstad, Magne Tveit</td><td></td><td></td></tr></tbody></table>	Navn/Name	Telefon/Phone	Mobil	Sagmo, Kristian		452 44 270	Bolstad, Magne Tveit			
Navn/Name	Telefon/Phone	Mobil								
Sagmo, Kristian		452 44 270								
Bolstad, Magne Tveit										
Prosjekt (Project) PIV measurements on blade cascade for HiFrancis project										
Forsøksstid / Experimental time (start - stop) 23.08.2017 - 23.08.2018										
Kort beskrivelse av forsøket og relaterte farer (Short description of the experiment and related hazards) Laser measurements with class IV laser on a blade cascade test section. Danger of eye injury and skin injury. Radiation area clearly marked. The flashing laser light can in some cases trigger epilepsy if proper goggles are not worn.										

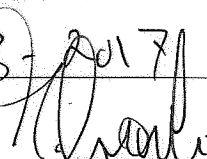
NTNU

Institutt for energi og prosesssteknikk

Dato

23/8/2017

Signert



 NTNU

 SINTEF

